

5

Robert Labuda – Andrej Kovalcik – Jan Repka
– Vladimir Hlavna

**SIMULATION OF A WHEELED VEHICLE
DYNAMIC REGIMES IN LABORATORY
CONDITIONS**

10

Richard Lenhard – Michal Jakubsky – Milan Malcho
– Jozef Jandacka

**ANALYSIS OF TRANSMISSION
PHENOMENA IN LOW-POTENTIAL HEAT
TRANSPORT BY HEAT PIPES IN THE
DEEP- BOREHOLE SIMULATOR**

17

Maria Carnogurska – Miroslav Prihoda
**PHYSICAL MODELING OF FLOW IN
A TUNDISH FOR CONTINUOUS CASTING
MACHINE**

24

Milan Zmindak – Daniel Riecky
**MESHLESS MODELLING OF LAMINATE
MINDLIN PLATES UNDER DYNAMIC
LOADS**

32

Milan Saga – Martin Dudinsky – Peter Pechac
**OPTIMIZATION OF THIN SHELL
STRUCTURES USING FSD ALGORITHMS**

39

Vladimir Dekys – Jozef Broncek
**MEASURING STRAIN
OF THE LATTICE TOWERS**

43

Alzbeta Sapietova – Milan Saga – Pavol Novak
**MULTI-SOFTWARE PLATFORM
FOR SOLVING OF MULTIBODY SYSTEMS
SYNTHESIS**

49

Radoslav Konar – Milos Mician
**NUMERICAL SIMULATION OF RESIDUAL
STRESSES AND DISTORTIONS IN BUTT
WELD IN SIMULATION PROGRAMME
SYSWELD**

55

Slavomir Hreck – Robert Kohar – Stefan Medvecky
**DETERMINATION OF THE MAXIMUM
ROLLER BEARING LOAD WITH REGARDS
TO DURABILITY THEREOF USING
FEM ANALYSIS**

62

Robert Kohar – Slavomir Hreck – Stefan Medvecky
**USAGE OF DYNAMIC ANALYSIS TO
DETERMINE FORCE INTERACTIONS
BETWEEN COMPONENTS OF ROLLING
BEARINGS**

68

Martina Zachariasova – Robert Hudec
– Miroslav Benco – Patrik Kamencay – Peter Lukac
– Slavomir Matuska
**THE EFFECT OF METRIC SPACE ON THE
RESULTS OF GRAPH BASED COLOUR
IMAGE SEGMENTATION**

73

Vladimir Medvid
**APPLICATIONS OF CUTTING STOCK
PROBLEM**

78

Julia Stoberova
**DYNAMICS OF HAEMATOPOIETIC
STEM CELLS MODEL**



Dear readers,

The development of mechanical engineering has been influenced by various factors. In general, they are commercial and legislative factors known as different packages of the European Commission and European Parliament ranging from strict environmental policy up to optimizing interests of mechanical engineering companies. From the beginning, all these influences appear to be distant and general, but later, they are manifested in everyday life of scientists, researchers, designers and producers of mechanical engineering products. They all have to be well prepared to accept the mentioned challenges but they also have to be professionally able to reject illogical and irrational requirements.

An important step to meet the objective is to provide space and time as well as economic background to those who bring new ideas and offer modern solutions. Then, it depends on producers how they will use them in real life.

If mechanical engineering is to remain the moving force of the economic growth also in the future, it is necessary to pay utmost attention to the solutions of the mentioned problems connected mostly with economically and scientifically acceptable use of raw materials. In this issue you can read papers written by authors who are recognized professionals in their fields.

The papers focus mostly on modeling and simulation of not only processes but also activities related to mechanical engineering

Vladimir Hlavna

Robert Labuda – Andrej Kovalcik – Jan Repka – Vladimír Hlavna *

SIMULATION OF A WHEELED VEHICLE DYNAMIC REGIMES IN LABORATORY CONDITIONS

The paper deals with simulation of wheeled vehicle dynamic regimes in laboratory conditions. Based on the analysis of static and dynamic characteristics of the vehicle and test equipment the calculation model was created that calculates the course of a loading moment on the simulator for the given vehicle and driving regime. The basic condition for the simulation is the requirement for reaching congruent courses of driving speeds at the same vehicle control both on the roadway and in the test room.

Key words: Driving simulator, simulation of loading, vehicle, test room, modelling

1. Introduction

When designing new solutions within research activities in the field of transportation technology it is impossible to avoid modelling of real systems either in the test room (physical model) or on the computer (mathematical model [1]). Such a modelling is implemented at creation of control algorithms and programmes for development of computer control systems. It is a significant change in designing the drives when model experimenting is used to a great extent. As early as at designing the vehicle drive there is an assumption that the chosen vehicle operational parameters are controlled from one centre. The cooperation is provided by control systems not only in crisis situations but also in usual operation. The decisive role in the control of drive operation, in cooperation of individual elements as well as the collaboration between the vehicle and driver is performed by automated systems. They are able to identify, process and optimize the parameters of vehicle running in the real time.

The vehicle is a multi-parametric system whose final behaviour depends not only on technical parameters but also on service conditions. Statistics show that human is the weakest link in transportation systems. Although intelligent assistant systems are frequently used in vehicles, human remains the least reliable and hardly predicted link in the transportation systems. The research in crisis situations in real operation is demanding (not only from the point of safety but also technically and economically), therefore, vehicle simulators are used for this purpose. The simulator allows driving a vehicle along a virtual track surrounded by the environment simulating the real conditions. The simulators consist of real parts of vehicle cockpits and surfaces providing the driver's view. Based on the driver's reactions in traffic situations, the simulator creates the conditions which are either similar or identical to the real vehicle behaviour.

A similar principle is applied in the simulators designed for examining changes in processes and energy transmission in the vehicle driving mechanism. The dynamic driving simulator is a new step in the development of virtual testing of drives. It provides researchers, designers and constructors with a deeper insight into the behaviour of a solved drive and offers a direct feedback to their activities from different points of view.

2. Selected problems of drive modelling in a test room

In simulation there is an effort to imitate a real system through a suitable model that is as similar as possible to the real equipment not only with its composition but also with its behaviour. It is suitable to set up the model in a test room from the real components of modelled equipment. Important part of such a model is the device for simulation of loading.

Basic characteristics are taken from steady-state regime measurements. Important requirements put on a loading device include ranges of parameters (moment, output, speed) and way of control. From the point of control, the requirement for the reproducibility of experiment is critical.

In non-steady state regimes it is necessary to take into account other parameters and properties characterizing dynamic properties. It concerns the tested drive and loading device. In mechanical systems it concerns, first of all, the moments of single elements inertia; in hydraulic and pneumatic systems it concerns the capacity resulting from elasticity of the used medium and its piping. An important factor of the model dynamics is its behaviour from the point of delays. It is necessary to consider the delay of processes themselves in the given modelled system and delays in control

* Robert Labuda, Andrej Kovalcik, Jan Repka, Vladimír Hlavna
Faculty of Mechanical Engineering, University of Zilina, Slovakia,
E-mail: robert.labuda@fstroj.uniza.sk

signals transmission. These dependences are gathered experimentally through measurements of transient characteristics.

2.1 Influence of moment of inertia on dynamics of modelled system

If the moment of inertia of the used brake is greater than the moment of inertia of the real system reduced to the drive of the tested drive (for example, of the combustion engine), the testing of dynamics of such a system is limited or completely deleted. A suitable solution in this case can be an inclusion of additional transfer into the tested drive and braking device. On the contrary, if the moment of inertia of the brake is smaller than the reduced moment of tested mechanism, the arrangement should provide the simulation of the additional loading. Doing so there are more options:

- insertion of additional transfer,
- insertion of additional mass (flywheel),
- process adaptation of the moment by means of a static component control.

If the mass of identical moment of inertia with the required moment (identical with the real drive value) is fixed to the shaft of the tested element, the control of loading device will be limited to the control of the static component of the moment only.

2.2 Influence of delays in the controlled system and control mechanism

The vehicle equipped with a combustion engine is a typical example of the system in which delays are demonstrated. The influence of delays is significant mainly because the real operation of such a system is in the majority of applications characterized by an unsteady-state regime. This is caused by an accidentally changing loading, changing interventions of service or automatic control.

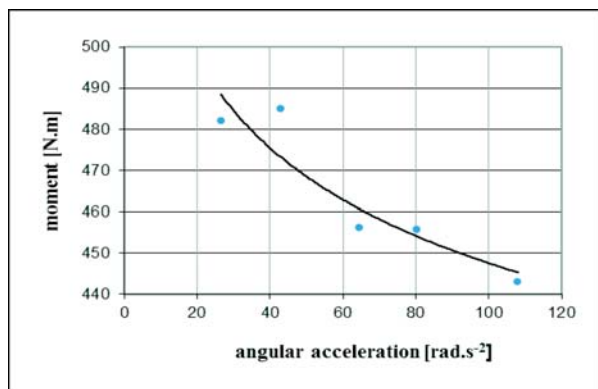


Fig. 1 Dependence of combustion engine moment on change speeds (at starting)

Demonstration of basic characteristics of engines as well as assessment of vehicle characteristics and their traction abilities

(dynamic characteristics [2]) come out of static characteristics. Calculations of a vehicle dynamics are then influenced by certain inaccuracies. These can be found out experimentally, comparing static and dynamic courses. Fig. 1 shows the dependence of the achieved moment of the tested tractor engine Z 8604 on the change speed. The change speed was simulated by a graded static loading at acceleration. The change in regime was induced by a jump change in fuel supply to the maximum value [3]. For calculation of vehicle dynamic characteristics [3] is, therefore, necessary to take into account the change of the combustion engine driving moment with change speed [4].

3. Drive simulator

3.1 Description

The drive simulator is a device that allows vehicle testing in laboratory conditions. The roadway (horizontal or sloping) is replaced by a roller of the test device. The analysis of force relations results from the contact of the vehicle and roadway. For the vehicle on a test track it is the roadway with given parameters, in a test room it is a roadway replaced by rollers of the test room.

Steady-state regime in a roller test room.

The objective is to express the volume of the brake moment on the test rollers that is needed for the equilibrium of forces (F_h) between the vehicle wheels and test rollers. The driving force comes out of the equilibrium of moments on the driving wheel, Fig. 2a

$$F_h \cdot r_d - M_h + M_f = 0 \tag{1}$$

where

$$F_h = \frac{M_h - M_f}{r_d} \tag{2}$$

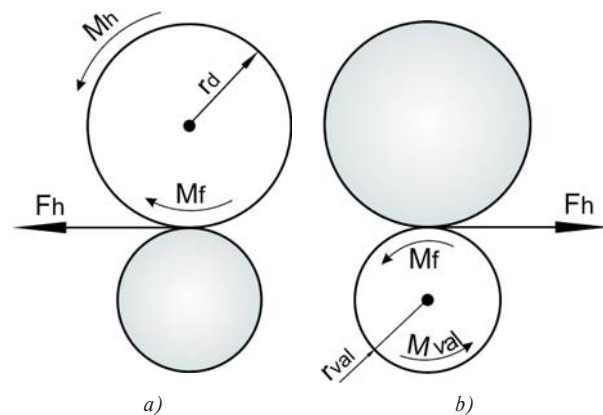


Fig. 2 Scheme of force relations in the contact of vehicle and test rollers in a steady state

From the equilibrium of moments on the driven roller, Fig. 2b

$$M_{val} + M_f = F_h \cdot r_{val} \quad (3)$$

We can determine

$$M_{val} = F_h \cdot r_{val} - M_f \quad (4)$$

where

- F_h - driving force on the vehicle wheels,
- M_h - driving moment on the vehicle wheels,
- M_f - moment of rolling resistance between vehicle wheels and rollers,
- r_d - dynamic radius of the driving wheel,
- M_{val} - moment on test rollers,
- r_{val} - test rollers radius.

From equations (2) and (4) the relation between moments on the driving wheel and braked rollers can be expressed

$$M_{val} = M_h \cdot \frac{r_{val}}{r_d} - M_f \cdot \left(1 + \frac{r_{val}}{r_d}\right) \quad (5)$$

To achieve the values M_{val} on the rollers, the electrical dynamometer generating a particular brake moment is used.

Dynamic - unsteady-state regime of the vehicle

In an unsteady-state regime there are, apart from static load, resistances from inertia effects of moving and rotating masses of the tested vehicle, and inertia effects of the loading device. In loading simulation it is necessary to consider the fact that the tested vehicle stands still while the "roadway" - replaced by test rollers - is moving.

The volume of driving force on the vehicle wheels results from the motion equation [5]

$$F_h = F_v + F_f + F_s + m_v \cdot \delta \cdot \frac{dv_v}{dt} \quad (6)$$

For the equilibrium of moments on test rollers the following holds:

$$F_h \cdot r_{val} = M_{val} + M_f + I_{val} \cdot \frac{d\omega_{val}}{dt} \quad (7)$$

and the following driving force results:

$$F_h = \frac{M_{val} + M_f}{r_{val}} + \frac{I_{val}}{r_{val}^2} \cdot \frac{dv_{val}}{dt} \quad (8)$$

$$M_b^d = F_{odp} \cdot r_d \cdot i_{k,d} \cdot \eta_{k,d} + \frac{1}{r_d \cdot i_{k,d}} \cdot \left(m_v \cdot r_d^2 \cdot i_{k,d}^2 \cdot \eta_{k,d} + 4 \cdot I_k \cdot i_{k,d}^2 \cdot \eta_{k,d} + I_{sm} \cdot i_{sm,d}^2 \cdot \eta_{sm,d} - 4 \cdot I_{val} \cdot i_{v,d}^2 \cdot \frac{1}{\eta_{v,d}} - I_d \right) \cdot \frac{dv_v}{dt} \quad (10)$$

where

- F_v - vehicle air resistance,
- F_f - rolling resistance between driving wheels and road,
- F_s - climbing resistance,
- m_v - vehicle total mass,
- δ - influence coefficient of rotating masses,
- v_v - circumferential speed on driving wheel (vehicle speed),

- I_{val} - moments of inertia of rotating rollers and parts among rollers and brake dynamometer reduced to the test rollers shaft,
- ω_{val} - roller angular velocity.

From the equality of the right sides of equations (6) and (8) the relation between the drive moment on rollers and resistances of the vehicle at slide less running ($v_v = v_{val}$) can be expressed.

The simulation of vehicle loading is carried out through the control of the brake moment of rollers M_{val} in compliance with the required acceleration of the vehicle dv_v/dt .

$$\frac{M_{val}}{r_{val}} = F_v + F_f + F_s - \frac{M_f}{r_{val}} + \left(m_v \cdot \delta - \frac{I_{val}}{r_{val}^2} \right) \cdot \frac{dv_v}{dt} \quad (9)$$

Equation (9) is the basis of the programme control of the moment on rollers according to the required acceleration. Modern drive simulators use the measurements of roller acceleration for control.

4. Simulation of vehicle starting

For loading simulation we chose the course of acceleration at the starting of Golf 1.4 TSI along the standardized test track with exactly defined parameters and respecting the conditions of official testing [6].

4.1 Simulation of vehicle loading on the dynamometer shaft of a roller test room

The loading simulation was performed on the dynamometer, point *D* in Fig. 3. The simulation is influenced also by the increase in rolling resistance during the wheel rolling on test rollers opposed to rolling on the roadway - M_f/r_{val} . In an unsteady-state regime the control of brake moment will simulate the dynamic component representing inertia effects of moving masses of the vehicle and rotational masses of the drive. The control takes into account also inertia effects of rotating masses of loading device mechanisms (rollers, gear box, dynamometer rotor,...). The brake moment on the dynamometer shaft will be controlled in compliance with the relation:

where

- $i_{vd} = n_{val}/n_d$ transmission ratio between the dynamometer and test rollers,
- $i_{kd} = n_k/n_d$ transmission ratio between the vehicle wheels and dynamometer shaft,
- $i_{smd} = n_{sm}/n_d$ transmission ratio between the combustion engine and dynamometer,

- η_{kd} mechanical efficiency between the vehicle wheels and test room dynamometer,
- η_{vd} mechanical efficiency between the rollers and test room dynamometer,
- η_{smd} mechanical efficiency between the combustion engine and dynamometer,
- F_{odp} drive resistance ($F_v + F_f + F_s$),
- I_k, I_{sm} moment of wheel inertia and combustion engine.

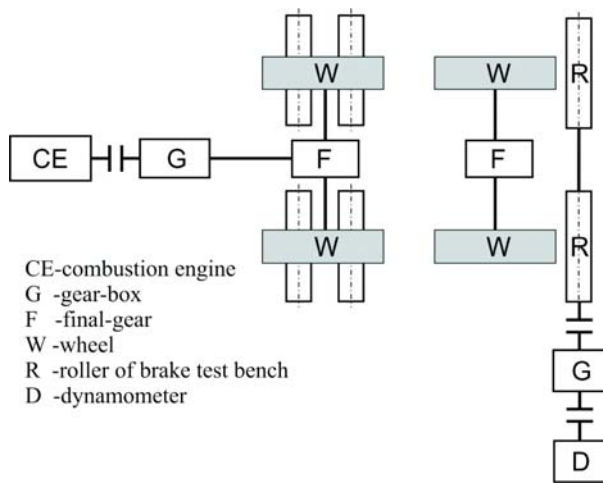


Fig. 3 Scheme of vehicle mechanism and output roller test room

4.2 Simulation of vehicle loading on combustion engine shaft

The system scheme in Fig. 4 shows a connection of the simulator directly to the combustion engine shaft. The simulator role is to induce the same loading on the combustion engine shaft as the loading from the transmission device and run on the real vehicle for the specified regime. Similarly as in equation (10) the relation for simulation of the moment on the combustion engine shaft is created:

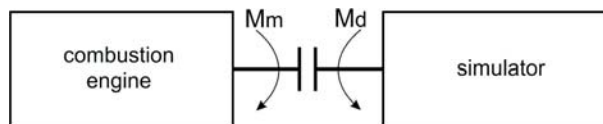


Fig. 4 Scheme simulator connection to combustion engine shaft

$$M_b^{sm} = F_{odp} \cdot \frac{r_d}{i_{sm,k} \cdot \eta_{sm,k}} + \frac{i_{sm,k}}{r_d} \cdot \left(m_v \cdot r_d^2 \cdot \frac{1}{i_{sm,k}^2 \cdot \eta_{sm,k}} + 4 \cdot I_k \cdot \frac{1}{i_{sm,k}^2 \cdot \eta_{sm,k}} + I_{sm} \right) \cdot \frac{dv}{dt} \tag{11}$$

where

- $i_{smk} = n_{sm}/n_k$ transmission ratio between the combustion engine and vehicle wheels,
- η_{smk} mechanical efficiency between combustion engine and vehicle driving wheels.

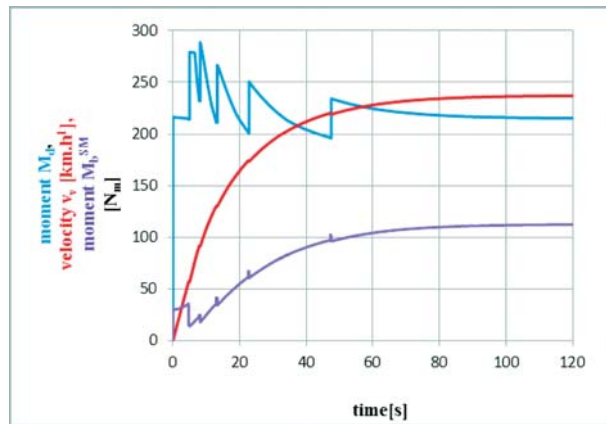


Fig. 5 Time characteristic of velocity for a vehicle run-up on dry asphalt; brake moments simulated on dynamometer shaft and on combustion engine shaft

5. Results of simulation

The basis for the simulation of loading is the time velocity characteristic achieved through the calculation in the program DYNAST [7]. To detune the programme of the brake moment simulation in the test room, the dynamic characteristic of a chosen vehicle starting was performed in the programme Dynast [7]. Fig. 5 illustrates the vehicle starting characterized by a time velocity characteristic (red line) and depiction of the courses of brake moments on the dynamometer shaft of the roller test room (blue line) and on the combustion engine shaft (violet line). Fig. 6 shows the relationship between the moment generated by the combustion engine and loading moment on the same shaft for the same time velocity characteristic (Fig. 5). The simulation of the brake moment on the combustion engine shaft for various roadway surfaces is illustrated in Fig. 7. In all the courses ($M = \text{konst.}$) the limitations are given by adhesion conditions. The curves M_d follow the declining section of the outer speed characteristic of the combustion engine behind the point M_{max} , (gear change at the revolutions of 4000 min^{-1}).

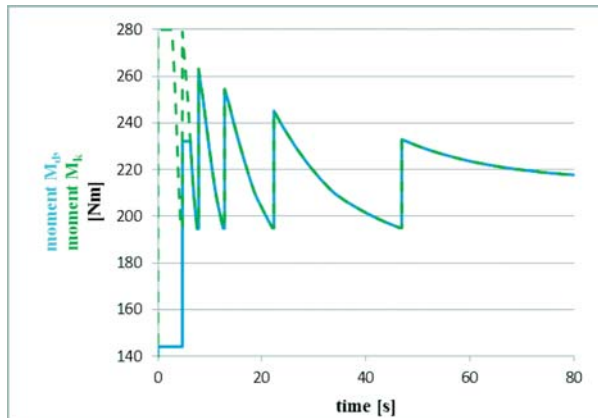


Fig. 6 Process of simulated brake moment on combustion engine shaft and moment generated by a combustion engine

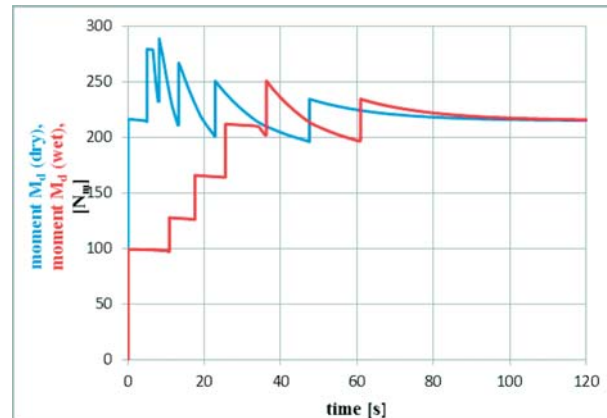


Fig. 7 Comparison of simulated brake moment on the engine shaft for dry and wet asphalt

6. Conclusion

The paper presents the calculation and simulation of loading in the test room by which the real vehicle loading on the test bed is replaced. Another step of the solution will be the model of the whole vehicle system, of loading equipment and simulation of the vehicle dynamics at the programmed change in loading or in the engine driving moment.

Acknowledgements

This contribution was created within the framework of the project KEGA 038ZU-4/2011 and VEGA 1/0554/10, which are supported by the Ministry of Education of the Slovak Republic.

References

- [1] LAJCAKOVA, G., MELCER, J.: Dynamic Effect of Moving Vehicles on the Road Concrete Slabs, In: *Communications - Scientific Letters of the University of Zilina*, No. 3, 2011, ISSN 1335-4205.
- [2] HLAVNA, V., GERLICI, J., LABUDA, R., LANG, A.: *Means of Transport - Theory*, EDIS - Publishing house of University of Zilina, 2006, ISBN 80-8070-498-8.
- [3] LABUDA, R., ISTENÍK, R.: *Results of Comparison Measurements Made on a Turbocharged Combustion Engine*. In: Proc. of Transfer 2004, Section 6, Trenčín, 2004, ISBN 80-8075-030-0
- [4] SVOBODA, J.: *The Theory of Means of Transport*, Publishing house, CVUT in Prague, 2000,
- [5] SEMETKO, J. et al.: *Mobile Energy Means*, Publishing Priroda, 1986
- [6] VLK, F.: *Testing and Diagnostics of Motor Vehicles - 1st edition*, Brno, 2001, p. 576, ISBN 80-238-6573-0.
- [7] ISTENIK, R., FITZ, P.: *Program System of Dynast*, EDIS - Publishing house, University of Zilina, 2001.

Richard Lenhard – Michal Jakubsky – Milan Malcho – Jozef Jandacka *

ANALYSIS OF TRANSMISSION PHENOMENA IN LOW-POTENTIAL HEAT TRANSPORT BY HEAT PIPES IN THE DEEP- BOREHOLE SIMULATOR

This article presents a proposal of a simulator for low-potential geothermal heat transfer by means of heat pipes into the heat pump exchanger section. On this device the research on transmission phenomena at different temperatures at the simulator inlet was done. Measurements were taken at various temperature and pressure parameters of carbon dioxide as a working substance in the heat pipe. The paper contains experimental measurements on the simulator for low potential heat transfer and their analysis, theoretical analysis of phase changes in carbon dioxide in the heat pipes depending on changes in pressure and temperature. Simultaneously, the impact of these two quantities on other parameters of the system will be analyzed, namely, input and output temperatures of the coolant in the heat exchanger and cooling of the surrounding rocks. In the conclusion are laboratory results and the CFD simulation model of low-potential geothermal borehole.

Key words: heat pipes, low-potential heat, deep-borehole simulator, geothermal heat

1. Introduction

At present, considerable attention is paid to the use of low-potential geo heat by means of heat pumps obtaining the low-potential heat by forced circulation pumps. One possibility to increase the intensity of low-potential heat transfer is the application of heat pipes (HP) placed in deep boreholes.

2. Simulator of deep borehole

The device for the use of low-potential geothermal heat without forced circulation of the heat medium in a deep well pressure is equipment using domestic energy resources. Such use has a direct impact on the environmental protection through the reduction in CO₂ production in providing thermal comfort.

The project innovativeness lies in the use of low potential geo heat for heating without any circulating pump to provide warm fluid flow in a deep borehole or its model.

The purpose of the designed device is to simulate transfer of low-potential heat from rocks by means of a collector with cooling fluid and heat pipes in laboratory conditions. It is also possible to perform measurements of heat flows at identical input temperature conditions and at different heat pipes filling (CO₂, NH₃) at various pressures during filling the pipes.



Fig. 1 Simulator

The device (simulator Fig. 1) for the transport of low-potential heat through stage conversions in the evaporation and condensation sections of the pipes at temperatures below 0 °C enables the development of research activities for the verification of manufacturing technology of heat pipes suitable for the use of low-potential geo heat in laboratory conditions. Individual components of the device allow the investigation on thermo kinetic parameters of heat transport from rocks to the heat carrier on the model. The

* Richard Lenhard, Michal Jakubsky, Milan Malcho, Jozef Jandacka

University of Zilina, Faculty of Mechanical Engineering, Department of Power Engineering, Zilina, Slovakia, E-mail: richard.lenhard@fstroj.uniza.sk

device enables a realistic modeling of heat flows from rocks to the heat carrying medium.

This device, which was designed as a scale model of two deep wells, each of which carries away geo heat by means of other technology and other heat carrier. The basic idea lies in the simulation of geoprocesses, i.e. in accumulation of heat in rocks through heating and subsequent carrying the heat away with the use of both existing and new technologies.

3. Construction of the borehole model

The borehole model consists of several simple components. The borehole itself is a 200 mm polyethylene tube which is 5 m high, Fig. 2. The polyethylene tube of diameter 500 mm and 5 m high represents the neighborhood of the cylinder-shaped borehole. A smaller tube is coaxially secured in a larger one by means of insert connectors. Four heat pipes with carbon dioxide as a working fluid supplied from a gas bottle are inserted into a borehole (200 mm polyethylene tube). The heat pipe surrounding is filled with bentonite in which heat is accumulated and subsequently taken away through the heat pipes. The inner annular space is filled with damp sand, (rock neighborhood of the borehole) whose coefficient of thermal conductivity is $1.63 \text{ W}\cdot\text{m}^{-1}\cdot\text{K}^{-1}$.

The outside pipe circumference (500 mm) is spirally wound by a heating cable whose output is $10 \text{ W}\cdot\text{m}^{-1}$ (it substitutes accumulation of Earth's heat). The cable diameter is 6 mm and the pitch is 30 mm (Fig. 2) [1].

NiCr-Ni thermocouples were used to observe the course of temperatures in the borehole average and height, Fig. 3. Thermocouples are touch temperature sensors consisting of two different metals welded together. There is surface tension on the weld joint whose quantity depends on the temperature.

For the simulator we will use 26 thermocouples which will be connected to the Ahlborn Almemo measuring instruments. The control panel is connected to a laptop with the software AMR

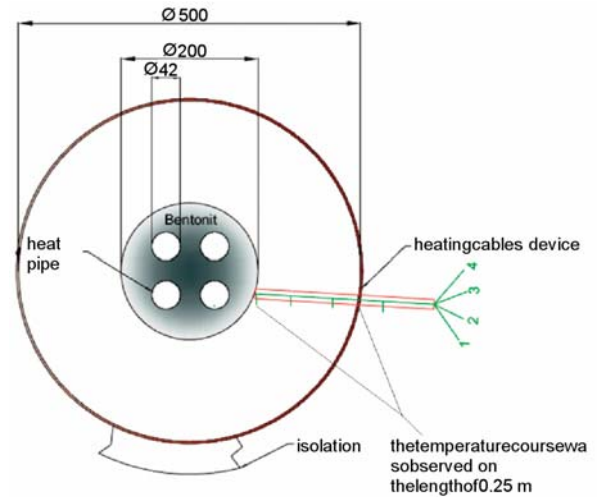


Fig. 3 A cross section of a model borehole and the way in which thermocouples are introduced

Wincontrol 6, that records all the data in Excel within pre-set time intervals. The measuring station was located on the platform 4 m above the ground. The length of individual thermocouples differs with regard to their position in the simulator. The bunch of 26 thermocouples is kept in a protection sleeve for their better arrangement towards the control panel.

It is important to know the phase transformation of carbon dioxide in the bottle as the filling of heat pipes is provided from a pressure bottle. The bottle was weighed after each filling of the heat pipes and we could follow changes in its mass. We are thus informed on the total amount of CO_2 (kg) in the heat tubes.

The simulator is designed so that the evaporation part of the heat pipe is introduced in the heat exchanger and the coolant (Thermal G) in the exchanger carries away the heat from the working medium (CO_2) in the heat pipe, Fig. 4. The coolant in the exchanger washes the heat tubes surfaces in which condensation of gaseous CO_2 occurs. Subsequently, the condensate flows down

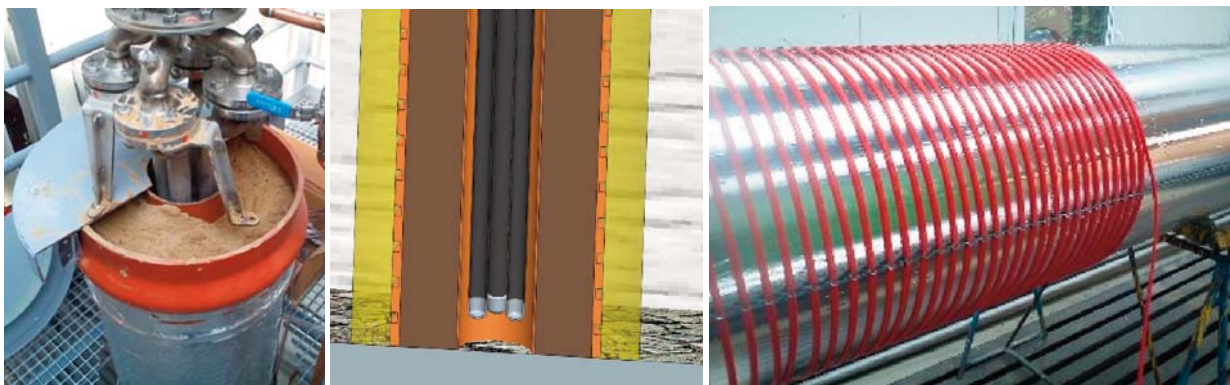


Fig. 2 Heat-pipe embedded in borehole models and electric heating cables as natural surroundings of the borehole substituting the Earth's heat

the heat pipes walls to the bottom part where CO₂ is in a liquid form and the whole process is repeated. The process without forced circulation can work only at a certain pressure and temperature which corresponds to the saturation curve [2].

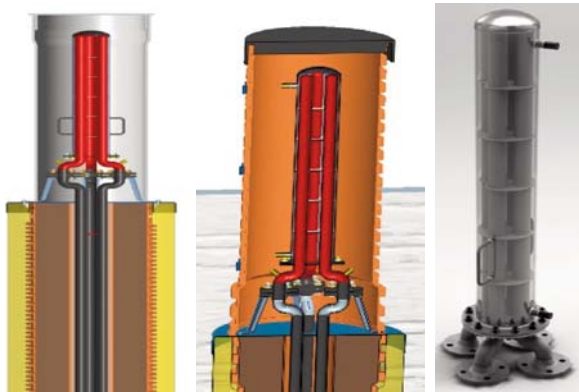


Fig. 4 Upper part of heat pipes placed in heat exchanger

CO₂ is in a gaseous form at the initial pressure of 2.37 MPa and at the temperature of 37 °C. In Fig. 5 the red point shows the concrete state of gas in a phase diagram. In this situation no change of state occurs. The process described above can occur only when we move along the saturation curve. It is, therefore, necessary to increase the pressure or to lower the temperature. After the CO₂ gets into a state of saturation, it will be necessary to maintain this state by means of heating cables = the Earth's heat. The achieved equilibrium between the Earth's heat supply and its take away enables a long-term heat take away in the heat exchanger.

The simulator condition before the measurements was as follows:

- pressure of CO₂ in the heat tubes: $p_0 = 2.37$ MPa
- the average temperature in the simulator (average value of 24 thermocouples placed along the simulator height and diameter - borehole cylinder): $t_0 = 37$ °C,

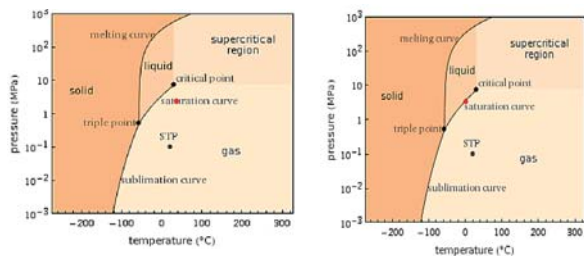


Fig. 5 Phase diagram showing CO₂ specific conditions [3]

The average temperature in the simulator before starting the measurement did not correspond to the actual soil temperatures at the depth of 150 m, because the temperature increases with depth according to the geothermal gradient by 3 or 4 °C for 100 vertical

meters [4]. From 30 m and lower the temperature continuously increases by 1 °C for every 32.7 m. At the depth of 3 km it is about 100 °C. Preset average temperature in the simulator $t_0 = 37$ °C corresponded to the depth of approximately 1000 m. For the purpose of measurements and simulation of the most frequently constructed wells at the depth of 150 m, we needed during the measurement to achieve the temperature from 9 up to 12 °C.

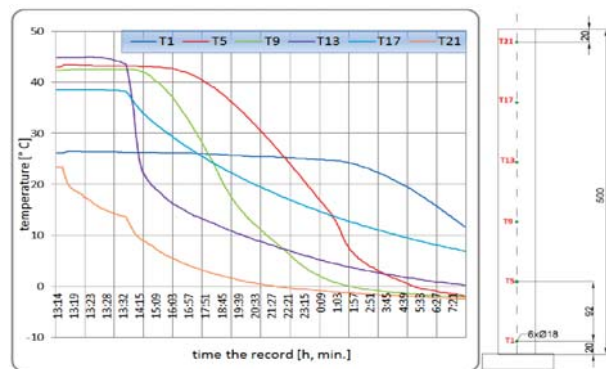


Fig. 6 Recorded drops in temperatures

We will increase the initial pressure $p_0 = 2.37$ MPa to $p_1 = 3.5$ MPa. After the increase in pressure, the temperature drop in the simulator was monitored. When the average temperature dropped to $t_1 = 9.11$ °C (19 hrs. of record), we turned on the heating by means of electric heating cables alongside the simulator-borehole height. At this temperature the pressure was 3.04 MPa. To be able to exactly determine the CO₂ temperature we have to consider only those thermocouples that are located in the vicinity of the heat pipe (Fig. 6). The total average temperature gives us an idea of the soil temperature, but for the average temperature of the working medium only the thermocouples placed very close the heat tube should be taken into account.

We obtain 1 kW of heat output from approximately 12 to 18 m of a borehole [5]. If we choose the value of 17 m for the output of 1000 W we get from 1 m borehole approximately 60 W. The heating by means of heating cables alongside the simulator is divided into 3 sections, each of which is connected to the power supply RAT whose performance is set to the value of 60 W. Such an output suffices to maintain the average temperature in the simulator. Fig. 6 shows the section in which temperatures begin to drop and the state of “quasi-equilibrium” begins. The temperatures level off.

The actual borehole is an infinite cylinder in which the heat spreads in the direction of the temperature drop, i.e., to the point where the heat is carried away by means of chosen technology. Since in laboratory conditions an infinite rock cylinder cannot be measured, heat must be supplied to the borehole in some other way. This is provided by means of electric heating cables that heat the sand (rock) in the borehole neighborhood.

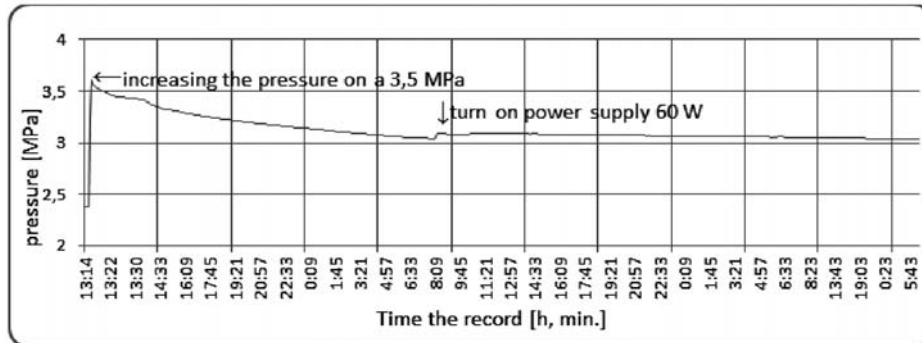


Fig. 7 Pressure increase in the tubes and its several-hour drop corresponding to temperature drop in the simulator

Fig. 7 illustrates the pressure course of CO₂ in the simulator from the pressure p_0 to p_1 . Pressure drop lasting several hours resulted in the whole simulator cooling. When the temperature in the simulator increases after switching on the electric heating cable, there was a slight increase in pressure.

Due to the pressure increase (to 3.5 MPa) we achieved the average temperature drop (by 27.9 °C) in the simulator (the temperature corresponding to the depth of 150 m). Using heating cables we ensured the stabilization of temperature and pressure in the simulator (delivery of 60 W during 24 hours.) We thus achieved the average temperature difference $\Delta t = 0.56$ °C in the heat exchanger. The specific heat capacity of the coolant Thermal G is $3300 \text{ J.kg}^{-1}.\text{K}^{-1}$ and the average flow rate recorded during the measurement was $11 \text{ kg.min}^{-1} = 0.18 \text{ kg.s}^{-1}$. We calculated that the heat carried away during the state of equilibrium was $\dot{Q} = 332 \text{ W}$.

4. Numerical Simulation of Borehole Model for the Transport of Geothermal Heat

Numerical models (Fig. 8) were developed on the basis of a real model of the simulator designed to simulate geothermal heat with forced circulation.



Fig. 8 External and internal structure of borehole simulator

The geometry of simulator model was created in the Gambit program according to the already designed construction. Having

meshed the model, the boundary conditions were set (fluid geometry, solid material geometry, velocity and pressure conditions at the inlet and outlet). The model created this way was transferred to Fluent program [6].

Fluent program is commonly used CFD software, which defines boundary conditions (Fig. 9) that are understood as a precondition for the correct calculation. The Turbulent model was as two - equations $k - \epsilon$. This is the most widely tested and used a two-equation -transport- model (two transport equations for k and ϵ) [7].

The transport equations for k and ϵ can be deduced from the modeled equations by introducing a gradient diffusion hypothesis (with isotropic viscosity) in the turbulent diffusion terms for k and ϵ , and replacing R_{ij} in the production terms by its behavior law (1):

$$R_{ij} = \frac{2}{3}k\delta_{ij} - \nu_t(\overline{U}_{ij} + \overline{U}_{ji}), \quad (1)$$

$$\frac{dk}{dt} = P + \left(\frac{\nu_t}{h_k}k\right)_{,i} - \epsilon, \quad (2)$$

$$\frac{d\epsilon}{dt} = C_{\epsilon 1} \frac{P\epsilon}{k} + \left(\frac{\nu_t}{h_\epsilon}\epsilon\right)_{,i} - C_{\epsilon 2} \frac{\epsilon^2}{k}, \quad (3)$$

With and $P = \nu_t \overline{U}_{i,j}(\overline{U}_{i,j} + \overline{U}_{j,i})$, $\nu_t = c\mu(k^2/\epsilon)$, h_k and h_ϵ standing for turbulent Prandtl - Schmidt numbers assumed to be constant. The components of the Reynolds stress tensor are obtained from the behavior law $R_{ij} = 2/3k\delta_{ij} - \nu_t(\overline{U}_{i,j} + \overline{U}_{j,i})$. If this law gives a good approximation of the shear stresses, the normal stresses are, however, poorly estimated in general.

Determination of numerical constants

The decay of grid turbulence allows us to determine the value of constant $C_{\epsilon 2}$; its value is found to be $C_{\epsilon 2} = 1.9$.

Wall turbulence (logarithmic region of the turbulent boundary layer on a flat plate) yields the relation:

$$C_{\epsilon 1} = C_{\epsilon 2} - \frac{K^2}{h_\epsilon \sqrt{c_\mu}} \quad (K = 0.41 \text{ Karman constant}) \quad (4)$$

and also $c\mu = u_*^4/k^2$ with $u_* = \sqrt{\tau_w/\rho}$ (wall friction velocity).

Referring to experimental data, it can be deduced $c\mu \approx 0.09$

The numerical values of constants recommended by Launder B.E., (LAU 75A) are the following:

$$c\mu = 0.09, h_k = 1.0, h_e = 1.3, C_{\epsilon 1} = 1.44, C_{\epsilon 2} = 1.92 \quad (5)$$

The $k-\epsilon$ model generally gives good results in simple flows as far as the means of the velocities and energies are concerned. But it cannot predict sufficiently the specific characteristics of complex flows (a recirculation of the regions, the secondary flows, etc...) [8].

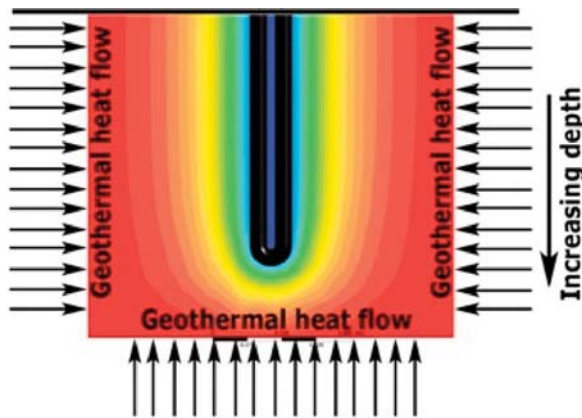


Fig. 9 Boundary conditions

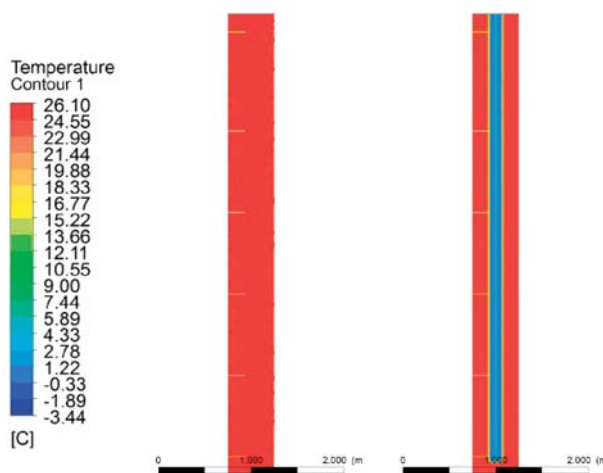


Fig. 10 Simulation begins at 0 s

Fig. 11 Simulation after 10 min

Boundary conditions for simulation of heat transfer in geothermal borehole simulator were as follows:

- time for cooling soils,
- stabilization time for continual delivery of low potential heat energy.
- temperature of soil and ambient,
- physical properties of soil and pipe[9],
- wall temperature of the pipe and setting the conductivity to extract low potential heat from soil [10] [11].

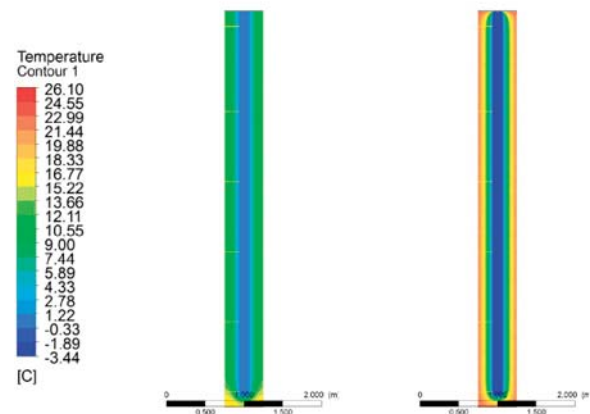


Fig. 12 Simulation after 19 hours, stabilized

Fig. 13 Simulation after 48 hours

Results from the numerical simulation on one of the borehole models are shown in Figs. 10–14, where we can see when the simulation begins at the temperature 26.1 °C. Fig. 12 shows the result after accumulation that lasted 19 hours (borehole model was cooled to an average temperature of 11.4 °C by U-ground heat exchanger with a temperature –0.6 °C). Then the calculation was changed (turn on the heating shell borehole model at 22 °C and cooling by U-ground heat exchanger with a temperature –3.4 °C). This way a continual delivery of heat for the transfer of low potential heat energy from soil was provided. Fig. 13 presents the final result where the borehole model is stabilized. Figs. 10–14 show a yellow line marking the place where measurements taken on the borehole model were recorded.

The simulation results from each time step shown in Figs. 15 – 17 were gathered from the same point (location of the temperature sensors is shown in Fig. 3; measuring points are shown in Fig. 6; placement of temperature sensors in the simulations are yellow lines; the results are from the measuring positions T1 and T21) as taken on the borehole model. The results after 10 min of stimulation can be seen in Fig. 15. The temperatures taken in the first T1 and last T21 points have identical values. It means that the whole model has equally stabilizing temperature along the cross section.

Fig. 16 shows the simulation results after 19 hours where the cooling of the borehole can be seen. Temperatures measured in the first and last measurement points indicate that the average temperature reached in the borehole model was the same as the measured temperature.

Fig. 17 shows the simulation results after 48 hours where the temperatures in the first and last measuring point are uniform along the cross-section. It means that the same average temperatures were achieved as those taken on the simulator and the model was again stabilized. This will ensure a uniform heat delivery.

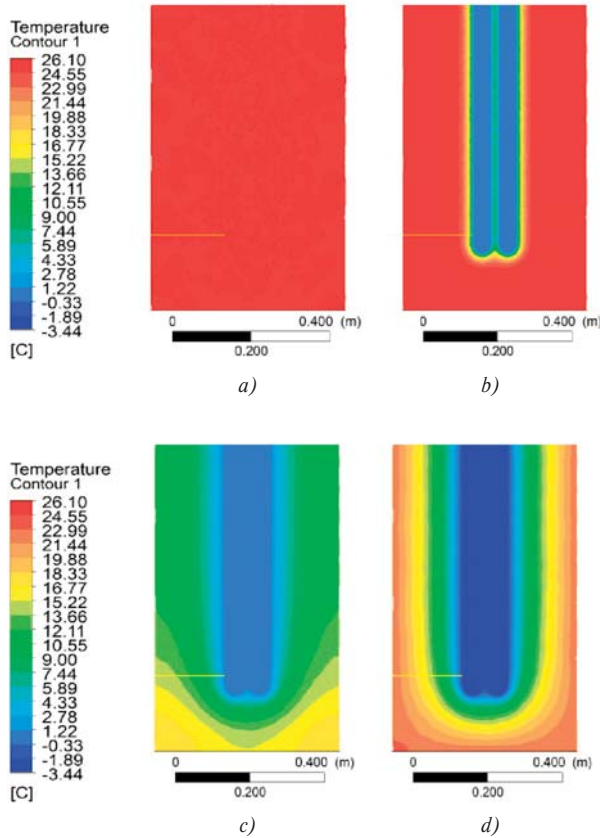


Fig. 14 Results of individual simulation steps (a - 0 s, b - after 10 min., c - after 19 hrs and d - after 48 hrs)

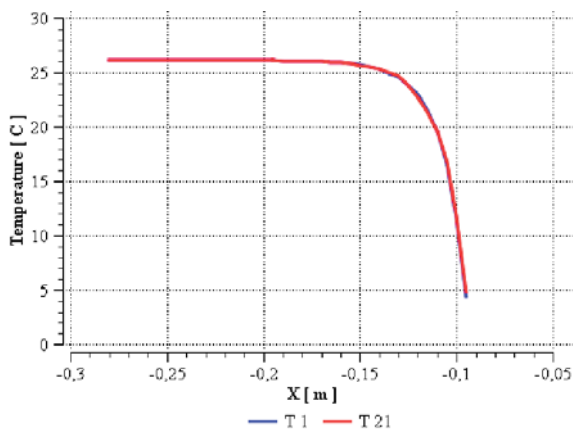


Fig. 15 Simulation result after 10 min

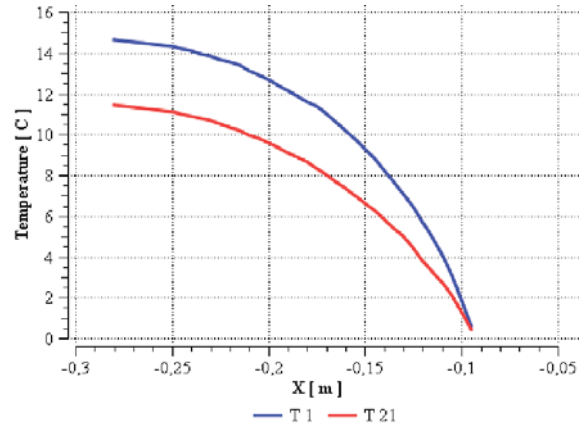


Fig. 16 Simulation result after 19 hours

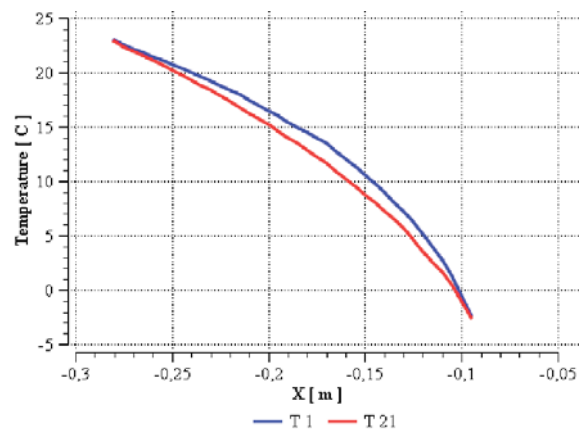


Fig. 17 Simulation result after 48 hours

5. Discussion

The designed equipment (simulator) for heat transport enables a relevant comparison of the thermal power transmitted from the rock heat by means of the U-ground heat exchangers and by means of heat pipes with thermo-siphon effect under the same conditions. This problem cannot be solved in a classical borehole since rock characteristics differ from one borehole to another. The presented simulator is a suitable device for testing the heat potential of geothermal borehole. Based on the known parameters of the rock (thermal conductivity, capacity, rock moisture) it is possible to verify the measured heat outputs during the testing of the borehole potential (from the temperature and flow of tested fluid) and to find the dependence between the characteristic of borehole soil and their temperatures.

6. Conclusion

The paper describes the construction design, schemes and connection of the simulator geothermal borehole model located

in the laboratory, a creation of CFD model simulator and CFD simulation results of the model simulator in which the transfer of low potential geothermal energy was simulated. The CFD simulations results were compared with a real simulator. Comparison of simulation results showed that they are in good agreement with the results of measurements. The device for simulation of low potential geothermal heat allows to mimic the processes taking place in deep boreholes. Examining these processes in laboratory conditions allows getting some knowledge of a suitable heat carrier, soil conductivity, etc.

In laboratory conditions it is possible to achieve the carbon dioxide saturation point through changes in CO_2 pressure and

temperature. If we are able to maintain this condition and simultaneously accumulate heat to the borehole, we can provide a long-term heat take away in the exchanger. In real conditions when the seasons change, this is not possible. Carbon dioxide as the working substance in heat tubes works without forced circulation and has the potential to be used in real boreholes.

Acknowledgement

This article has been prepared within the framework of the operational program Research and Development - ITMS-26220220057 "Device for the use of low-potential geothermal heat without forced circulation of the heat carrier in deep boreholes".

References

- [1] <http://devi.danfoss.com/Slovakia/Consumer/FloorHeatingForHome/Products>
- [2] CAPLA, L., KOUTSKY, B., BURYAN, P.: *Technical Report No. 10/04 Studies of Dependences Carbon Dioxide Pressure on Temperature*, VSCHT, Prague, 2004.
- [3] <http://www.wolframalpha.com>.
- [4] PETRAS, D.: *Low Temperature Heating and Renewable Energy Sources*. Bratislava: Jaga, 2009. 216 p., ISBN 80-07-00031-5.
- [5] SCHIESTEL, R.: *Modeling and Simulation of Turbulent Flows*. Hoboken: Wiley 2008. ISBN 978-1-84821-001-1.
- [6] LENHARD, R., MALCHO, M.: Numerical Simulation Device for the Transport of Geothermal Heat with Forced Circulation of Media: Elsevier-An International Journal: *Mathematical and Computer Modelling*. - ISSN 0895-7177, doi:10.1016/j.mcm.2011.06.011.
- [7] LENHARD, R., JAKUBSKY, M., NEMEC, P.: *Device for Simulation of Transfer Geothermal Heat with Forced and without Forced Circulation of Heat Carrier*, Fourth Global Conference on PCO 2010, Kuching - Sarawak - Malaysia, 2010, ISBN 978-983-44483-32.
- [8] SCHIESTEL, R.: *Modeling and Simulation of Turbulent Flows*. Hoboken, Wiley 2008, ISBN 978-1-84821-001-1.
- [9] CARNOGURSKA, M., PRIHODA, M., BRESTOVIC, T., MOLINEK J., PYSZKO, R.: Determination of Permeability and Inertial Resistance Coefficient of Filter Inserts Used in the Cleaning of Natural Gas. *Journal of Mechanical Science and Technology*. Vol. 26, 2012, No. 1, pp. 103-111.
- [10] JANDACKA, J., PAPUCIK, S.; DEKYS, V.; MELICHER, R.: An Analysis of Air Flow at Various Spacing of Fans on a Physical Model of a Road Tunnel, *Communications - Scientific Letters of the University of Zilina*. ISSN 1335-4205. Vol. 10, No. 3 (2008), pp. 40-44.
- [11] BRESTOVIC, T., CARNOGURSKA, M., PYSZKO, R., KUBIK, M.: Effect of Radiation on Heat Exchange in Finned Heat Transfer Surfaces. In: *AEaNMiFMaE* 2012, p. 19-26, ISBN 978-80-554-0516-2.

Maria Carnogurska – Miroslav Prihoda *

PHYSICAL MODELING OF FLOW IN A TUNDISH FOR CONTINUOUS CASTING MACHINE

The paper describes a procedure for obtaining similarity criteria for a real object – a tundish for continuous casting machine (CCM) and its reduced physical model. The procedure is demonstrated on the basis of Navier-Stokes differential equations and with the help of dimensional analysis. To obtain similarity criteria dimensional analysis makes use of dimensions of those physical quantities which significantly influence the mentioned phenomenon. From the above it results that when modeling a concrete phenomenon with the help of this method it is inevitable to thoroughly know the physical substance of the phenomenon to expressly ensure the choice of all relevant quantities. On the basis of elaborated model laws the basic characteristics of flow (rate, flow volume, time intervals) were designed for the reduced model of the real CCM. The obtained dependences of characteristics feature the universal validity for all the models of tundishes.

Keywords: liquid iron, flow, modeling, similarity criteria.

1. Introduction

At continuous casting of steel the full ladle is put on a rotating turret of the casting machine. The ladle shroud having been set and ladle slide gate having been opened, the tundish starts being filled until the required surface height is achieved [1]. Discharge from the tundish to the mould is in the case of submerged casting usually stopper controlled; in the case of open stream casting it is given by the diameter of the nozzle and casting speed. The tundish is one of the basic parts of the casting machine as it fulfils various important functions. Its size is usually 8 – 10 % of the ladle. In the case of CCM for billets steel from one tundish is distributed into as many as six molds. When there are more strands, the casting machine makes use of two tundishes [2, 3 and 4]. The requirements put on the tundish result into different demands put on its shape, arrangement as well as size due to the fact that some of the required functions oppose each other. For example, more perfect homogenization of chemical composition and temperature of steel are achieved at intensive mixing of the molten metal; on the other hand, possibilities of inclusions washing-out and their subsequent trapping in cover slag are getting worse. Although a larger volume of the tundish contributes to a better separation of non-metallic inclusions, it also prolongs non-stationary states at exchanges of a ladle [5, 6, 7 and 8].

The authors are not aware of the fact that the complicated phenomenon of steel flow modeling in the tundish in reduced physical models has been described on the basis of criterion equations in such a way as it is presented in this paper. General information on modeling can be found in some publications [9, 10 and 11]. This article presents the flow process in a tundish analyzed by means of similarity criteria characterizing the most general fluid

motion. Consequently, the criteria that are irrelevant for steel flow in the tundish were omitted [12]. All similarity criteria will be derived by means of two methods – from differential equations and on the basis of dimensional analysis [13, 14, 15 and 16].

2. Analytical method of determining similarity criteria from Navier-Stokes equations

Navier-Stokes differential equations are the most general equations of unsteady spatial isothermal motion of real, i. e., viscous fluid. They express the equilibrium of unit forces of mass (a), pressure ($\partial p / (\rho \cdot \partial y)$), friction ($\nu \cdot \nabla^2 v$) and inertia ($Dv_y / d\tau$). Making use of so called complete (total, substitution) derivation of velocity components and referring forces to the unit of mass, we get the below relation for the axis x

$$a_x - \frac{1}{\rho} \cdot \frac{\partial p}{\partial x} + \nu \cdot \nabla^2 v_x = \frac{Dv_x}{d\tau} \quad (\text{m} \cdot \text{s}^{-2}) \quad (1)$$

Similar relations hold for two other coordinate axes. In the vector record it is the relation in the form

$$a - \frac{1}{\rho} \cdot \mathbf{grad} p + \nu \cdot \nabla^2 \mathbf{v} = \frac{D\mathbf{v}}{d\tau} \quad (\text{m} \cdot \text{s}^{-2}) \quad (2)$$

Considering the most common case of force field of the Earth's gravity, then acceleration a in equation (2) is replaced by gravitational acceleration g , or by its components. Equation (2) has to hold both for the *model* and for the *real object*. When equation (1) is rewritten with appropriate similarity constants of quantities “ c ” (quantity in the real object D to the magnitude in the model M) we get the below relation for the axis x

* Maria Carnogurska¹, Miroslav Prihoda²

¹ Department of Power Engineering, Faculty of Mechanical Engineering, Technical University of Kosice, Slovakia, E-mail: maria.carnogurska@tuke.sk

² Faculty of Metallurgy and Materials Engineering, VSB – Technical University of Ostrava, Ostrava-Poruba, Czech Republic

$$c_g \cdot a_y - \frac{c_p}{c_\rho \cdot c_l} \cdot \frac{1}{\rho} \cdot \frac{\partial p}{\partial y} + \frac{c_v \cdot c_\nu}{c_l^2} \cdot \nu \left(\frac{\partial^2 v_y}{\partial x^2} + \frac{\partial^2 v_y}{\partial y^2} + \frac{\partial^2 v_y}{\partial z^2} \right) = \frac{c_v}{c_\tau} \cdot \frac{\partial v_y}{\partial \tau} + \frac{c_v^2}{c_l} \left(v_x \frac{\partial v_y}{\partial x} + v_y \frac{\partial v_y}{\partial y} + v_z \frac{\partial v_y}{\partial z} \right) \quad (3)$$

where c_g - scale of change in gravitational acceleration, c_p - scale of change in pressure, c_ρ - scale of change in density, c_l - scale of change in length, c_ν - scale of change in kinematic viscosity, c_v - scale of change in velocity.

Similar equation can be written for two other axes. When equation (3) is divided by member c_v^2/c_l , we get the relation and similarly also for the axes x and z .

$$\frac{c_g \cdot c_l}{c_v^2} \cdot a_y = \frac{c_p}{c_\rho \cdot c_v^2} \cdot \frac{1}{\rho} \cdot \frac{\partial p}{\partial y} + \frac{c_v}{c_l} \cdot \nu \left(\frac{\partial^2 v_y}{\partial x^2} + \frac{\partial^2 v_y}{\partial y^2} + \frac{\partial^2 v_y}{\partial z^2} \right) = \frac{c_l}{c_v \cdot c_\tau} \cdot \frac{\partial v_y}{\partial \tau} + \left(v_x \frac{\partial v_y}{\partial x} + v_y \frac{\partial v_y}{\partial y} + v_z \frac{\partial v_y}{\partial z} \right) \quad (4)$$

Equation (4) holds for all groups of mutually similar hydrodynamic phenomena. As long as equations (1) and (4) are to represent both the model and reality, they have to be identical [10]. For indicators of model and real object similarities the following equation can be written

$$\frac{c_l}{c_\tau \cdot c_v} = \frac{c_g \cdot c_l}{c_v^2} = \frac{c_p}{c_\rho \cdot c_v^2} = \frac{c_v}{c_l \cdot c_l} = 1 \quad (5)$$

From the indicators four similarity criteria can be derived in the form

$$\pi_1 = \frac{l}{\tau \cdot v}, \quad \pi_2 = \frac{g \cdot l}{v^2}, \quad \pi_3 = \frac{p}{\rho \cdot v^2}, \quad \pi_4 = \frac{\nu}{v \cdot l} \quad (6)$$

Individual criteria have the following meaning

$$\pi_1 = \frac{l}{\tau \cdot v} = Ho^{-1}$$

reciprocal of homochronism criterion (Strouhal's number) (7)

$$\pi_2 = \frac{g \cdot l}{v^2} = Fr^{-1}$$

reciprocal of the Froude criterion (8)

$$\pi_3 = \frac{p}{\rho \cdot v^2} = Eu$$

Euler's criterion (9)

$$\pi_4 = \frac{\nu}{v \cdot l} = Re^{-1}$$

reciprocal of the Reynolds criterion (10)

The general criterion equation of spatial isothermal motion of incompressible viscous fluid derived from Navier-Stokes differential equations has then the following form

$$f(Ho, Fr, Eu, Re) = 0 \quad (11)$$

The system of differential Navier-Stokes equations expresses a whole group of phenomena and that is why it has an indefinite number of solutions. Equation (11) can express a mechanical sim-

ilarity of the real object to its reduced model only when starting equations will have an unambiguous solution. It can be achieved only when we add to the system of differential equations such conditions which will lead to an only solution expressly characterizing the observed phenomenon, i. e. conditions of one single meaning. The conditions have to contain geometry of space, physical properties of the ambient in which the observed phenomenon develops as well as values of variable quantities on the boundary of the

system and in the initial moment of the observed phenomenon. Boundary conditions have to guarantee constant values of similarity constants for each of variable quantities occurring on the boundary of the process. As for the initial conditions it is necessary to keep constant values of constants of proportion in all relevant quantities of the phenomenon. When comparing two phenomena we find out that similarity indicators formed from similarity constants are equal to one, such phenomena can be referred to as similar.

3. Analytical method of deriving similarity criteria with the help of dimension analysis

Physical quantities that influence isothermal motion of fluid are:

- kinematic viscosity ν ($m^2 \cdot s^{-1}$),
- density ρ ($kg \cdot m^{-3}$),
- rate of flow v ($m \cdot s^{-1}$),
- gravitational acceleration g ($m \cdot s^{-2}$),
- length l (m),
- pressure p ($kg \cdot m^{-1} \cdot s^{-2}$),
- time τ (s).

The complete physical equation characterizing dependence of mentioned physical quantities has the following form

$$\varphi(\nu, \rho, v, g, l, p, \tau) = 0 \quad (12)$$

Equation (12) is dimensionally homogeneous; therefore, individual physical quantities cannot occur in it independently, only in the form of products [15, 16]

$$\pi_i = v^{x_1} \cdot \rho^{x_2} \cdot \nu^{x_3} \cdot g^{x_4} \cdot l^{x_5} \cdot p^{x_6} \cdot \tau^{x_7} \quad (13)$$

where exponents x_1, x_2, \dots, x_7 are unknown and will have to be determined later.

Dimensional matrix for the basic unit will consist of $n = 7$ columns and a total of $m = 3$ lines and has the form

$$\begin{matrix} & \nu & \rho & \nu & g & l & p & \tau \\ \text{kg} & \parallel & 0 & 1 & 0 & 0 & 0 & 1 & 0 \\ \text{m} & \parallel & 2 & -3 & 1 & 1 & 1 & -1 & 0 \\ \text{s} & \parallel & -1 & 0 & -1 & -2 & 0 & -2 & 1 \end{matrix} \quad (14)$$

When the matrix rank $h = 3$ and number of relevant quantities $n = 7$ it is possible to create the total of $l = n - h$, i. e. 4 dimensionless arguments π . For calculation of unknown ($x_i > m$) the rectangular dimensional matrix A is divided into two parts; similarly we proceed when dividing the vector of unknown quantities x_i . The first part of the matrix is square with a number of h columns and h lines, while the matrix columns have to be chosen so that its determinant will be nonzero ($\Delta \neq 0$). This also complies with division of vectors x_i .

The shape of square matrix A and vector of unknown quantities x_i from equation (14) will be arranged and written in a simplified form

$$\mathbf{A} \cdot \mathbf{B} = (-1) \cdot \mathbf{D} \cdot \mathbf{E} \quad (15)$$

Matrix (15) in an itemized form for individual dimensions is as follows

$$\begin{matrix} \parallel & 1 & 0 & 0 \\ \parallel & -3 & 1 & 1 \\ \parallel & 0 & -1 & 0 \end{matrix} \cdot \begin{matrix} \parallel & x_2 \\ \parallel & x_3 \\ \parallel & x_5 \end{matrix} = (-1) \begin{matrix} \parallel & 0 & 0 & 1 & 0 \\ \parallel & 2 & 1 & -1 & 0 \\ \parallel & -1 & -2 & -2 & 1 \end{matrix} \cdot \begin{matrix} \parallel & x_1 \\ \parallel & x_4 \\ \parallel & x_6 \\ \parallel & x_7 \end{matrix} \quad (16)$$

Determinant of matrix A is determined, for example, on the basis of Laplace development and has to be $\neq 0$.

$$\Delta_A = \Sigma(-1)^{i+j} = a_{ij} \cdot M_{ij} \quad (17)$$

where

a_{ij} is the element in the i th line and j th column,
 M_{ij} - subdeterminant of the matrix in which the i th line and j th column are omitted. The value of matrix determinant is $\Delta_A = 1$, by which the solvability condition has been fulfilled.

Choice of redundant unknowns x_1, x_4, x_6, x_7 is repeated four times paying attention to the fact that the choices have to be linearly independent. The selection matrix has the following form

	x_1	x_4	x_6	x_7
1st choice	1	0	0	0
2nd choice	0	1	0	0
3rd choice	0	0	1	0
4th choice	0	0	0	1

(18)

and its determinant has the value $\Delta = 1$, by which the solvability condition has been fulfilled.

Transformation of equation (16) to the system of linear equation is in the form

$$\begin{aligned} x^2 &= -x_6 \\ -3 \cdot x_2 + x_3 + x_5 &= -2 \cdot x_1 - x_4 + x_6 \\ -x_3 &= x_1 + 2 \cdot x_4 + 2 \cdot x_6 - x_7 \end{aligned} \quad (19)$$

Solving the system of linear equations (19) we get the following similarity criteria

	x_1	x_2	x_3	x_4	x_5	x_6	x_7
π_1	1	0	-1	0	-1	0	0
π_2	0	0	-2	1	1	0	0
π_3	0	-1	-2	0	0	1	0
π_4	0	0	1	0	-1	0	1

(20)

Dimensionless arguments themselves have the form

$$\pi_1 = \frac{\nu}{\nu \cdot l}, \pi_2 = \frac{g \cdot l}{\nu^2}, \pi_3 = \frac{p}{\rho \cdot \nu^2}, \pi_4 = \frac{\tau \cdot \nu}{l} \quad (21)$$

From the way in which the criteria are derived results that all the expressions in (21) are dimensionless numbers, which can be easily verified by substituting dimension of individual quantities. Dimensionless form of the function describing steel flow can be written in the form

$$\varphi(\pi_1, \pi_2, \pi_3, \pi_4) = 0 \quad (22)$$

The acquired criteria in equation (22) one after the other are: reciprocal of the Reynolds criterion Re^{-1} , reciprocal of the Froude criterion Fr^{-1} , Euler's criterion Eu and homochronism criterion Ho , and expression (22) can also be written as

$$\varphi(Re, Fr, Eu, Ho) = 0 \quad (23)$$

As can be seen from comparison of relations (23) a (11) when looking for conditions of mechanical similarity of flow with the help of dimension analysis, two identical similarity numbers were achieved equally as when using the analysis method of Navier-Stokes differential equations.

4. Similarity between the model and real object

Physical similarity between the model and real object should be guaranteed by equal similarity criteria both in the real object and model. In the case of a steel flow simulation in the tundish four similarity criteria were derived - equations (21) or (23).

Homochronism criterion

also known as Strouhal's criterion (Sh), which apart from inertia force contains also impulse force, i. e. force related to the change of motion, is used for expression of dimensionless time. It can also be understood in such a way that the relative unit of measurement is time which fluid particles moving at the speed ν need to cover the path l . If it refers to the process which is stationary, i. e. the

process at the constant speed, the criterion Ho becomes irrelevant and equation (23) will be simplified and will have the form

$$\varphi(Re, Fr, Eu) = 0 \tag{24}$$

Euler's criterion

that includes forces of pressure and inertia serves for determination of pressure losses in the forced flow. This similarity number is significant especially when solving flow in pipes. For the flow in open channels, which is the case of motion of molten steel in the tundish, pressure losses are negligible. The Euler's number can therefore be omitted from relation (23) and the criterion equation gets the form

$$\varphi(Re, Fr) = 0 \tag{25}$$

Reynolds criterion

expressing the ratio of inertia to friction forces characterizes the flow of real liquid which is either laminar or turbulent. Transition from laminar to turbulent flow occurs at the critical value of the Reynolds criterion denoted Re_{kr} . If for a particular case $Re > Re_{kr}$, the flow is turbulent; if $Re < Re_{kr}$ the flow is laminar.

The similarity condition between the model (M) and real object (D) is by means of this criterion expressed as follows

$$Re_M = Re_D, \text{ or } Re = Re' \tag{26}$$

The similarity condition for the real object (tundish) and model (reduced tundish) - relation (26) - can be written as follows

$$\frac{\nu \cdot l}{\nu'} = \frac{\nu' \cdot l'}{\nu'}$$

The below mentioned expression must hold for the similarity constants

$$\frac{c_v}{c_l} = c_l^{-1} \tag{27}$$

If the kinematical viscosity of liquids both in the real object and in the model is identical, i. e., if $c_v = 1$, then equation (27) is simplified to the form

$$c_v = c_l^{-1} \tag{28}$$

For the model of the tundish ten times smaller than the real object holds that the scale of change in length is $c_l = 10$. To satisfy equation (28) it has to be $c_v = 0.1$, which means that velocity in the model diminished in this way would be ten times greater than the one in the real object. If the model fluid had ten times smaller kinematical viscosity than the real object liquid, the following would hold $c_v = 1$, i. e., velocity in the model would be equal to the real object velocity.

Froude criterion

represents the ratio of inertia to mass forces. If the equality of number Fr is kept at modeling, then the following holds

$$Fr_D = Fr_M \text{ resp. } \frac{\nu'^2}{g' \cdot l'} = \frac{\nu^2}{g \cdot l} \tag{29}$$

For particular similarity constants we then get

$$c_v^2 = c_g \cdot c_l \tag{30}$$

The processes in the model as well as those in the real object will take place under earth gravitation, i. e.

$$g = g \Rightarrow c_g = 1$$

so equation (30) then has, at the similarity constant of gravitation acceleration $c_g = 1$, the form

$$c_v^2 = c_l \text{ resp. } c_v = \sqrt{c_l} = c_l^{1/2} \tag{31}$$

If the Froude criterion is applied to the model in the same diminishment as the Reynolds criterion, i. e. in the scale 10:1, the rates in the model are 3.16 times smaller than those in the real object. Comparing the conditions of Froude and Reynolds similarities we can see that the modeling of motion phenomena at keeping number Fr is substantially simpler because the required rates of flow in the model are lower than those in the real object. When modeling according to Re the situation is opposite. Similar unfavorable ratio is also in volume flows, which often leads to serious technical problems. Comparing relations (28) and (31) we can see that both of them can simultaneously hold only at the length scale $c_l = 1$, i. e. in the case when both the model and real object have the same dimensions.

When using in the reduced model of the tundish the fluid with the same kinematical viscosity as the one used in the real object, the below condition cannot be satisfied

$$Re' = Re \wedge Fr' = Fr \tag{32}$$

Theoretically, the current equality of both criteria in the model and in real object can be ensured with the choice of such model liquid for which equation (33) will hold for kinematical viscosity

$$c_v = c_l \cdot \sqrt{c_l} = c_l^{3/2} \tag{33}$$

To achieve the *total mechanical similarity* between two hydrodynamic phenomena in the modeling research requires the use of such liquid which will guarantee simultaneous satisfaction of equality of all necessary similarity criteria both in the model and in the real object [17]. However, it is impossible to find two liquids that feature such physical characteristics to satisfy the mentioned conditions. That is why the *approximate mechanical similarity* has to be used when some criteria are considered irrelevant.

As we have already mentioned, when modeling the flow of liquid steel in the tundish it is possible to omit the criteria Ho and Eu . It has also been mentioned that in practice the condition (32), which is simultaneous equality of numbers Re and Fr , can hardly be satisfied. Concretely, in a ten times smaller model it would be

necessary to work with modeling fluid which would, in comparison with fluid in the real object, feature 31.6 times smaller kinematical viscosity. For modeling the fluid steel flow it would be required to use fluid featuring kinematical viscosity of order $10^{-8} \text{ m}^2 \cdot \text{s}^{-1}$. At the same time it has to be said that fluid featuring such kinematical viscosity at usual ambient temperatures practically does not exist.

If considering realistic possibilities of choice of model liquid which would, apart from certain physical characteristics, feature an easily accessible price, satisfy hygienic standards, and be easily stored then, it is water that can be used for flow modeling. Another advantage of water also is that its kinematical viscosity at the usual ambient temperature does not differ from kinematical viscosity of molten steel; they both are about the value of $1 \cdot 10^{-6} \text{ m}^2 \cdot \text{s}^{-1}$.

Referring to the above mentioned facts it is obvious that at modeling the molten steel flow in the tundish for continuous steel pouring machine it is desired to decide which criterion will be chosen as determining – the Froude or Reynolds criterion.

When comparing both similarity criteria we can see that for the physical model of steel flow in tundish for continuous steel pouring machine it is more convenient to prioritize the *Froude criterion*. Kinematically similar motion phenomena which are exclusively or predominantly influenced by the gravitation force are also dynamically similar when they have the same values *Fr* in mutually corresponding cross sections of both real object and model.

5. Results and discussion

Research into flow similarities in a diminished model of the tundish comes out from geometrical similarity as the basis for mechanical similarity. Apart from the similarity constant of velocity expressed by relation (31), which is written in the following way

$$c_v = \frac{v'}{v} = c_l^{1/2} \tag{34}$$

it is possible to define other similarity constants for the model and the real object, which is the similarity constant of volume flow

$$c_{Q_v} = \frac{Q'_v}{Q_v} = \frac{S' \cdot v'}{S \cdot v} = c_l^2 \sqrt{c_l} = c_l^{5/2} \tag{35}$$

and similarity constant of time intervals

$$c_\tau = \frac{c_l}{c_v} = \frac{c_l}{\sqrt{c_l}} = c_l^{1/2} \tag{36}$$

Applying the derived similarity constants of individual quantities to the tundish for a six-strand continuous casting machine (Fig. 1) casting billets having a cross section of $180 \times 180 \text{ mm}$ at the rate of $2.1 \text{ m} \cdot \text{min}^{-1}$ we can obtain the following information.

Mass flow of steel (oc) from the ladle to the tundish is

$$\begin{aligned} Q_{m,oc} &= 6 \cdot S \cdot v \cdot \rho = 6 \cdot 0.18 \cdot 0.18 \cdot 2.1 \cdot 7800 = \\ &= 3184 \text{ kg} \cdot \text{min}^{-1} \end{aligned}$$

where

- v* – pouring rate ($\text{m} \cdot \text{min}^{-1}$),
- ρ – density of steel at normal temperature ($\text{kg} \cdot \text{m}^{-3}$),
- S* – cross section of raw casting (m).

Volume flow of steel from the ladle to the tundish

$$\begin{aligned} Q_{v,oc} &= \frac{Q_{m,oc}}{\rho_l} = \frac{3184}{6900} = 0.4615 \text{ m}^3 \cdot \text{min}^{-1} = \\ &= 461.5 \text{ l} \cdot \text{min}^{-1} \end{aligned}$$

where

- ρ_l – density of molten steel ($\text{kg} \cdot \text{m}^{-3}$).

When a reduced model of a tundish is in the scale 10:1, it will hold that $c_l = 10$; then, in compliance with equation (35) the volume flow of water (in) into the model is equal to

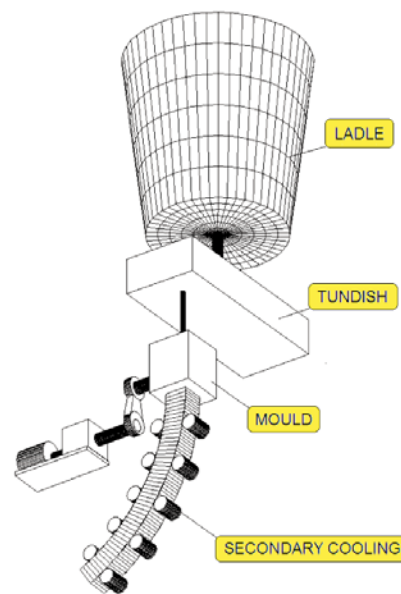


Fig. 1 Schematic diagram of a CCM [18]

$$Q_{v,vo} = \frac{Q_{v,oc}}{c_l^{5/2}} = \frac{461.5}{10^{5/2}} = 1.46 \text{ l} \cdot \text{min}^{-1}$$

and, therefore, it will be 316-times smaller than the volume flow of molten steel in the real tundish (Fig. 2). The place in the figure is marked with a circle on the axis *y*. The figure presents the dependence of the ratios of volume flows on the reduction scale within the scales 10:1 to 1:1, which represents the congruence of the model and real object. Water flow rate in the ten times smaller model will be 3.16 times smaller than steel flow rate in the tundish, i. e. its value is $0.66 \text{ m} \cdot \text{s}^{-1}$ and time intervals in the model will be 3.16-times smaller than those in the real tundish. At the same time the figure presents the dependence of the ratios of flow rate and time intervals to the scale of the model reduction within the same boundaries as in volume flows.

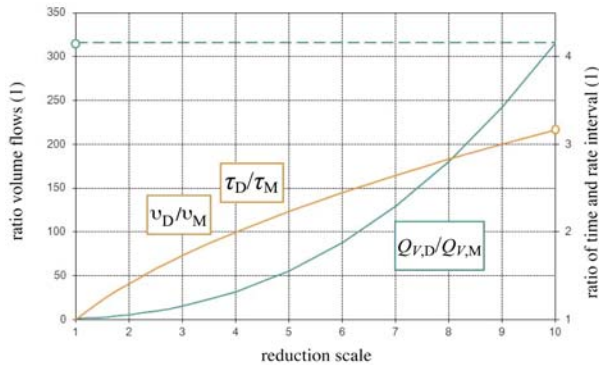


Fig. 2 Dependence of ratio of volume flows, rate and time intervals on the scale of reduction

If the model of the tundish is in the scale, e. g. 8:1, the volume water flow will be $2.55 \text{ l}\cdot\text{min}^{-1}$ (181-times smaller than molten steel flow in the tundish), flow rates will be 2.83-times smaller than the rates of molten steel in the real object and time intervals in the model will be 2.83-times shorter. For the model of the tundish in the scale 5:1 similar values for volume flow will be equal to $8.26 \text{ l}\cdot\text{min}^{-1}$ (55.9-times shorter than the volume flow of molten steel in the tundish), flow rates will be 2.24-times smaller

and times will be 2.24-times shorter. If the model is designed in other scale of lengths, the scale for other quantities will be determined from Fig. 2.

6. Conclusions

There is no doubt about advantages of modeling of continuous steel casting in laboratory conditions. Approximate mechanical similarity is applied in the presented procedure of isothermal modeling of molten steel flow in the tundish. Water was chosen as the model fluid due to its physical characteristics.

In the paper we present the process of determining volume flow of water in the reduced laboratory model of the tundish for a six-strand continuous machine whose geometrical similarity to the real object was given in the scales from 10:1 to 1:1. Respecting derived similarity constants of individual physical quantities, results of this analysis can be applied also for an arbitrary number of strands in a pouring machine or for two tundishes.

Acknowledgements

The publication is based on the solution of the partial problem of grant project VEGA No. 1/0006/11, KEGA 045-015TUKE-4/2010 and SP2011/29-FMMI VŠB TUO.

References

- [1] STRANSKY, K., KAVICKA, F., SEKANINA, B., STETINA, J., MAUDER, T., STRANSKY, L.: *Acta Metallurgica Slovaca*, vol. 16, No. 4, 2010, pp. 216-222.
- [2] DOLEJSI, Z., REDR, M., PRIHODA, M., MOLINEK, J., JURECKA, P.: *Continuous Steel Casting*. Prague, TEVUH, 1987, 383 p. (in Czech).
- [3] DOLEJSI, Z., PRIHODA, M., MOLINEK, J., JURECKA, P., VESELY, K.: *Continuous Steel Casting*. 2nd, vol. Prague, TEVUH, 1988, 191 p. (in Czech).
- [4] PRIHODA, M., BAZAN, J., DOBROVSKA, J., JELINEK, P., JONSTA, Z., VROZINA, M.: *New Knowledge from Research into Continuous Steel Casting*. Ostrava : VSB-TU Ostrava, 2001, 177 p. (in Czech).
- [5] MOLINEK, J., VACLAVIK, L., KLIMSZOVA, A., PRIHODA, M.: *Acta Metallurgica Slovaca*, vol. 13, No. 5, 2007, pp. 355-360 p. (in Czech).
- [6] PRIHODA, M., MOLINEK, J., PYSZKO, R., FOJTIK, P.: *Acta Metallurgica Slovaca*, vol. 10, No. 3 (special issue), pp. 434-438 (in Czech).
- [7] ABOUTALEBI REZA, M., HASAN, M., GUTHRIE, L. I. R.: *Metallurgical and Materials Transactions B*, 1995, No. 26B, pp. 731-744.
- [8] HUESPE, E. A., CARDONA, A., FACHINOTTI, V.: *Computer Methods in Applied Mechanics and Engineering*, 2000, No. 182, pp. 439-455.
- [8] PASCON, F., HABRAKEN, A., BLES, G.: *J. de Physique IV*, 2004, vol. 120, pp. 447-455.
- [9] PRIHODA, M., MOLINEK, J., DITTEL, D., VACULIK, M., FOJTIK, P.: *Acta Metallurgica Slovaca*, vol. 13, 2007, No. 3, pp. 311-316 (in Czech).
- [10] PRIHODA, M., JURECKA, P., MOLINEK, J., REDR, M., TLUSTY, R.: *Hutnicke listy XXXX*, 1985, No. 7, pp. 491-497, (in Czech).
- [11] SANTOS, A. C. , SPIM, A. J., GARCIA, A.: *Engineering Applications of Artificial Intelligence*, vol. 16, No. 16, 2003, pp. 511-527.
- [12] CARNOGURSKA, M., PRIHODA, M.: *Application of Dimensional Analysis in Energetic*. Viena, Kosice, 2011, 214 p. (in Slovak).
- [13] CARNOGURSKA, M., PRIHODA, M., BRESTOVIC, T.: *Chemical and Process Engin.*, vol. 32, No. 3, 2011, pp. 175-184, DOI: 10.2478/v10176-011-0013-7.
- [14] CARNOGURSKA, M., PRIHODA, M., POPCAKOVA, D.: *J. of Mechanical Science and Technology*, vol. 24, 2010, No. 12, pp. 2479-2486.
- [15] LANGHAR, H. L.: *Dimensional Analysis and Theory of Models*. Malabar : Robert E. Krieger Publishing Company, 1987 (in Czech).

- [16] BARENBLATT, G. I.: *Dimensional Analysis*. New York : London : Paris : Montreaux : Tokyo: Gordon and Breach Science Publishers, 1987.
- [17] VOJSOVICOVA, M., LIPTAKOVA, T., ZATKALIKOVA, V.: *Rheological Characteristics of Thermoplastic Polymers after Degradation*, Communications: Scientific Letters of the University of Zilina. - ISSN 1335-4205. - vol. 13, No. 4 (2011), pp. 32-35.
- [18] PYSZKO, R.: *Research into Working Conditions in Crystallizer at Continuous Steel Casting*. Doctoral dissertation. VSB-TU Ostrava, 1993, 133 p., (in Czech).

Milan Zmindak – Daniel Riecky *

MESHLESS MODELLING OF LAMINATE MINDLIN PLATES UNDER DYNAMIC LOADS

Collocation method and Galerkin method have been dominant in the existing meshless methods. A meshless local Petrov-Galerkin (MLPG) method is applied to solve laminate plate problems described by the Reissner-Mindlin theory for transient dynamic loads. The Reissner-Mindlin theory reduces the original three-dimensional (3-D) thick plate problem to a two-dimensional (2-D) problem. The bending moment and the shear force expressions are obtained by integration through the laminated plate for the considered constitutive equations in each lamina. The weak-form on small subdomains with a Heaviside step function as the test functions is applied to derive local integral equations. After performing the spatial MLS approximation, a system of ordinary differential equations of the second order for certain nodal unknowns is obtained. The derived ordinary differential equations are solved by the Houbolt finite-difference scheme as a time-stepping method.

Keywords: Local integral equations, Reissner-Mindlin plate theory, MLS approximation, orthotropic material properties

1. Introduction

Composite materials are now common engineering materials used in a wide range of applications. They play an important role in the aviation, aerospace and automotive industry, are also used in the construction of ships, submarines, nuclear and chemical facilities, etc. During the last several decades, laminated composite plates have been widely used in engineering structures. The optimization of the topology of structural lay out and composite plates and shells has great impact on the performance of structures [1-3].

Previous research results show that the transverse shear effects are more significant for orthotropic plates than for isotropic ones [4, 5]. It is well known that the classical thin plate theory of Kirchhoff gives rise to certain non-physical simplifications mainly related to the omission of the shear deformation and the rotary inertia, which become more significant for increasing thickness of the plate. The effects of shear deformation and rotary inertia are taken into account in the Reissner-Mindlin plate bending theory [6]. A higher-order theory for plates deformed in shear and normal mode was used by Qian et al. [7]. There, the plate material is made of two isotropic constituents and exhibits macroscopically isotropic material properties which vary in the thickness direction only. Results of the static analysis and computed natural frequencies of a simply supported square plate match well with corresponding analytical values.

In addition, the governing equations for thick orthotropic shells are also quite complicated. A review on early applications of BEM to shells is given by Beskos [8]. The analysis of thin elastic plates by the boundary element method (BEM) is a research subject since

many years. Much previous research works have been done for static and dynamic analysis of isotropic thin plates by the BEM [9]. The first application of the boundary integral equation method to Reissner's plate model was given by Van der Ween [10]. Dynamic analysis of elastic Reissner-Mindlin plates was performed by the direct BEM in the frequency domain [11, 12]. All previous BEM applications deal with isotropic Reissner-Mindlin plates. Wang and Huang [13] were the first who applied BEM to orthotropic thick plates.

In spite of the great success of the FEM and the BEM as accurate and effective numerical tools for the solution of boundary or initial-boundary value problems in domains with complex shapes, there is still a growing interest in developing new advanced numerical methods [14, 15]. Meshless approaches for problems of continuum mechanics have attracted much attention during the past decade especially owing to their high adaptivity and low costs to prepare input data for numerical analyses. Many meshless methods are derived from a weak-form formulation on global domain or a set of local subdomains [16, 17]. In the global formulation background cells are required for the integration of the weak-form. In methods based on local weak-form formulation no cells are required and therefore they are often referred to as truly meshless methods. If a simple form is chosen for the geometry of the subdomains, numerical integrations over them can be easily carried out. The first application of a meshless method to plate/shell problems was given by Krysl and Belytschko [18, 19], where they applied the element-free Galerkin method. The Moving Least-Square (MLS) approximation yields a C^1 -continuity which satisfies the Kirchhoff hypotheses. The continuity of the MLS approximation is given by the minimum between the continuity of the basis functions and that of the weight

* Milan Zmindak, Daniel Riecky

Department of Applied Mechanics, Faculty of Mechanical Engineering, University of Zilina, Slovakia, E-mail: milan.zmindak@fstroj.uniza.sk

function. So continuity can be tuned to a desired value. Their results showed an excellent convergence, however, their formulation is not applicable to shear deformable plate/shell problems. Recently, Noguchi et al. [20] used a mapping technique to transform a curved surface into a flat two-dimensional space. Then, the element-free Galerkin method can be applied also to thick plates or shells including the shear deformation effects. The meshless local Petrov-Galerkin (MLPG) method is a fundamental base for the derivation of many meshless formulations, since the trial and the test functions can be chosen from different functional spaces. The method has been successfully applied also to plate and shell problems with homogeneous material properties [21-24].

2. Theory Background of Governing Equations

The classical laminate plate theory is an extension of the classical plate theory to composite laminates. Consider a plate of total thickness h composed of N orthotropic layers with the mean surface occupying the domain Ω in the plane (x_1, x_2) . The $x_3 \equiv z$ axis is perpendicular to the mid-plane (Fig.1). The k -th layer is located between the points $z = z_k$ and $z = z_{k+1}$ in the thickness direction.

The Reissner-Mindlin plate bending theory is used to describe the plate deformation. The transverse shear strains are represented as constant throughout the plate thickness and some correction coefficients are required for the computation of transverse shear forces in that theory. Then, the spatial displacement field in time τ , due to transverse loading and expressed in terms of displacement components u_1, u_2 and u_3 , has the following form [25]

$$\begin{aligned} u_1(\mathbf{x}, x_3, \tau) &= x_3 w_1(\mathbf{x}, \tau), \\ u_2(\mathbf{x}, x_3, \tau) &= x_3 w_2(\mathbf{x}, \tau), \\ u_3(\mathbf{x}, \tau) &= w_3(\mathbf{x}, \tau) \end{aligned} \quad (1)$$

where $x = [x_1, x_2]^T$ is the position vector, and $w_\alpha(x_1, x_2, \tau)$ represent the rotations around the in-plane axes and the out-of-plane deflection, respectively (Fig. 1). The linear strains are given by

$$\begin{aligned} \epsilon_{11}(\mathbf{x}, x_3, \tau) &= x_3 w_{1,1}(\mathbf{x}, \tau) \\ \epsilon_{22}(\mathbf{x}, x_3, \tau) &= x_3 w_{2,2}(\mathbf{x}, \tau) \\ \epsilon_{12}(\mathbf{x}, x_3, \tau) &= x_3 [w_{1,2}(\mathbf{x}, \tau) + w_{2,1}(\mathbf{x}, \tau)]/2 \\ \epsilon_{13}(\mathbf{x}, \tau) &= [w_1(\mathbf{x}, \tau) + w_{3,1}(\mathbf{x}, \tau)]/2 \\ \epsilon_{23}(\mathbf{x}, \tau) &= [w_2(\mathbf{x}, \tau) + w_{3,2}(\mathbf{x}, \tau)]/2 \end{aligned} \quad (2)$$

In the case of orthotropic materials for the k -th lamina, the relation between the stresses σ_{ij} and the strains ϵ_{ij} is described by the constitutive equations for the stress tensor

$$\sigma_{ij}^{(k)}(\mathbf{x}, x_3, \tau) = c_{ijml}^{(k)} \epsilon_{ml}(\mathbf{x}, x_3, \tau) \quad (3)$$

where the material stiffness coefficients $c_{ijml}^{(k)}$ are assumed to be homogeneous for the k -th lamina.

It can be seen from equation (2) that the strains are continuous throughout the plate thickness. Hence, discontinuous material coefficients yield discontinuities in stresses on the lamina surfaces.

For plane problems the constitutive equation (3) is frequently written in terms of the second-order tensor of elastic constants. The constitutive equation for orthotropic materials and plane stress problem are given for example in [23, 26].

Despite the stress discontinuities, one can define the integral quantities such as the bending moments $M_{\alpha\beta}$ and the shear forces $Q_{\alpha\beta}$ as

$$\begin{bmatrix} M_{11} \\ M_{22} \\ M_{12} \end{bmatrix} = \int_{-h/2}^{h/2} \begin{bmatrix} \sigma_{11} \\ \sigma_{22} \\ \sigma_{12} \end{bmatrix} x_3 dx_3 = \sum_{k=1}^N \int_{z_k}^{z_{k+1}} \begin{bmatrix} \sigma_{11} \\ \sigma_{22} \\ \sigma_{12} \end{bmatrix}^{(k)} x_3 dx_3 \quad (4)$$

and

$$\begin{bmatrix} Q_1 \\ Q_2 \end{bmatrix} = \kappa \int_{-h/2}^{h/2} \begin{bmatrix} \sigma_{13} \\ \sigma_{23} \end{bmatrix} dx_3 = \kappa \sum_{k=1}^N \int_{z_k}^{z_{k+1}} \begin{bmatrix} \sigma_{13} \\ \sigma_{23} \end{bmatrix}^{(k)} dx_3, \quad (5)$$

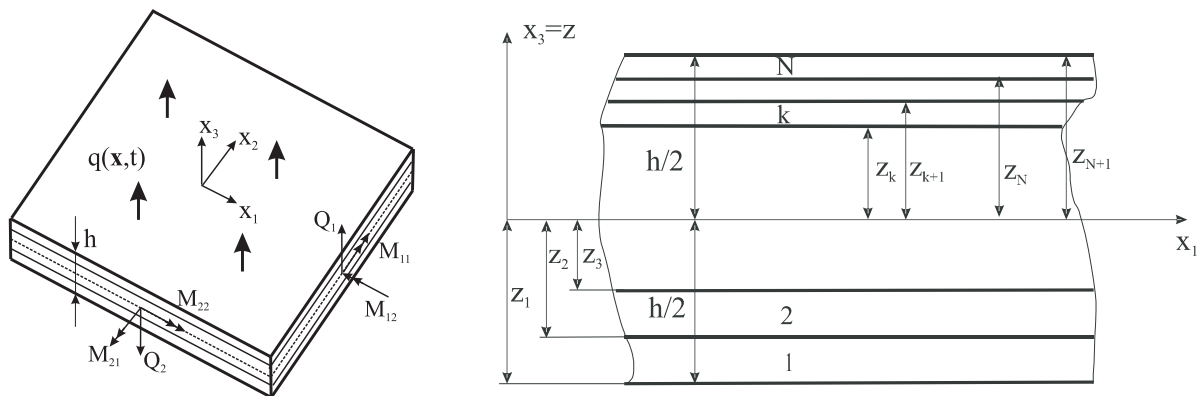


Fig. 1. Definition of bending moments, forces and layer numbering for a laminate plate

where $\kappa = 5/6$ in the Reissner plate theory.

Substituting constitutive equations and (2) into moment and force resultants (5) allows the expression of the bending moments $M_{\alpha\beta}$ and shear forces Q_α for $\alpha, \beta = 1, 2$, in terms of rotations and lateral displacements of the orthotropic plate. In the case of the considered layer-wise continuous material properties through the plate thickness, one obtains

$$M_{\alpha\beta} = D_{\alpha\beta}(w_{\alpha,\beta} + w_{\beta,\alpha}) + C_{\alpha\beta}w_{\gamma,\gamma} \quad (6)$$

$$Q_\alpha = C_\alpha(w_\alpha + w_{3,\alpha}) \quad (7)$$

In eq. (6), repeated indices α and β do not imply summation, and the material parameters $D_{\alpha\beta}$ and $C_{\alpha\beta}$ are given as

$$\begin{aligned} 2D_{11} &= \int_{-h/2}^{h/2} z^2 E_1(z) \frac{1 - \nu_{21}}{e} dz = \\ &= \sum_{k=1}^N \int_{z_k}^{z_{k+1}} E_1^{(k)} \frac{1 - \nu_{21}^{(k)}}{e^{(k)}} z^2 dz = \sum_{k=1}^N E_1^{(k)} \frac{1 - \nu_{21}^{(k)}}{e^{(k)}} \frac{1}{3} (z_{k+1}^3 - z_k^3) \end{aligned}$$

$$\begin{aligned} 2D_{22} &= \int_{-h/2}^{h/2} z^2 E_2(z) \frac{1 - \nu_{12}}{e} dz = \\ &= \sum_{k=1}^N E_1^{(k)} \frac{1 - \nu_{12}^{(k)}}{e^{(k)}} \frac{1}{3} (z_{k+1}^3 - z_k^3) \end{aligned}$$

$$D_{12} = \int_{-h/2}^{h/2} z^2 G_{12}(z) dz = \sum_{k=1}^N G_{12}^{(k)} \frac{1}{3} (z_{k+1}^3 - z_k^3)$$

$$C_{11} = \int_{-h/2}^{h/2} z^2 E_1(z) \frac{\nu_{21}}{e} dz = \sum_{k=1}^N E_1^{(k)} \frac{\nu_{21}^{(k)}}{e^{(k)}} \frac{1}{3} (z_{k+1}^3 - z_k^3)$$

$$C_{22} = \int_{-h/2}^{h/2} z^2 E_2(z) \frac{\nu_{12}}{e} dz = \sum_{k=1}^N E_1^{(k)} \frac{\nu_{12}^{(k)}}{e^{(k)}} \frac{1}{3} (z_{k+1}^3 - z_k^3)$$

$$C_{12} = C_{21} = 0$$

$$\begin{aligned} C_\alpha &= \kappa \int_{-h/2}^{h/2} z^2 G_{\alpha 3}(z) dz = \kappa \sum_{k=1}^N G_{\alpha 3}^{(k)} (z_{k+1} - z_k) e^{(k)} = \\ &= 1 - \nu_{12}^{(k)} \nu_{21}^{(k)}. \end{aligned} \quad (8)$$

For a homogeneous plate equations (8) are reduced into simple forms

$$D_{11} = \frac{D_1}{2}(1 - \nu_{21}), \quad D_{22} = \frac{D_2}{2}(1 - \nu_{12}),$$

$$D_{12} = D_{21} \frac{G_{12} h^3}{12},$$

$$C_{11} = D_1 \nu_{21}, \quad C_{22} = D_2 \nu_{12}, \quad C_{12} = C_{21} = 0,$$

$$D_\alpha = \frac{E_\alpha h^3}{12e}, \quad D_1 \nu_{21} = D_2 \nu_{12}, \quad C_\alpha = \kappa h G_{\alpha 3}$$

$$e = 1 - \nu_{12} \nu_{21} \quad (9)$$

The plate is subjected to a transverse dynamic load $q(\mathbf{x}, t)$. Assuming the mass density to be homogeneous within each lamina and using the Reissner's linear theory of thick plates [25], the equations of motion may be written as

$$M_{\alpha\beta,\beta}(\mathbf{x}, \tau) - Q_\alpha(\mathbf{x}, \tau) = I_m \dot{w}_\alpha(\mathbf{x}, \tau) \quad (10)$$

$$Q_{\alpha,\alpha}(\mathbf{x}, \tau) - q(\mathbf{x}, \tau) = I_Q \ddot{w}_3(\mathbf{x}, \tau), \quad \mathbf{x} \in \Omega \quad (11)$$

where

$$\begin{aligned} I_m &= \int_{-h/2}^{h/2} z^2 \rho(z) dz = \sum_{k=1}^N \int_{z_k}^{z_{k+1}} \rho^{(k)} z^2 dz = \\ &= \sum_{k=1}^N \rho^{(k)} \frac{1}{3} (z_{k+1}^3 - z_k^3), \end{aligned}$$

$$I_Q = \int_{-h/2}^{h/2} \rho(z) dz = \sum_{k=1}^N \int_{z_k}^{z_{k+1}} \rho^{(k)} dz = \sum_{k=1}^N \rho^{(k)} (z_{k+1} - z_k)$$

are global inertial characteristics of the laminate plate. If the mass density is constant throughout the plate thickness, we obtain

$$I_m = \frac{\rho h^3}{12}, \quad I_Q = \rho h.$$

Throughout the analysis, Greek indices vary from 1 to 2, and the dots over a quantity indicate differentiations with respect to time τ .

3. Local Petrov-Galerkin Weak-Form

Instead of writing the global weak-form for the above governing equations, the MLPG methods construct the weak-form over local subdomains such as Ω_s , which is a small region taken for each node inside the global domain [17]. The local subdomains overlap each other and cover the whole global domain Ω (Fig. 2). The local subdomains could be of any geometrical shape and size. In the current paper, the local subdomains are taken to be of circular shape.

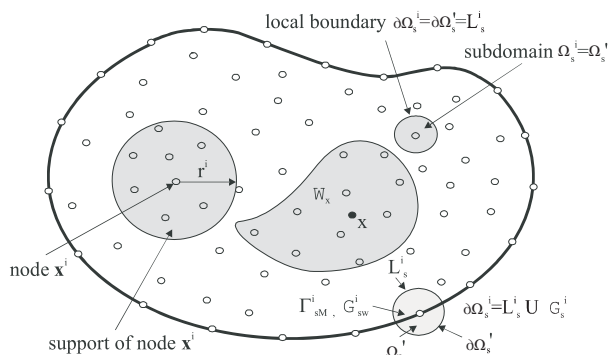


Fig. 2. Local boundaries for weak formulation, the domain Ω_x for MLS approximation of the trial function, and support area of weight function around node x^i

The local weak-form of the governing equations (9) and (10) for $\mathbf{x}^i \in \Omega_s^i$ can be written as

$$\int_{\Omega_s^i} [M_{\alpha\beta}(\mathbf{x}, \tau) - Q_\alpha(\mathbf{x}, \tau) - I_M \ddot{w}_\alpha(\mathbf{x}, \tau)] w_{\alpha\gamma}^*(\mathbf{x}) d\Omega = 0 \quad (12)$$

$$\int_{\Omega_s^i} [Q_{\alpha\alpha}(\mathbf{x}, \tau) - q(\mathbf{x}, \tau) - I_Q \ddot{w}_3(\mathbf{x}, \tau)] w^*(\mathbf{x}) d\Omega = 0$$

here $w_{\alpha\beta}^*(\mathbf{x})$ and $w^*(\mathbf{x})$ are weight or test functions.

Applying the Gauss divergence theorem to Eqs. (11) and (12) one obtains

$$\int_{\partial\Omega_s^i} M_\alpha(\mathbf{x}, \tau) w_{\alpha\gamma}^*(\mathbf{x}) d\Gamma - \int_{\Omega_s^i} M_{\alpha\beta}(\mathbf{x}, \tau) w_{\alpha\gamma, \beta}^*(\mathbf{x}) d\Omega - \int_{\Omega_s^i} Q_\alpha(\mathbf{x}, \tau) w_{\alpha\gamma}^*(\mathbf{x}) d\Omega - \int_{\Omega_s^i} I_M \ddot{w}_\alpha(\mathbf{x}, \tau) w_{\alpha\gamma}^*(\mathbf{x}) d\Omega = 0, \quad (13)$$

$$\int_{\partial\Omega_s^i} Q_\alpha(\mathbf{x}, \tau) n_\alpha(\mathbf{x}) w^*(\mathbf{x}) d\Gamma - \int_{\Omega_s^i} Q_{\alpha\alpha}(\mathbf{x}, \tau) w_{,\alpha}^*(\mathbf{x}) d\Omega - \int_{\Omega_s^i} I_Q \ddot{w}_3(\mathbf{x}, \tau) w^*(\mathbf{x}) d\Omega + \int_{\Omega_s^i} q(\mathbf{x}, \tau) w^*(\mathbf{x}) d\Omega = 0, \quad (14)$$

where $\partial\Omega_s^i$ is the boundary of the local subdomain and $M_\alpha(\mathbf{x}, \tau) = M_{\alpha\beta}(\mathbf{x}, \tau) n_\beta(\mathbf{x})$ is the normal bending moment and n_α is the unit outward normal vector to the boundary $\partial\Omega_s^i$. The local weak-forms (13) and (14) are the starting point for deriving local boundary integral equations on the basis of appropriate test functions. Unit step functions are chosen for the test functions $w_{\alpha\beta}^*(\mathbf{x})$ and $w^*(\mathbf{x})$ in each subdomain

$$w_{\alpha\gamma}^*(\mathbf{x}) = \begin{cases} \delta_{\alpha\gamma} & \text{at } \mathbf{x} \in (\Omega_s \cup \partial\Omega_s) \\ 0 & \text{at } \mathbf{x} \notin (\Omega_s \cup \partial\Omega_s) \end{cases}, \quad (15)$$

$$w^*(\mathbf{x}) = \begin{cases} 1 & \text{at } \mathbf{x} \in (\Omega_s \cup \partial\Omega_s) \\ 0 & \text{at } \mathbf{x} \notin (\Omega_s \cup \partial\Omega_s) \end{cases}.$$

Then, the local weak-forms (13) and (14) are transformed into the following local integral equations (LIEs)

$$\int_{\partial\Omega_s^i} M_\alpha(\mathbf{x}, \tau) d\Gamma - \int_{\Omega_s^i} Q_\alpha(\mathbf{x}, \tau) d\Omega - \int_{\Omega_s^i} I_M \ddot{w}_\alpha(\mathbf{x}, \tau) d\Omega = 0, \quad (16)$$

$$\int_{\partial\Omega_s^i} Q_\alpha(\mathbf{x}, \tau) n_\alpha(\mathbf{x}) d\Gamma - \int_{\Omega_s^i} I_Q \ddot{w}_3(\mathbf{x}, \tau) d\Omega + \int_{\Omega_s^i} q(\mathbf{x}, \tau) d\Omega = 0. \quad (17)$$

In the above local integral equations, the trial functions $w_\alpha(\mathbf{x}, \tau)$ related to rotations, and $w_3(\mathbf{x}, \tau)$ related to transversal displacements, are chosen as the moving least-squares (MLS) approximations over a number of nodes randomly spread within the domain of influence.

4. Numerical Implementation

In general, a meshless method uses a local interpolation to represent the trial function with the values (or the fictitious values) of the unknown variable at some randomly located nodes. The

moving least-squares (MLS) approximation [27] used in the present analysis may be considered as one of such schemes. Let us consider a sub-domain Ω_x of the problem domain Ω in the neighbourhood of a point \mathbf{x} for the definition of the MLS approximation of the trial function around \mathbf{x} (Fig. 3). To approximate the distribution of the generalized displacements (rotations and deflection) in Ω_x over a number of randomly located nodes $\{\mathbf{x}^a\}$, $a = 1, 2, \dots, n$, the MLS approximant $w_i^h(\mathbf{x}, \tau)$ of $w_i(\mathbf{x}, \tau)$ is defined by

$$\bar{\mathbf{w}}^h(\mathbf{x}, s) = \mathbf{p}^T(\mathbf{x}) \bar{\mathbf{a}}(\mathbf{x}, s), \quad \forall \mathbf{x} \in \Omega_x \quad (18)$$

where $\mathbf{w}^h = [w_1^h, w_2^h, w_3^h]^T$, $\mathbf{p}^T(\mathbf{x}) = [p^1(\mathbf{x}), p^2(\mathbf{x}), \dots, p^m(\mathbf{x})]$ is a complete monomial basis of order m , and $\bar{\mathbf{a}}(\mathbf{x}, \tau) = [\mathbf{a}^1(\mathbf{x}, \tau), \mathbf{a}^2(\mathbf{x}, \tau), \dots, \mathbf{a}^m(\mathbf{x}, \tau)]^T$ is composed of vectors $\mathbf{a}^j(\mathbf{x}, \tau) = [a_1^j(\mathbf{x}, \tau), a_2^j(\mathbf{x}, \tau), a_3^j(\mathbf{x}, \tau)]^T$ which are functions of the spatial co-ordinates and the time $\mathbf{x} = [x_1, x_2]^T$.

The coefficient vector $\bar{\mathbf{a}}(\mathbf{x}, \tau)$ is determined by minimizing a weighted discrete L_2 -norm defined as

$$J(\mathbf{x}) = \sum_{a=1}^n \nu^a(\mathbf{x}) [\mathbf{p}^T(\mathbf{x}^a) \bar{\mathbf{a}}(\mathbf{x}, \tau) - \hat{\mathbf{w}}^a(\tau)]^2, \quad (19)$$

where $\nu^a(\mathbf{x}) > 0$ is the weight function associated with the node a and the square power is considered in the sense of scalar product. Recall that n is the number of nodes in Ω_x for which the weight function $\nu^a(\mathbf{x}) > 0$ and $\hat{\mathbf{w}}^a(\tau)$ are the fictitious nodal values, but not the nodal values of the unknown trial function $\mathbf{w}^h(\mathbf{x}, \tau)$, in general. The stationarity of J in eq. (19) with respect to $\bar{\mathbf{a}}(\mathbf{x}, \tau)$ leads to

$$\mathbf{A}(\mathbf{x}) \bar{\mathbf{a}}(\mathbf{x}, \tau) - \mathbf{B}(\mathbf{x}) \hat{\mathbf{w}}(\tau) = 0 \quad (20)$$

where

$$\hat{\mathbf{w}}(\tau) = 0[\hat{w}^1(\tau), \hat{w}^2(\tau), \dots, \hat{w}^n(\tau)]^T,$$

$$\mathbf{A}(\mathbf{x}) = \sum_{a=1}^n \nu^a(\mathbf{x}) \mathbf{p}(\mathbf{x}^a) \mathbf{p}^T(\mathbf{x}^a),$$

$$\mathbf{B}(\mathbf{x}) = [v^1(\mathbf{x}) \mathbf{p}(\mathbf{x}^1), v^2(\mathbf{x}) \mathbf{p}(\mathbf{x}^2), \dots, v^n(\mathbf{x}) \mathbf{p}(\mathbf{x}^n)]. \quad (21)$$

The solution of eq. (20) for and the subsequent substitution into eq. (18) lead to the following expression

$$\mathbf{w}^h(\mathbf{x}, \tau) = \Phi^T(\mathbf{x}) \cdot \hat{\mathbf{w}}(\tau) = \sum_{a=1}^n \phi^a(\mathbf{x}) \hat{\mathbf{w}}^a(\tau) \quad (22)$$

where

$$\Phi^T(\mathbf{x}) = \mathbf{p}^T(\mathbf{x}) \mathbf{A}^{-1}(\mathbf{x}) \mathbf{B}(\mathbf{x}). \quad (23)$$

In eq. (22), $\phi^a(\mathbf{x})$ is usually referred to as the shape function of the MLS approximation corresponding to the nodal point \mathbf{x}^a . From eqs. (21) and (23), it can be seen that $\phi^a(\mathbf{x}) = 0$ when $\nu^a(\mathbf{x}) = 0$. In practical applications, $\nu^a(\mathbf{x})$ is often chosen in such a way that it is non-zero over the support of the nodal point \mathbf{x}^a . The support of the nodal point \mathbf{x}^a is usually taken to be a circle of the radius r^a centred at \mathbf{x}^a (see Fig. 3). The radius r^a is an important parameter of the MLS approximation because it determines the range of the

interaction (coupling) between the degrees of freedom defined at considered nodes.

Usually a 4th-order spline-type weight function is applied [17]

$$\nu^a(\mathbf{x}) = \begin{cases} 1 - 6\left(\frac{d^a}{r^a}\right)^2 + 8\left(\frac{d^a}{r^a}\right)^3 - 3\left(\frac{d^a}{r^a}\right)^4 & 0 \leq d^a \leq r^a \\ 0 & d^a \geq r^a \end{cases} \quad (24)$$

where $d^a = \|\mathbf{x} - \mathbf{x}^a\|$ and r^a is the radius of the circular support domain. With eq. (24), the C^1 -continuity of the weight function is ensured over the entire domain, therefore the continuity condition of the bending moments and the shear forces is satisfied. The size of the support r^a should be large enough to cover a sufficient number of nodes in the domain of definition to ensure the regularity of the matrix \mathbf{A} . The value of n is determined by the number of nodes lying in the support domain with radius r^a .

The partial derivatives of the MLS shape functions are obtained as [28]

$$\phi_{,k}^a = \sum_{j=1}^m [p_{,k}^j (A^{-1}\mathbf{B})^a + p^j (A^{-1}\mathbf{B}_{,k} + A_{,k}^{-1}\mathbf{B})^a] \quad (25)$$

wherein $A_{,k}^{-1} = (A^{-1})_{,k}$ represents the derivative of the inverse of \mathbf{A} with respect to x_k , which is given by

$$A_{,k}^{-1} = -\mathbf{A} A_{,k} \mathbf{A}^{-1}.$$

The directional derivatives of $\mathbf{w}(\mathbf{x}, \tau)$ are approximated in terms of the same nodal values as

$$\mathbf{w}_{,k}(\mathbf{x}, \tau) = \sum_{a=1}^n \hat{\mathbf{w}}^a(\tau) \phi_{,k}^a(\mathbf{x}) \quad (26)$$

Substituting the approximation (26) into the definition of the bending moments (6) and then using $M_{\alpha\beta}(\mathbf{x}, \tau) = M_{\alpha\beta}(\mathbf{x}, \tau) n_{\beta}(\mathbf{x})$, one obtains for $\mathbf{M}(\mathbf{x}, \tau) = [M_1(\mathbf{x}, \tau), M_2(\mathbf{x}, \tau)]^T$

$$\begin{aligned} \mathbf{M}(\mathbf{x}, \tau) &= \mathbf{N}_1 \sum_{a=1}^n \mathbf{B}_1^a(\mathbf{x}) \mathbf{w}^{*a}(\tau) + \mathbf{N}_2 \sum_{a=1}^n \mathbf{B}_2^a(\mathbf{x}) \mathbf{w}^{*a}(\tau) = \\ &= \mathbf{N}_\alpha(\mathbf{x}) \sum_{a=1}^n \mathbf{B}_\alpha^a(\mathbf{x}) \mathbf{w}^{*a}(\tau) \end{aligned} \quad (27)$$

where the vector $\mathbf{w}^{*a}(\tau)$ is defined as a column vector $\mathbf{w}^{*a}(\tau) = [\hat{\mathbf{w}}_1^a(\tau), \hat{\mathbf{w}}_2^a(\tau)]^T$, the matrices $\mathbf{N}_\alpha(\mathbf{x})$ are related to the normal vector $\mathbf{n}(\mathbf{x})$ on $\partial\Omega_s$ by

$$\mathbf{N}_1(\mathbf{x}) = \begin{bmatrix} n_1 & 0 & n_2 \\ 0 & n_2 & n_1 \end{bmatrix} \text{ and } \mathbf{N}_2(\mathbf{x}) = \begin{bmatrix} C_{11} & 0 \\ 0 & C_{22} \end{bmatrix} \begin{bmatrix} n_1 & n_1 \\ n_2 & n_2 \end{bmatrix}$$

and the matrices \mathbf{B}_α^a are represented by the gradients of the shape functions as

$$\mathbf{B}_1^a(\mathbf{x}) = \begin{bmatrix} 2D_{11}\phi_{,1}^a & 0 \\ 0 & 2D_{22}\phi_{,2}^a \\ D_{12}\phi_{,2}^a & D_{12}\phi_{,1}^a \end{bmatrix}, \quad \mathbf{B}_2^a(\mathbf{x}) = \begin{bmatrix} \phi_{,1}^a & 0 \\ 0 & \phi_{,2}^a \end{bmatrix}.$$

The influence of the material properties for composite laminates is incorporated into $C_{\alpha\beta}$ and $D_{\alpha\beta}$ defined in equations (7). Similarly one can obtain the approximation for the shear forces

$$\mathbf{Q}(\mathbf{x}, \tau) = \mathbf{C}(\mathbf{x}) \sum_{a=1}^n [\phi^a(\mathbf{x}) \mathbf{w}^{*a}(\tau) + \mathbf{F}^a(\mathbf{x}) \hat{\mathbf{w}}_3^a(\tau)] \quad (28)$$

where $\mathbf{Q}(\mathbf{x}, \tau) = [Q_1(\mathbf{x}, \tau), Q_2(\mathbf{x}, \tau)]^T$ and

$$\mathbf{C}(\mathbf{x}) = \begin{bmatrix} C_1(\mathbf{x}) & 0 \\ 0 & C_2(\mathbf{x}) \end{bmatrix}, \quad \mathbf{F}^a(\mathbf{x}) = \begin{bmatrix} \phi_{,1}^a \\ \phi_{,2}^a \end{bmatrix}.$$

Then, insertion of the MLS-discretized moment and force fields (27) and (28) into the local integral equations (16) and (17) yields the discretized local integral equations

$$\begin{aligned} &\sum_{a=1}^n \left[\int_{\Gamma_{sw}^i} \mathbf{N}_\alpha(\mathbf{x}) \mathbf{B}_\alpha^a(\mathbf{x}) d\Gamma - \int_{\Omega_s^i} \mathbf{C}(\mathbf{x}) \phi^a(\mathbf{x}) d\Omega \right] \mathbf{w}^{*a}(\tau) - \\ &- \sum_{a=1}^n I_M \hat{\mathbf{w}}_3^{*a}(\tau) \left(\int_{\Omega_s^i} \phi^a(\mathbf{x}) d\Omega \right) - \\ &- \sum_{a=1}^n \hat{\mathbf{w}}_3^a(\tau) \left(\int_{\Omega_s^i} \mathbf{C}(\mathbf{x}) \mathbf{F}^a(\mathbf{x}) d\Omega \right) = - \int_{\Gamma_{sw}^i} \tilde{\mathbf{N}}(\mathbf{x}, \tau) d\Gamma, \end{aligned} \quad (29)$$

$$\begin{aligned} &\sum_{a=1}^n \left(\int_{\partial\Omega_s^i} \mathbf{C}_n(\mathbf{x}) \phi^a(\mathbf{x}) d\Gamma \right) \mathbf{w}^{*a}(\tau) + \\ &+ \sum_{a=1}^n \hat{\mathbf{w}}_3^a(\tau) \left(\int_{\partial\Omega_s^i} \mathbf{C}_n(\mathbf{x}) \mathbf{F}^a(\mathbf{x}) d\Gamma \right) = \\ &= I_Q \sum_{a=1}^n \hat{\mathbf{w}}_3^a(\tau) \left(\int_{\Omega_s^i} \phi^a(\mathbf{x}) d\Omega \right) = - \int_{\Omega_s^i} q(\mathbf{x}, \tau) d\Omega, \end{aligned} \quad (30)$$

in which $\tilde{\mathbf{M}}(\mathbf{x}, \tau)$ represent the prescribed bending moments on Γ_{sw}^i and

$$\mathbf{C}_n(\mathbf{x}) = (n_1, n_2) \begin{pmatrix} C_1 & 0 \\ 0 & C_2 \end{pmatrix} = (C_1 n_1, C_2 n_2).$$

Equations (29) and (30) are considered on the subdomains adjacent to the interior nodes \mathbf{x}^i as well as to the boundary nodes on Γ_{sw}^i . For the source point \mathbf{x}^i located on the global boundary Γ the boundary of the subdomain $\partial\Omega_s^i$ is decomposed into L_s^i and L_{sw}^i (part of the global boundary with prescribed bending moment) according to Fig. 2.

It should be noted here that there are neither Lagrange multipliers nor penalty parameters introduced into the local weak-forms (12) because the essential boundary conditions on Γ_{sw}^i (part of the global boundary with prescribed rotations or displacements) can be imposed directly, using the interpolation approximation (22)

$$\sum_{a=1}^n \phi^a(\mathbf{x}^i) \hat{\mathbf{w}}^a(\tau) = \tilde{\mathbf{w}}(\mathbf{x}^i, \tau) \text{ for } \mathbf{x}^i \in \Gamma_{sw}^i, \quad (31)$$

where $\tilde{\mathbf{w}}(\mathbf{x}^i, \tau)$ is the generalized displacement vector prescribed on the boundary Γ_{sw}^i . For a clamped plate all three vector components (rotations and deflection) are vanishing on the fixed edge, and eq. (31) is used at all the boundary nodes in such a case. However, for a simply supported plate only the third component of the displacement vector (deflection) is prescribed, while the rotations are unknown. Then, the entire equation (29) and the third component of eq. (31) are applied to the nodes lying on the global boundary. On those parts of the global boundary where no displacement boundary conditions are prescribed both local integral equations (29) and (30) are applied.

Collecting the discretized local boundary-domain integral equations together with the discretized boundary conditions for the generalized displacements, one obtains a complete system of ordinary differential equations and it can be rearranged in such a way that all known quantities are on the r.h.s. Thus, in matrix form the system becomes

$$\mathbf{M} \ddot{\mathbf{U}} + \mathbf{K} \mathbf{U} = \mathbf{F} \quad (32)$$

where \mathbf{M} is the mass matrix, \mathbf{K} is the stiffness matrix and \mathbf{F} is the external load vector. Recall that the system matrix has a block structure. There are many time integration procedures for the solution of this system of ordinary differential equations. In the present work, the Houbolt method is applied [29]. In the Houbolt finite-difference scheme the value of the time-step has to be appropriately selected with respect to material parameters (elastic wave velocities) and time dependence of the boundary conditions.

5. Numerical Examples

In this section, numerical results are presented for two laminate plates under an impact load with Heaviside time variation. Clamped and simply supported square plates are analysed. In order to test the accuracy, the numerical results obtained by the present method are compared with the results provided by the FEM-ANSYS code using a very fine mesh. In numerical calculations, deviations of the results for plates with a laminate structure from those corresponding to a homogeneous plate are investigated. The mass density is assumed to be uniform m within the whole bulk of the plate.

Example 1: Clamped square plate

In this example the clamped orthotropic thick square plate under an impact load with Heaviside time variation is analyzed. The clamped square plate has side-length $a = 0.254m$ and the plate thickness is $h/a = 0.05$. Homogeneous material properties are considered firstly to test the accuracy of the present computational method. The following material parameters are used in our numerical analysis: Young's moduli $E_2 = 0.6895 \cdot 10^{10} \text{ N/m}^2$ and $E_1 = 2E_2$, Poisson's ratios $\nu_{21} = 0.15$ and $\nu_{12} = 0.3$ and mass density $\rho = 5.0 \times 10^3 \text{ kgm}^{-3}$. The used shear moduli correspond to Young's modulus E_2 , namely, $G_{12} = G_{13} = G_{23} = E_2/[2(1 + \nu_{12})]$.

For the numerical modelling we used again 441 nodes with a regular distribution (Fig. 3). Numerical calculations are carried out for a time-step $\Delta\tau = 0.357 \cdot 10^{-4} \text{ s}$. The MLPG results are compared with those obtained by FEM-ANSYS computer code, where 900 quadrilateral eight-node shell elements with 1000 time increments were used. The static central deflection is $w_3^{stat}(0) = 8.842 \cdot 10^{-3} \text{ m}$ for the considered load $q_0 = 2.07 \times 10^6 \text{ Nm}^{-2}$. The static bending moment is $M_{11}^{stat}(0) = 3064 \text{ Nm}$. The time is normalized by $\tau_0 = a^2/4\sqrt{\rho h/D} = 0.3574 \cdot 10^{-2} \text{ s}$, where $D = Eh^3/[12(1 - \nu^2)]$ is bending rigidity of plate. A good agreement of the present results for the deflection and the bending moment at the plate center and the FEM results is observed.

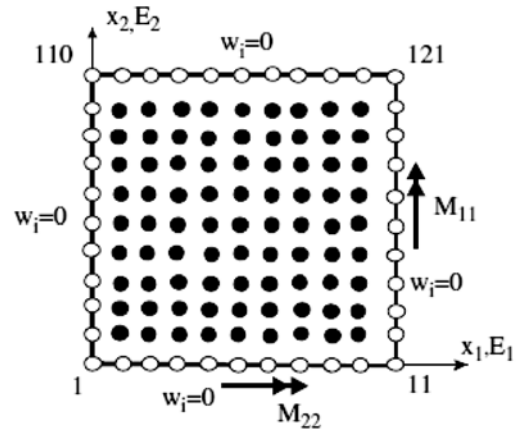


Fig. 3. Node distribution for numerical analyses of a clamped square plate.

The peaks of the moment amplitudes are shifted to shorter time instants for the orthotropic plate with a larger flexural rigidity. Since the mass density is the same for both isotropic and orthotropic plates, the wave velocity is higher for the orthotropic plate with higher Young's modulus. The amplification of the bending moments due to the dynamic impact load for both isotropic and orthotropic plates are almost the same if they are normalized with respect to the corresponding static values. The static bending moment for the orthotropic plate is slightly higher at the center of the plate [30]. Time variation of the deflection at the center of a clamped square plate subjected to a suddenly applied load Fig. 4. Then, the peak value for the orthotropic plate under an impact load has to be higher since that value is normalized by corresponding static value at the center of the isotropic plate.

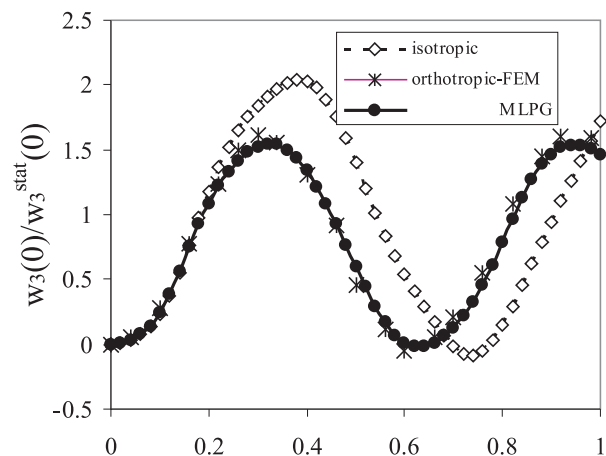


Fig. 4 Time variation of the deflection at the center a clamped square plate

Example 2: Simply supported three-ply orthotropic square plate

A simply supported three-ply orthotropic square plate under an impact load with Heaviside time variation is analyzed. The used geometrical and material parameters are the same as for the previous clamped plate. The total plate thickness is $h = 0.0127m$, which is equal to the thickness of the homogeneous plate in previous examples. The bottom and top layers have the same thickness $h_1 = h_3 = h/4$. Young's moduli for both bottom and top layers are the same and they are 5 times larger than the ones corresponding to the homogeneous orthotropic plate. The second mid-layer has the thickness $h_2 = h/2$ and the same material properties as the homogeneous plate analyzed in previous example. For the numerical modelling we used again 441 nodes with a regular distribution. A uniformly distributed load $q_0 = 300 \text{ psi} = 2.07 \times 10^6 \text{ Nm}^{-2}$ is considered here.

Numerical calculations are carried out for a time-step $\Delta t = 0.357 \cdot 10^{-4} \text{ s}$. Time variation of the deflection at the center of a simply supported plates subjected to a suddenly applied load is given in Fig. 5.

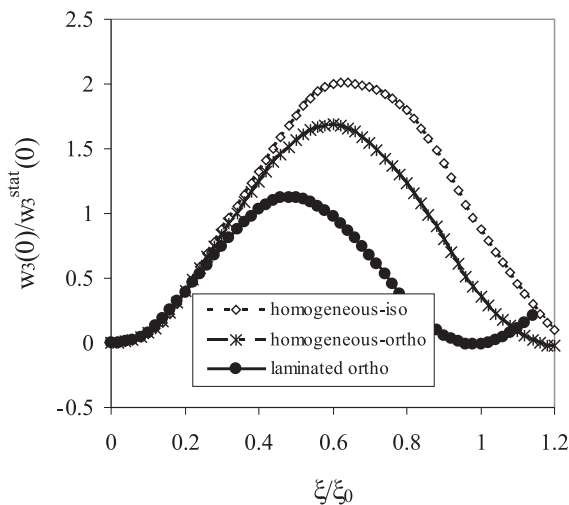


Fig. 5 Time variation of the deflection at the center of a simply supported plates subjected to a suddenly applied load

The peaks of the deflection and bending moment amplitudes are shifted to shorter time instants for the orthotropic homogeneous and laminated plates due to larger Young's moduli. They are largest for the laminated orthotropic plate. Since the mass density is the same in all plates, the elastic wave velocity is largest for the laminated plate. The maximum reduction of the deflection is achieved for the laminate plate, where the flexural rigidity is the largest.

6. Conclusion

A meshless local Petrov-Galerkin method is applied to laminate plates under mechanical loadings. The present computational method has no restriction on the number of the laminae and their material properties. The laminate plate bending problem is described by the Reissner-Mindlin theory. The Reissner-Mindlin theory reduces the original three-dimensional (3-D) thick plate problem to a 2-D problem. The weak-form on small subdomains with a Heaviside step function as the test functions is applied to derive local integral equations. After performing the spatial MLS approximation, a system of ordinary differential equations for certain nodal unknowns is obtained. Then, the system of the ordinary differential equations is solved by the Houbolt finite-difference scheme as a time-stepping method.

The proposed method is a truly meshless method, which requires neither domain elements nor background cells in either the interpolation or the integration. It is demonstrated numerically that the quality of the results obtained by the proposed MLPG method is very good. The degree of the agreement of our numerical results with those obtained by the FEM-ANSYS computer code ranges from good to excellent. Since in our illustrative examples only simple problems are analysed, only a regular node distribution has been used. However, a random location of nodes should be considered for further progress of the method.

Acknowledgments

The authors gratefully acknowledge the support by the Slovak Grant Agency VEGA 1/1226/12 and Slovak Science and Technology Assistance Agency registered under number APVV-0169-07.

References

- [1] ZHOU, J. X., WANG, X.M, ZHANG, Y.Q., ZHANG, L.: On the Enhancement of Computation and Exploration of Discretization Approaches for Meshless Shape Design Sensitivity Analysis. *Struc. Multidisc. Optim*, 31, 2006, pp. 96–104.
- [2] SAGA, M., VASKO, M.: Stress Sensitivity Analysis of the Beam and Shell Finite Elements. *Communications - Scientific Letters of the University of Zilina*, 11, 2, 2009, pp. 5–12.
- [3] SAGA, M., KOPAS, P., VASKO, M.: Some Computational Aspects of Vehicle Shell Frames Optimization Subjected to Fatigue Life. *Communications - Scientific Letters of the University of Zilina*, 12, 4, 2010, pp. 73–79.
- [4] WANG, J., HUANG, M.: Boundary Element Method for Orthotropic Thick Plates. *Acta Mechanica Sinica*, 7, 1991, pp. 258–266.
- [5] WANG, J.; SCHWEIZERHOF, K.: Study on Free Vibration of Moderately Thick Orthotropic Laminated Shallow Shells by Boundary-domain Elements. *Applied Mathematical Modelling*, 20, 1996, pp. 579–584.

- [6] REDDY, J. N.: *Mechanics of Laminated Composite Plates: Theory and Analysis*. CRC Press, Boca Raton, 1997.
- [7] QIAN, L. F., BATRA, R. C., CHEN, L. M.: Analysis of Cylindrical Bending Thermoelastic Deformations of Functionally Graded Plates by a Meshless Local Petrov-Galerkin Method. *Computational Mechanics*, 33, 2004, 263-273.
- [8] BESKOS, D. E.: Static and Dynamic Analysis of Shells. In *Boundary Element Analysis of Plates and Shells*. Springer-Verlag : Berlin, 1991, pp. 93-140.
- [9] PROVIDAKIS, C. P., BESKOS, D. E.: Dynamic Analysis of Plates by boundary Elements. *Applied Mechanics Reviews ASME*, 52, 1999, pp. 213-236.
- [10] VAN DER WEEN, F.: Application of the Boundary Integral Equation Method to Reissner's Plate Model. *Intern. J. for Numerical Methods in Engineering*, 18, 1982, pp. 1-10.
- [11] ANTES, H.: Static and Dynamic Analysis of Reissner-Mindlin Plates. In: *Boundary Element Analysis of Plates and Shells* (Beskos DE ed.). Springer-Verlag : Berlin, 1991, pp. 312-340.
- [12] WEN, P. H., ALIABADI, M. H.: Boundary Element Frequency Domain Formulation for Dynamic Analysis of Mindlin Plates. In: *Boundary Element Techniques* (Aliabadi MH, Selvadurai APS, Tan CL, eds.), 2005, pp. 35-42.
- [13] WANG, J., HUANG, M.: Boundary Element Method for Orthotropic Thick Plates. *Acta Mechanica Sinica*, 7, 1991, pp. 258-266.
- [14] KOMPIS, V., DEKYS, V.: Analysis of Local Stress and Displacement Fields in Contact of 3D Bodies with Curved Surfaces, *Mechanical Eng. J.*, 54, pp. 5-6, 2003.
- [15] ZMINDAK, M., RIECKY, D., SOUKUP, J.: Failure of Composites with Short Fibers. *Communications - Scientific Letters of the University of Zilina*, 4/2010.
- [16] BELYTSCHKO, T., KROGAUZ, Y., ORGAN, D., FLEMING, M., KRYSL, P.: Meshless Methods; an Overview and Recent Developments. *Comp. Meth. Appl. Mech. Engn.*, 1996, 139, pp. 3-47.
- [17] ATLURI, S. N.: *The Meshless Method*, (MLPG) for Domain & BIE Discretizations, Tech Science Press, 2004.
- [18] KRYSL, P.; BELYTSCHKO, T.: Analysis of Thin Plates by the Element-Free Galerkin Method. *Computational Mechanics*, 17, 1996, pp. 26-35.
- [19] KRYSL, P.; BELYTSCHKO, T.: Analysis of Thin Shells by the Element-Free Galerkin Method. *Int. J. Solids and Structures*, 33, 1996, pp. 3057-3080.
- [20] NOGUCHI, H., KAWASHIMA, T., MIYAMURA, T.: Element Free Analyses of Shell and Spatial Structures, *Int. J. for Numerical Methods in Engineering*, 47, 2000, pp. 1215-1240.
- [21] LONG, S.Y., ATLURI, S.N., A: Meshless Local Petrov Galerkin Method for Solving the Bending Problem of a Thin Plate. *Computer Modeling in Engineering & Sciences*, 3, 2002, pp. 11-51.
- [22] SLADEK, J., SLADEK, V., MANG, H.A.: Meshless Formulations for Simply Supported and Clamped Plate Problems. *Int. J. for Numerical Methods in Engineering*, 55, 2002, pp. 359-375.
- [23] SLADEK, J., SLADEK, V., MANG, H.A.: Meshless LBIE Formulations for Simply Supported and Clamped Plates under Dynamic Load, *Computers & Structures*, 81, 2003, pp. 1643-1651.
- [24] JARAK, T.; SORIC, J.; HOSTER, J.: Analysis of Shell Deformation Responses by the Meshless Local Petrov-Galerkin (MLPG) approach. *CMES: Computer Modeling in Engineering & Sciences*, 18, 3, 2007, pp. 235-246.
- [25] REDDY, J.N., MIRAVETE, A.: *Practical Analysis of Composite Laminates*. CRC Press, 1995.
- [26] LEKHNITSKII, S.G.: *Theory of Elasticity of an Anisotropic Elastic Body*. Holden Day, San Francisco, also Mir Publishers, Moscow, 1981.
- [27] LANCASTER, P., SALKAUSKAS, T.: Surfaces Generated by Moving Least Square Methods. *Math. Comput.*, 37, 1981, pp. 141-158.
- [28] SLADEK, J., SLADEK, V., MANG, H.A.: Meshless Formulations for Simply Supported and Clamped Plate Problems. *Int. J. Num. Meth. Engn.*, 55, 2002, pp. 359-375.
- [29] BATHE, K.J.: *Finite Element Procedures*. Prentice - Hall, Inc., 1996.
- [30] RIECKY, D., ZMINDAK, M., NOVAK, P.: *Transient Dynamic Analysis of Rectangular Orthotropic Composite Plates*. In: Proc. of 9th European Conference of Young Research and Scientific Workers, TRANSCOM 2011, Zilina, 2011.

Milan Saga – Martin Dudinsky – Peter Pechac *

OPTIMIZATION OF THIN SHELL STRUCTURES USING FSD ALGORITHMS

The paper presents a theoretical and numerical study of the efficiency of the fully stress design (FSD) algorithm in the case of thin shell finite elements. Relation between membrane forces, bending moments and the element thickness is analysed by means of numerical tests. Subsequent numerical testing and a new iterative algorithm to providing the rapid convergence of the optimizing process is proposed.

Keywords: stress analysis, thin shell finite element, fully stress design

1. Introduction

Structural optimization and development of new optimizing methods have been topical problems for several decades. At the present time the current issues are problems which have global character such as ecology, energetic sources, mineral and natural wealth, effectiveness of production and so on. Optimization process is used in all fields participating in development or innovation of technical devices and solutions. At the present time optimization and innovation are inseparable parts of every existing or developed engineering work analysed by means of computational technique [1].

Expansion of computational technique allowed putting qualitatively new approaches in designing machines and appliances into practice. The problem of proper designing and constructing of machines gets new dimensions and wide scope for solving other unsolved problems by establishing computers and consequent creating and developing corresponding software. An optimized design is comprehended as a technically realizable design of structure which is the best from all possible designs for a given goal [2].

Optimization of mechanical systems combines numerical mathematics and engineering mechanics. It is used in applications in civil engineering, mechanical engineering, automotive and ship-building industry, and so on. It made the biggest progress in last thirty years thanks to utilizing very fast numerical computers and computer graphics. When choosing cost, weight of structure or maximum power at a limited cost as a design criterion, the importance of optimization is evident.

The main task for a designer is still to propose dimensions of the structure properly with respect to its minimal weight, proper geometry, or some dynamical properties. The main goal is to spare material and find the best solution from a constructional point of

view as well as the view of utilization of material and technologies [1].

The effort to create an optimal structure is not new, of course, but using optimization approaches in practical work of a designer can be achieved only by utilizing numerical methods and a powerful computational technique. Numerical methods are forcing out analytical methods which are time-consuming and improper for a lot of practical problems [3, 4].

Today we expect that designed objects will be optimally balanced in term of entire life cycle, i.e. projecting, manufacturing, running, maintaining and liquidating. The mentioned process relates mainly with economic aspects of each stage. Achieving this goal is very difficult, because a designer is usually met with contradictory demands related to individual stages of the mentioned life cycle of a designed object [4].

First formulations of optimization problems in the form of mathematical programming have been occurring approximately since 1960. One of the pioneers who significantly influenced the development of the optimal designing of constructions of machines and their components, was undoubtedly Schmit. He linked optimization methods with a new and progressive computational method at that time – the finite element method as one of the first. At that time, the weight of a monitored object or some strength condition was the objective function. Optimization process was gradually improving by adding other limiting conditions. In the second half of the last century other works of similar nature, which extended options in the field of optimal designing of parameters of machines and their components into automated approaches occurred. We can not omit works of Kirch, Morrow, or Gallagher. Plenty of effective approaches were designed. They were based not only on a purely mathematical comprehension of optimization problem, but also a little bit non-traditional or unaccustomed appro-

* Milan Saga, Martin Dudinsky, Peter Pechac

Department of Applied Mechanics, Faculty of Mechanical Engineering, University of Zilina, Slovakia, E-mail: milan.saga@fstroj.uniza.sk

aches which play an important role in solving various technical problems were utilized. These approaches use some of the basic principles of mechanics. For example, the method which is known as the fully stress design (FSD), originated from the idea of independence of axial forces in statically determinate truss structures. Its application is useful mainly thanks to its effectiveness. However, it is limited only to problems of strength dimensioning and it turned out to be a certain disadvantage in creating universal program systems. In this article theory of FSD will be described and applied specially for thin shell structures in spite of its lower universality [2, 5].

2. Stress Calculation of thin Shellfinite Element

We will focus on well-known shell finite elements (Kirchhoff's or Mindlin's formulation) [1, 6, 7, 8], mainly on the stress calculation. The stiffness parameters depend on material constants and element geometry, mainly on its thickness. The stress calculation process is based on the expression of the j -th element membrane forces and bending moments (without shear forces) [6, 9], i.e.

$$\begin{aligned} [F_{xx} \ F_{yy} \ F_{xy}]_j^T &= \mathbf{F}_m^j = \int_S \mathbf{E}_m^j \cdot \boldsymbol{\varepsilon}_m^j dS_j = \\ &= \mathbf{E}_m^j \cdot \int_S \mathbf{B}_m^j dS_j \cdot \mathbf{u}_L^j = t_j \cdot \mathbf{D}_j \cdot \mathbf{I}_b^j \cdot \mathbf{u}_L^j \end{aligned} \quad (1)$$

and

$$\begin{aligned} [M_{xx} \ M_{yy} \ M_{xy}]_j^T &= \mathbf{M}_b^j = \int_S \mathbf{E}_b^j \cdot \boldsymbol{\varepsilon}_b^j dS_j = \\ &= \mathbf{E}_b^j \cdot \int_S \mathbf{B}_b^j \cdot dS_j \cdot \mathbf{u}_L^j = \frac{t_j^3}{12} \cdot \mathbf{D}_j \cdot \mathbf{I}_b^j \cdot \mathbf{u}_L^j \end{aligned} \quad (2)$$

The auxiliary matrices \mathbf{I}_m and \mathbf{I}_b can be calculated only using the numerical approach. Further details about \mathbf{E}_m , \mathbf{E}_b , \mathbf{D} , \mathbf{B}_m , \mathbf{B}_b , \mathbf{u}_L and t are presented in [9]. The extreme stress values can be expected at the top or at the bottom surface. Generally, it means

$$\begin{aligned} [\boldsymbol{\sigma}_{mb}]_{top}^j &= \begin{Bmatrix} \sigma_{xx} \\ \sigma_{yy} \\ \sigma_{xy} \end{Bmatrix}^j = \begin{bmatrix} 1/t_j & 0 & 0 & 6/t_j^2 & 0 & 0 \\ 0 & 1/t_j & 0 & 0 & 6/t_j^2 & 0 \\ 0 & 0 & 1/t_j & 0 & 0 & 6/t_j^2 \end{bmatrix} \cdot \\ &\begin{Bmatrix} F_{xx} \\ F_{yy} \\ F_{xy} \\ M_{xx} \\ M_{yy} \\ M_{xy} \end{Bmatrix} = [\mathbf{A}]_{top}^j \cdot \mathbf{f}^j \end{aligned} \quad (3)$$

for top element surface and

$$\begin{aligned} [\boldsymbol{\sigma}_{mb}]_{bot}^j &= \begin{Bmatrix} \sigma_{xx} \\ \sigma_{yy} \\ \sigma_{xy} \end{Bmatrix}^j = \begin{bmatrix} 1/t_j & 0 & 0 & -6/t_j^2 & 0 & 0 \\ 0 & 1/t_j & 0 & 0 & -6/t_j^2 & 0 \\ 0 & 0 & 1/t_j & 0 & 0 & -6/t_j^2 \end{bmatrix} \cdot \\ &\begin{Bmatrix} F_{xx} \\ F_{yy} \\ F_{xy} \\ M_{xx} \\ M_{yy} \\ M_{xy} \end{Bmatrix} = [\mathbf{A}]_{bot}^j \cdot \mathbf{f}^j \end{aligned} \quad (4)$$

for the bottom element surface. Generally, the “top” or “bottom” von Mises stresses may be calculated from relations [10]

$$\begin{aligned} \sigma_{eq|top}^2 &= [\boldsymbol{\sigma}_{mb}]_{top}^T \cdot \mathbf{T}_{mb} \cdot [\boldsymbol{\sigma}_{mb}]_{top} = \mathbf{f}^T \cdot [\mathbf{A}]_{top}^T \cdot \\ &\cdot \mathbf{T}_{mb} \cdot [\mathbf{A}]_{top} \cdot \mathbf{f} = \mathbf{f}^T \cdot \mathbf{T}_{top} \cdot \mathbf{f} \end{aligned} \quad (5)$$

or

$$\begin{aligned} \sigma_{eq|bot}^2 &= [\boldsymbol{\sigma}_{mb}]_{bot}^T \cdot \mathbf{T}_{mb} \cdot [\boldsymbol{\sigma}_{mb}]_{bot} = \mathbf{f}^T \cdot [\mathbf{A}]_{bot}^T \cdot \\ &\cdot \mathbf{T}_{mb} \cdot [\mathbf{A}]_{bot} \cdot \mathbf{f} = \mathbf{f}^T \cdot \mathbf{T}_{bot} \cdot \mathbf{f} \end{aligned} \quad (6)$$

where

$$\mathbf{T}_{mb} = \begin{bmatrix} 1 & -0.5 & 0 \\ -0.5 & 1 & 0 \\ 0 & 0 & 3 \end{bmatrix}, \quad (7)$$

$$\mathbf{T}_{top} = \begin{bmatrix} 1/t^2 & -1/2t^2 & 0 & 6/t^3 & -3/t^3 & 0 \\ -1/2t^2 & 1/t^2 & 0 & -3/t^3 & 6/t^3 & 0 \\ 0 & 0 & 3/t^2 & 0 & 0 & 18/t^3 \\ 6/t^3 & -3/t^3 & 0 & 36/t^4 & -18/t^4 & 0 \\ -3/t^3 & 6/t^3 & 0 & -18/t^4 & 36/t^4 & 0 \\ 0 & 0 & 18/t^3 & 0 & 0 & 108/t^4 \end{bmatrix} \quad (8)$$

and

$$\mathbf{T}_{bot} = \begin{bmatrix} 1/t^2 & -1/2t^2 & 0 & 6/t^3 & 3/t^3 & 0 \\ -1/2t^2 & 1/t^2 & 0 & 3/t^3 & -6/t^3 & 0 \\ 0 & 0 & 3/t^2 & 0 & 0 & -18/t^3 \\ -6/t^3 & 3/t^3 & 0 & 36/t^4 & -18/t^4 & 0 \\ 3/t^3 & -6/t^3 & 0 & -18/t^4 & 36/t^4 & 0 \\ 0 & 0 & -18/t^3 & 0 & 0 & 108/t^4 \end{bmatrix} \quad (9)$$

3. Fully Stress Design (FSD) Theory

We will apply the FSD on a thin shell finite element. The thickness of element t_j will be considered to be a design variable and the iterative relation will be given by [1, 2]

$$t_i^{(k+1)} = \frac{\sigma_{ieq}^{(k)}}{\sigma_L} \cdot t_i^{(k)} \quad (10)$$

where σ_{ieq} is von Mises equivalent stress for the shell element. It is convenient to use, for example, the procedure based on a discrete distribution of interval of admissible values of design variable (e.g. interval partition method) and subsequent evaluation of σ_{ieq} for each t_i . So, then the nearest smaller value of calculated equivalent stress with respect to σ_L will determine the new value of t_i .

The geometric interpretation of the method is shown in Fig. 1. Starting from the similarity of triangles OAB and OCD we will get

$$\frac{\sigma_{ieq}^{(k)}}{\left(\frac{1}{t_i}\right)^{(k)}} = \frac{\sigma_L}{\left(\frac{1}{t_i}\right)^{(k+1)}} \quad (11)$$

From this equation we obtain the well-known iterative relation (10). The mentioned geometric interpretation shows that the new estimation $t_i^{(k+1)}$ is approximated from points $[0,0]$ and

$[(1/t_i)^{(k)}, \sigma_L]$. From the numerical mathematical point of view we are speaking about Regula Falsi method (method of chords-secants).

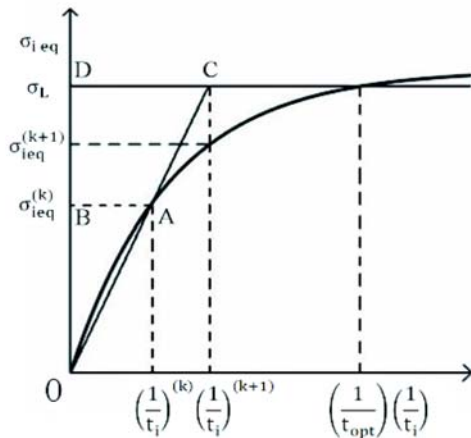


Fig. 1 Geometric interpretation of "classic" FSD

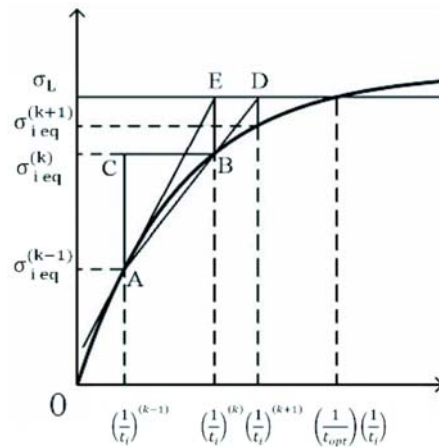


Fig. 2 Geometric interpretation of "new" FSD

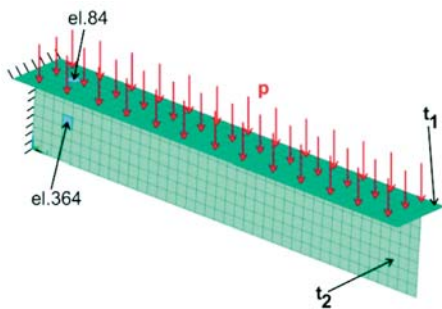


Fig. 3 One-sided fixed testing beam
 $p = 0.05 \text{ MPa}$

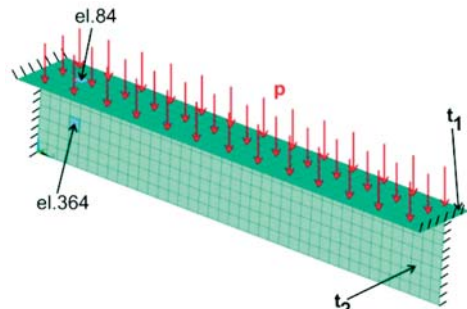


Fig. 4 Two-sided fixed testing beam
 $p = 0.05 \text{ MPa}$

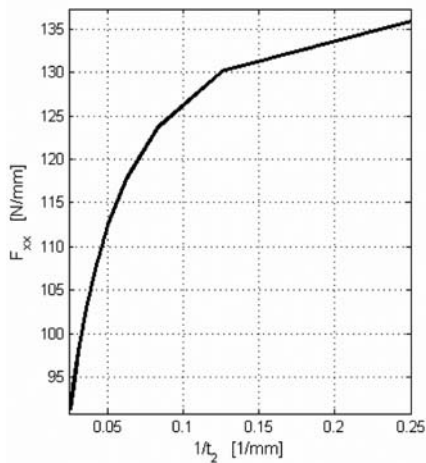


Fig. 5 Relation $F_{xx} - t_2$ for element 84,
for $t_1 = 20 \text{ mm}$ - one-sided fixed beam

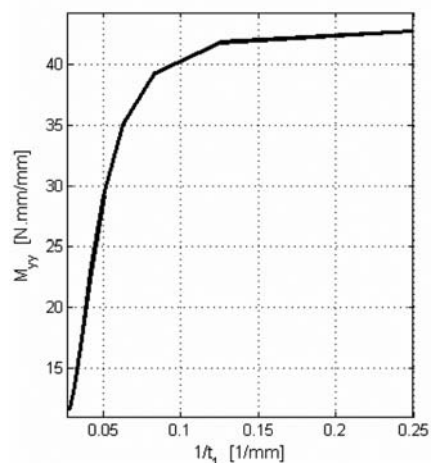


Fig. 6 Relation $M_{yy} - t_1$ for element 84,
 $t_2 = 20 \text{ mm}$ - two-sided fixed beam

On the basis of experiences with classical relation (10), the authors proposed two new computational algorithms. The first one arises from the idea of approximation of new solution from the previous two solutions which leads to the method which is very similar to Newton's tangent method. Geometric interpretation of the method is shown in Fig. 2. Starting from the similarity of triangles ABC and BDE we will get

$$\frac{\sigma_{ieq}^{(k)} - \sigma_{ieq}^{(k-1)}}{\left(\frac{1}{t_i}\right)^{(k)} - \left(\frac{1}{t_i}\right)^{(k-1)}} = \frac{\sigma_L - \sigma_{ieq}^{(k)}}{\left(\frac{1}{t_i}\right)^{(k+1)} - \left(\frac{1}{t_i}\right)^{(k)}} \quad (12)$$

and after modification we obtain the following iterative relation

$$\left(\frac{1}{t_i}\right)^{(k+1)} = \left(\frac{1}{t_i}\right)^{(k)} + \frac{\sigma_L - \sigma_{ieq}^{(k)}}{\sigma_{ieq}^{(k)} - \sigma_{ieq}^{(k-1)}} \left[\left(\frac{1}{t_i}\right)^{(k)} - \left(\frac{1}{t_i}\right)^{(k-1)} \right] \quad (13)$$

New estimation $(1/t_i)^{(k+1)}$ results from the approximation of points $[(1/t_i)^{(k-1)}, \sigma_{ieq}^{(k-1)}]$ and $[(1/t_i)^{(k)}, \sigma_{ieq}^{(k)}]$. The introduced computational procedure is applicable also for truss, beam and shell finite elements.

The second proposed algorithm is suitable especially for shell finite elements.

It arises from the numerical study of effect of element thickness change on internal forces and moments [1]. The numerical analyses (tests) series was realized and it clearly proved the propriety of approximation of internal forces (moments). Two examples were tested (Figs. 3, 4). The dependence of force (moment) vs. element thickness is illustrated in Figs. (5, 6).

The numerical tests showed that the assumption of constant internal forces and moments per unit length $F_{xx}, F_{yy}, F_{xy}, M_{xx}, M_{yy}, M_{xy}$ in thin shells can cause troubles with convergence of solution and algorithms efficiency. This problem can be eliminated by the linear approximation of dependence between the mentioned internal forces per unit length and inverse value of element thickness t_i (more details in e.g. [1] and Fig. 7). Next, we will assume that for $t_i \rightarrow \infty$ expression $(1/t_i) \rightarrow 0$ and an internal force (moment) per unit length $T \rightarrow 0$. So, then the final approximation relation will be given by

$$\mathbf{T}_{approx}^{(k+1)} = \frac{t^2}{t^{(k+1)}} \cdot \mathbf{T}^k \quad \text{or} \quad \mathbf{f}_{approx}^{(k+1)} = \frac{t^k}{t^{(k+1)}} \cdot \mathbf{f}^k, \quad (14)$$

where k is the number of iteration step, in which we find a new value of $t^{(k+1)}$ from discrete design variables interval, for which we will predict internal force quantities per unit length $\mathbf{f}_{approx}^{(k+1)} = [F_{xx}, F_{yy}, F_{xy}, M_{xx}, M_{yy}, M_{xy}]^T$ and von Mises stress σ_{eq} . Vector \mathbf{f}^k is the actual vector of internal forces and moments determined from FEM analysis in k -th iteration step, t^k is the value of design variable, for which FEM analysis in k -th iteration step was performed. Using (5) and (6) we can calculate the approximated value of equivalent stress in $(k+1)$ -th iteration step as follows

$$\left(\sigma_{eq}^2\right)_{approx}^{(k+1)} = \left(\mathbf{f}_{approx}^{(k+1)}\right) \cdot \mathbf{T}_{top}^{(k+1)} \cdot \mathbf{f}_{approx}^{(k+1)} = \left(\mathbf{f}^k\right)^T \cdot \frac{t^k}{t^{(k+1)}} \cdot \mathbf{T}_{top}^{(k+1)} \cdot \frac{t^k}{t^{(k+1)}} \cdot \mathbf{f}^k \quad (15)$$

or

$$\left(\sigma_{eq}^2\right)_{approx}^{(k+1)} = \left(\mathbf{f}_{approx}^{(k+1)}\right) \cdot \mathbf{T}_{bot}^{(k+1)} \cdot \mathbf{f}_{approx}^{(k+1)} = \left(\mathbf{f}^k\right)^T \cdot \frac{t^k}{t^{(k+1)}} \cdot \mathbf{T}_{bot}^{(k+1)} \cdot \frac{t^k}{t^{(k+1)}} \cdot \mathbf{f}^k \quad (16)$$

The mentioned approximation can decrease the number of iteration steps.

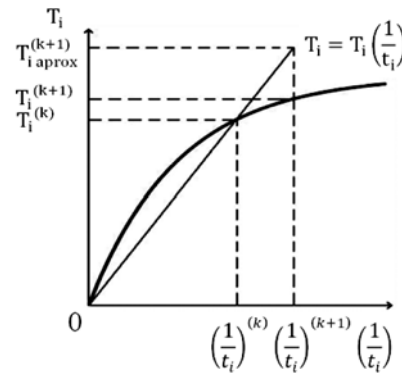


Fig. 7 Principle of the linear approximation of $T(1/t)$

4. Comparison Study of the Proposed Algorithms

The presented computational algorithms were tested and compared on a cranked beam (Fig. 8). Four-node thin shell isoparametric finite elements were used for this testing mechanical problem. The number of elements was 5462 and number of nodes was 5739. The material parameters used: Young's modulus $E = 2.1 \cdot 10^5$ MPa and Poisson's ratio $\nu = 0.3$. The boundary conditions were defined as follows

- forces => pressure $p = 0.05$ MPa (Fig. 8, magenta part),
- displacements => zero displacement on marked areas (Fig. 8, green part).

Three optimizing variables were selected for the process of optimization - thicknesses of flanges and web (See Fig. 9 - blue, green and red parts). The maximum design stress considered $\sigma_L = 120$ MPa. Vector $t_{start} = [40, 40, 40]$ mm was suggested as the start point and discrete design variables were chosen from interval (8, 40) mm with increment of 1 mm. The optimizing process was terminated when the following convergence conditions were fulfilled

- stress convergence condition

$$\left| \frac{\sigma_L - \sigma_i}{\sigma_L} \right| \leq 0.2; \quad \sigma_L - \sigma_i > 0,$$

- design variable convergence condition

$$\frac{t_i^{(k)} - t_i^{(k+1)}}{t_i^{(k)}} \leq 0.05; \quad \sigma_L - \sigma_i > 0.$$

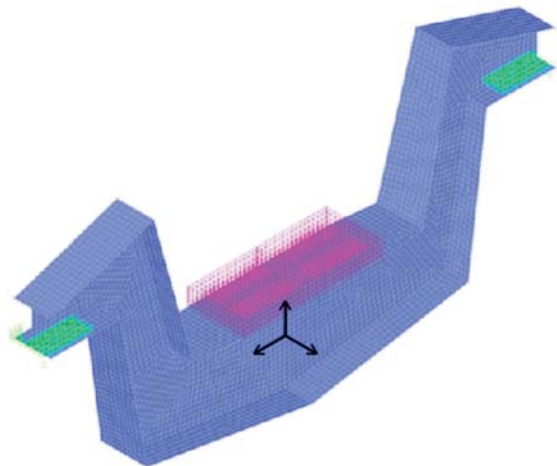


Fig. 8 Force and displacement boundary conditions

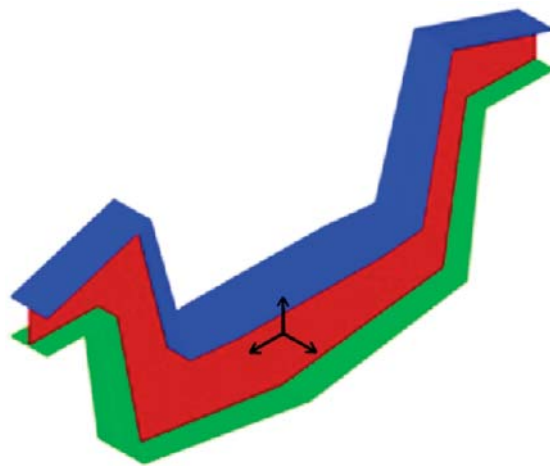


Fig. 9 Optimizing groups identification
 red - 1st design variable
 green - 2nd design variable
 blue - 3rd design variable

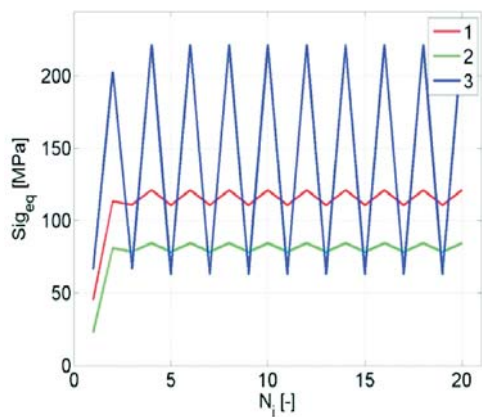


Fig. 10 History of stress convergence for 1st algorithm

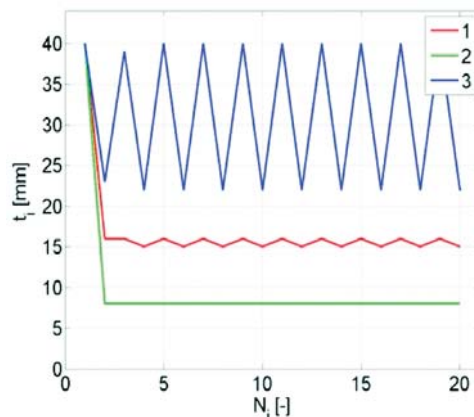


Fig. 11 History of thickness convergence for 1st algorithm

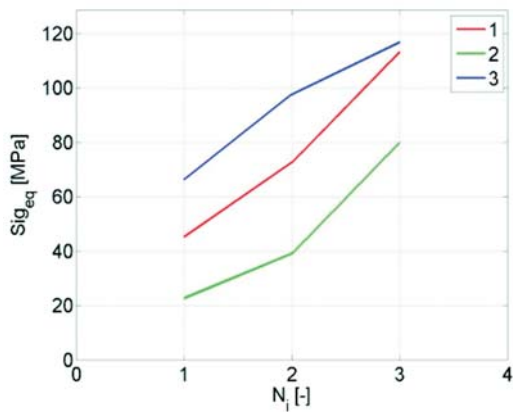


Fig. 12 History of stress convergence for 2nd algorithm

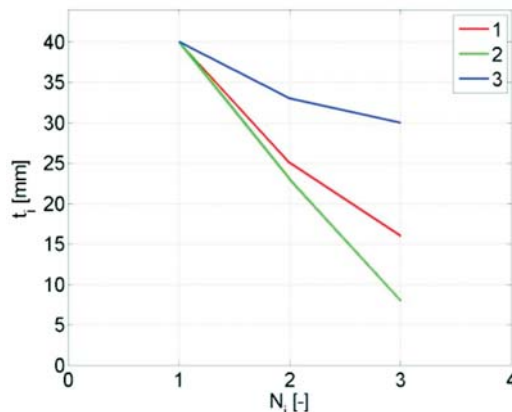


Fig. 13 History of thickness convergence for 2nd algorithm

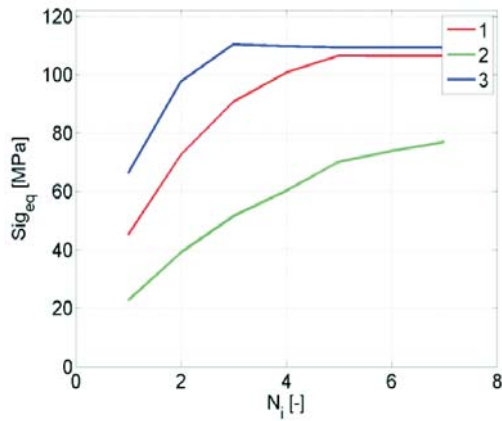


Fig. 14 History of stress convergence for 3rd algorithm

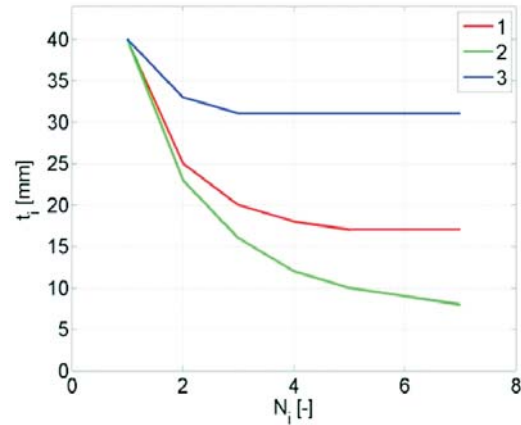


Fig. 15 History of thickness convergence for 3rd algorithm

The results of solution are summarized into Tables 1, 2 and Figures 10–15. Graphic presentation shows that classic FSD algorithm does not have to converge necessarily and in the case of the shell computational model the discrete optimization can be inconvenient. Other two presented algorithms have perspective and they converge very well. For problems with lower number of optimizing variables it is better to apply algorithm No. 2. Experiences of the authors indicate that the third algorithm is more suitable for problems with a higher number of optimizing variables (more than 10).

Table 1

Algorithm no. 2							
Iter. No.	t_1 [mm]	t_2 [mm]	t_3 [mm]	Stress_1 [MPa]	Stress_2 [MPa]	Stress_3 [MPa]	Weight [kg]
1	40	40	40	45.2	22.6	66.2	660
2	25	23	33	72.6	39.0	97.7	441
3	16	8	30	113.2	79.8	116.8	291

5. Conclusion

Our paper deals with the theoretical aspects and numerical realization of three fully stress optimizing algorithms focusing on shell finite elements models. The presented computational procedures were inbuilt into MATLAB's software module MAT_FSD which cooperates with FE software ADINA. Testing examples support the authors' considerations about the effectiveness of the proposed method.

References

[1] SAGA, M., VASKO, M., KOCUR, R., TOH, L., KOHAR, R.: *Application of Optimizing Algorithms in Solid Mechanics (in Slovak)*, VTS ZU Zilina, 2006.

Table 2

Algorithm no. 3							
Iter. No.	t_1 [mm]	t_2 [mm]	t_3 [mm]	Stress_1 [MPa]	Stress_2 [MPa]	Stress_3 [MPa]	Weight [kg]
1	40	40	40	45.1	22.6	66.2	660
2	25	23	33	72.6	39.0	97.7	441
3	20	16	31	90.7	51.5	110.1	363
4	18	12	31	100.7	60.2	109.8	329
5	17	10	31	106.5	70.2	109.4	313
6	17	9	31	106.4	73.9	109.3	308
7	16	8	30	113.2	79.8	116.8	291

The significant result of the presented study is mainly the fact that using of classical fully stress design method for shell structures modelled by means of the finite element method is inconvenient. The authors proposed two new algorithms which have overpassed this problem. These methods converge well, they are effective in the number of iteration steps and they have big perspective for large optimizing problems where the goal is to find hundreds of structural parameters by application of relatively low number of iteration steps.

Acknowledgements

This work has been supported by VEGA grant No. 1/0125/09.

- [2] HAFTKA, R. T., GURDAL, Z.: *Elements of Structural Optimization*. Kluwer Academic Publisher, 1992.
- [3] DEKYS, V., SAPIETOVA, A., KOCUR, R.: *On the Reliability Estimation of the Conveyer Mechanism using the Monte Carlo Method*. Proc. COSIM2006, Krynica-Zdroj, august 2006, pp. 67-74.
- [4] JAKUBOVICOVA L., KOPAS P., HANDRIK M., VASKO M.: *Computational and Experimental Analysis of Torsion and Bending Loading of Specimen*. In-Tech 2010, Prague, pp. 395-400.
- [5] LEITNER B., KOPAS P.: The Vector Autoregressive Moving Average Models Asa Tool for Stochastically Loaded Dynamic Systems Identification. *Machine Dynamics Research*, 2010, No. 4, vol. 34, pp. 32-41.
- [6] ZIENKIEWICZ, O. C.: *The Finite Element Method in Engineering Science*. McGraw, Hill, New York, 1971.
- [7] ZMINDAK, M., NOVAK, P.: Particles Interactions in Composites Reinforced by Fibre and Spherical Inclusions. *Communications - Scientific Letters of the University of Zilina*, No. 2, 2009.
- [8] ZMINDAK, M., RIECKY, D.: SOUKUP, J.: Failure of Composites with Short Fibers. *Communications - Scientific Letters of the University of Zilina*, No. 4, 2010.
- [9] SAGA, M., VASKO, M.: Stress Sensitivity Analysis of the Beam and Shell Finite Elements. *Communications - Scientific Letters of the University of Zilina*, vol. 11, No. 2, 2009, pp. 5-12.
- [10] KWON, Y. W., BANG, H.: *The Finite Element Method using MATLAB*. CRC Press University of Minnesota, 1996.
- [11] BATHE, K. J.: *Finite Element Procedures*. New Persey : Prentice Hall, 1996.
- [12] SAPIETOVA, A., DEKYS, V., VASKO, M.: A Numerical Modeling Rotating Machine Having Unbalance and the Measuring of its Dynamical Properties, *Metallurgija (Metallurgy)*, No. 2, vol. 49, 2010, pp. 503-507.

Vladimir Dekys – Jozef Broncek *

MEASURING STRAIN OF THE LATTICE TOWERS

The paper deals with strain measuring of bolted steel lattice high voltage tower structure on the test field. This measurement was associated to the test according to international standard IEC 60652, Ed. 2.0. If the tower is simulated as a truss structure and we expect the linear behavior of this object then the test data and calculation may show variations. The displacements of screw joint were detected as a source of this variation or non linear properties of structure. The key to this conclusion was detection of peak in measurement data.

Keywords: strain gauge, bolted lattice tower, non linearity, screw, peak detection

1. Introduction

The tests of the real objects are often expensive. The numerical models based on finite elements or meshless formulation play important role in estimating mechanical properties of these objects [1-4]. The models are necessary to verify the tests. In the case the test object is destroyed during test (according the test program) and the test is impossible to repeat with the same object then high demands are also placed on the preparation of test methods used, and related measurements.

This group includes the tests of bolted steel lattice high voltage tower structure, which are implemented in the company of our customer, according to specific customer requirements. The determination of deformation in selected parts of the tower was solved by the Faculty of Mechanical Engineering University of Zilina, Department of Applied Mechanics and Department of Design and Mechanical Elements. The paper deals with the preparation of measurement, its execution and interpretation of results. The interpretation will focus on possible sources of deviations between measured and calculated results.

2. The Basic Assumptions and Preparation of the Test

The subject test was bolted steel lattice high voltage tower structure made to the customer. The methodology for the test was prepared by customer according to international standard IEC 60652, Ed. 2.0. The tower was loaded by vertical and horizontal forces. First, there was a load force in the vertical direction to simulate the gravitational forces of ropes and ice, then there was a load tower in the horizontal direction, this simulates the effect of wind load acting perpendicular to the direction of power lines, Fig. 1. The strength in the horizontal direction was gradually step by step increased until the plastic deformation of the column correspond-

ing to the collapse of the structure. In describing the test was a requirement of determining the strain (deformation) in the axial direction of the trusses, due to tensile – compressive forces in the members truss structures. It was just assuming the presence of axial forces only and it was necessary to make measurements at selected locations L-tower profiles on both parts of the L-profile. The customer intends to compare own computational model with the experiment.

As the measuring points were also located at height up to 20 meters of ground on the assembled column and measurement should be made at temperatures below 0 °C, strain gauges and wires were installed on the chosen elements of the tower or the partially assembled parts of the tower in the production hall. The functionality of sensors was verified with wires and calibration was performed too. Checking and calibration was repeated after standing the tower on the test field, and also just prior to the test.

The strain gauges Micro-Measurement Division Vishay were used, namely CEA-06-250UW-120 and installation technology of Vishay too. The sensors were installed at the customers required locations. Some of the locations are shown in Fig. 1.

Four gauges were used in a full bridge connection, with two active gauges in the axial direction of member and two dummy gauges to eliminate temperature effects were placed transverse to the applied strain, Fig. 2.

The bridges were connected to the five cDAQ National Instruments 9237 modules (4 channel, 24-bit resolution, 50 kS/s/channel maximum sampling rate, cDAQ NI bridge module) in NI 9178 chassis, by using 8-wires cable. 8 wire connections allow to control the supply voltage to the bridge, eliminate the resistance of wires whose length was varied in the test and reached the 60 m and allows precision calibration of bridges [5]. This configuration was

* Vladimir Dekys, Jozef Broncek

Department of Applied Mechanics and Department of Design and Mechanical Elements, Faculty of Mechanical Engineering, University of Zilina, Slovakia, E-mail: vladimir.dekys@fstroj.uniza.sk

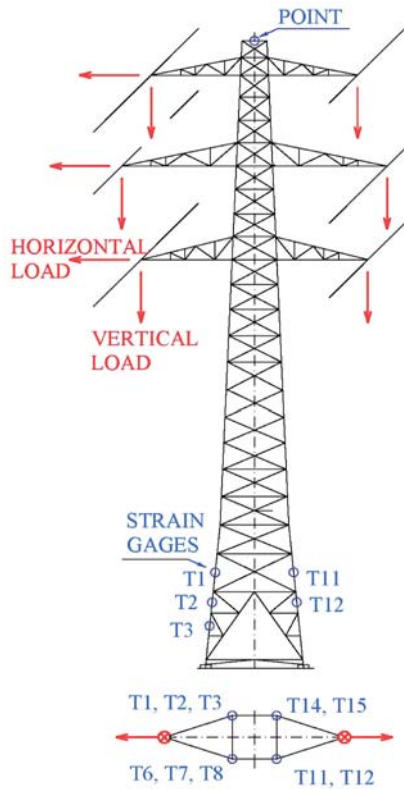


Fig. 1 Load of tower with chosen strain gauges places

also installed on the test element in the laboratory of the Faculty of Mechanical Engineering and the installation with the whole measuring string was verified on a test stand too. The properties installed sensors and the measuring system was also tested at ambient temperature below -10°C . It should be noted that the bridge does not eliminate the potential bending in members.

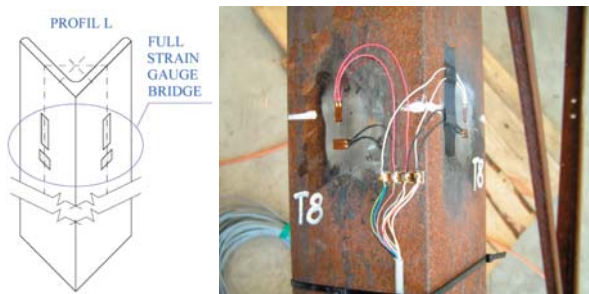


Fig. 2 A position of strain gauges on the chosen place of L-profile

The strain (deformation) $e_{\mu\epsilon}$ [$\mu\epsilon$] for different load stage is generally defined:

$$e = \frac{\Delta L}{L}, \quad 1\mu\epsilon = 10^{-6}, \quad e = 10^{-6}e_{\mu\epsilon} \quad (1)$$



Fig. 3. The test stand to verify the installation of strain gauges and the whole measuring chain

e [1] is the measured strain, [1],

L [1] is the active grid length of strain gauge, [m]

ΔL [1] is the change of active grid length of strain gauge, [m].

For full-bridge type III, [6]:

$$e = \frac{-2V_r}{GF[(\nu + 1) - \nu(\nu - 1)]}, \quad (2)$$

$$V_r = \frac{V_{CH}(\text{strained}) - V_{CH}(\text{unstrained})}{V_{EX}}$$

V_{CH} is the measured signal's voltage, [V],

V_{EX} is the excitation voltage, [V],

ν is the Poisson's ratio, defined as the negative ratio of transverse strain to the axial strain (longitudinal) strain, [1],

GF is gauge factor, [1].

The tensile - compressional force F [kN]:

$$F = EA(10^{-6}e_{\mu\epsilon})/1000, \quad (3)$$

E is Young's modulus of elasticity, [N/mm],

A is area of cross section, [mm].

The measured data are below the yield stress value, therefore the linear model is sufficient. In the case of the nonlinear region,

we have to use the tensile curve. Based on the shape of the tensile curve then we would determine the bilinear or multilinear model according to which the Young's modulus E would be changed in the formula (3).

3. Results

The results of measurement are depicted in Figs. 4-6.

In Fig. 4 is depicted strain - deformation of chosen parts versus number of samples. It presented step by step increasing of strain (in absolute value) according to the increase of horizontal load. Rapid decrease of compressive strain (divergence of curves) in bottom of Fig. 4 is important. If the top curves (tensile strain) presented linear increase of strain, then the bottom curves (compressive strain) presented non linear decrease.

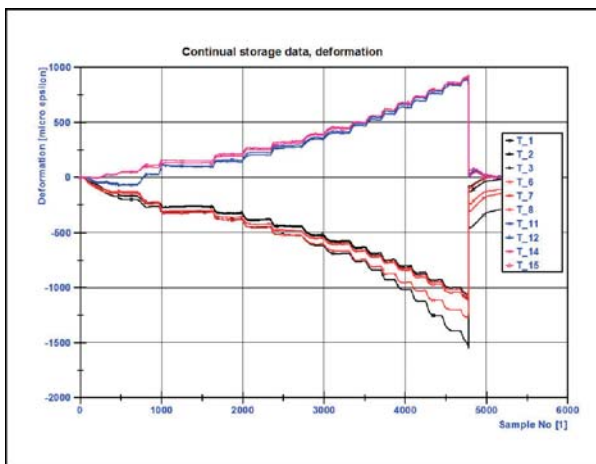


Fig. 4. An overall record of deformation (strain) in stepwise increasing of test load

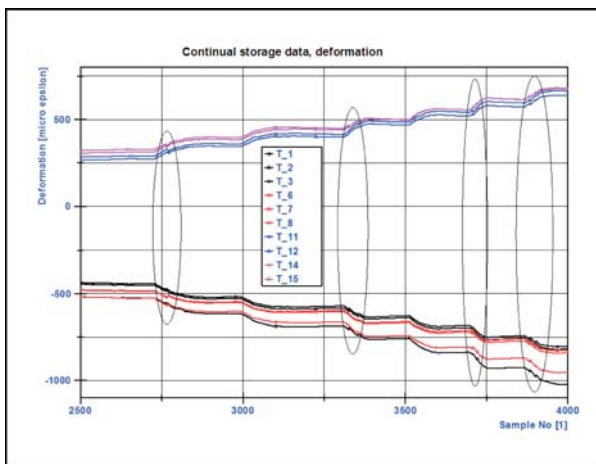


Fig. 5. Zoom of Fig. 4. Inside the ellipse are recognized peaks of strain

In Fig. 5 is depicted zoom of Fig. 4. Inside the ellipse are recognized peaks of strain. This phenomenon is explained as a displacement of parts of truss structure on the base tolerances in the holes of bolts.

In Fig. 6 is depicted zoom of Fig. 4 too. After this displacement are recognized next displacements in the bolt's holes, Fig. 4. This moment was recognized as a start of non linear properties of strain on the tested object.

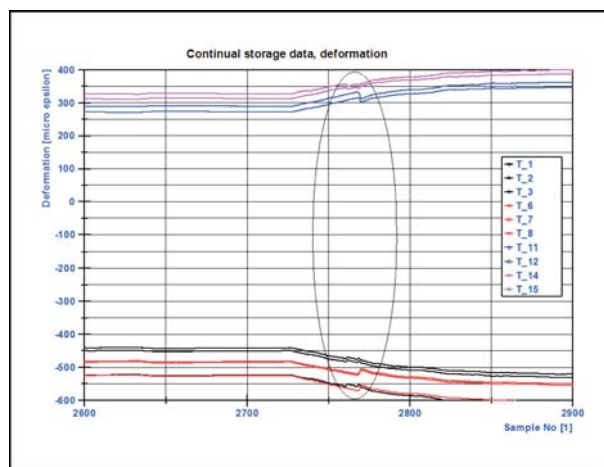


Fig. 6 Zoom of Fig. 4. Inside the ellipse are recognized peaks of strain

In Fig. 7 is depicted zoom of Fig. 4 for T_1, average values and original data stored with sampling frequency of 1 kHz. The displacement is recognized, it is marked with ellipse.

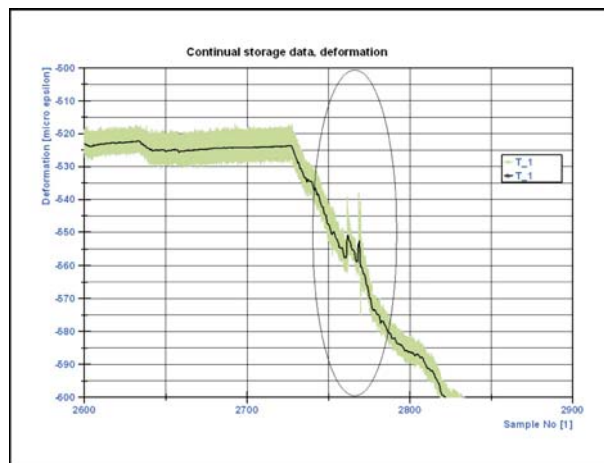


Fig. 7 Zoom of Fig. 4. Inside the ellipse are recognized peaks of strain, black - average data and grey - original stored data with sampling frequency of 1kHz

4. Conclusion

The objective of the paper was to present the experiences with strain measurements of bolted steel lattice high voltage tower structure and interpret non linear properties of measured strain. The displacements of members truss structure in screw bolts is presented in measurement data as a start of this non linear relation. The displacement of elements can cause a violation of the construction and the location of loading forces can be changed too.

The peaks are presented in the strain measured data. These changes are not implemented in usual computers models. The plastic deformation of truss is not source the peaks identified in the measured data in this paper. The next step will be formulation of this problem as a task with uncertainty parameters, [7].

Acknowledgement

The work has been supported by the grant project VEGA 1/1000/12 and 1/1259/12.

References

- [1] SAGA, M., VASKO, M.: Stress Sensitivity Analysis of the Beam and Shell Finite Elements. *Communications - Scientific Letters of the University of Zilina*, vol. 11, No. 2, 2009, pp. 5-12.
- [2] KOMPIS, V., TOMA, M., ZMINDAK, M., HANDRIK, M.: Use of Trefftz Functions in Non-linear, BEM/FEM, *Computer and Structures*, vol. 82, 2004, pp. 2351-2360.
- [3] MELICHER, R., MESKO, J., NOVAK, P., ZMINDAK, M.: Residual Stress Simulation of Circumferential Welded Joints. *Applied and Computational Mechanics*, vol. 1, No. 2, 2010, pp. 541-544.
- [4] SAGA, M., KOPAS, P., VASKO, M.: Some Computational Aspects of Vehicle Shell Frames Optimization Subjected to Fatigue Life. *Communications - Scientific Letters of the University of Zilina*, vol. 12, No. 4, 2010, pp. 73-79.
- [5] Connecting Strain Gauges and Shunt Resistors to the NI 9237, <http://digital.ni.com/public.nsf/allkb/892C84122A6501AE86257547007E5C53>
- [6] Strain Gauge Configuration Types, <http://zone.ni.com/devzone/cda/tut/p/id/4172#toc9>
- [7] VASKO, M., SAGA, M.: Solution of Mechanical Systems with Uncertainty Parameters using IFEA, *Communications - Scientific Letters of the University of Zilina*, vol. 11, No. 2, 2009, pp. 19-27.

Alzbeta Sapietova – Milan Saga – Pavol Novak *

MULTI-SOFTWARE PLATFORM FOR SOLVING OF MULTIBODY SYSTEMS SYNTHESIS

The paper deals with design and application of multi-software platform for solving of mechanical multi-body system problems. The Adams working interface and open architecture of Matlab programming language enable share common data during parallel run of simulations. This process was used for design and implementation of evaluation algorithm and optimization of technical equipment parameters in terms of their mechanical properties. The goal is to present the mapping process of the working space of the chosen manipulating equipment and application of the optimizing approach to find its geometry parameters. Multi-software technique will be applied for computational realization i.e. Adams and Matlab.

Key words: coupled mechanical system, optimization, Matlab, ADAMS

1. Introduction

Modeling can play an important role in the analysis and design of flexible multibody systems. Recent developments in commercial FEA packages allow to the designer to make the detailed analysis of composites structures, too [1, 2].

The problem during the production machine synthesis solving is to find the suitable construction and the corresponding suitable parameters of the mechanism (i.e. materials, dimensions of body shapes and cross-sections, algorithms for the movement controlling, etc.). The parameters must fulfill some functional and technological requirements. These requirements may relate only to the position of the mechanism elements. In this case we call it the geometrical synthesis. In the other cases we must deal with the velocity and acceleration requirements. The methods solving these problems are the scope of the kinematics synthesis.

The dynamical requirements (i.e. balancing, reaction forces reduction, motion irregularity reduction, required motion properties, etc.) are solved by the dynamical synthesis [3].

The area of the mechanism synthesis has been primarily defined as a relationship between the input and the output (1:1). However, this area is more complicated for the production machine mechanisms and it covers the whole mechanics and the control area. The solutions can be characterized as multiple inputs – outputs (M:N). Therefore it is needed to extend the traditional mechanic techniques with the techniques focused on the general design theory [3].

2. Files preparation for the kinematics synthesis of the rigid system virtual prototype

The solution objective is to design and implement the algorithm of the evaluation of the operating gear parameters from the mechanical properties view [4]. The approach is based on the solution of the fixed solid system (FSS) virtual prototypes by means of the computer simulation, using the kinematics and the optimization [5, 6]. There is tendency to eliminate the time-consuming analyses so that the program interconnection of the ADAMS and MATLAB systems will be designed and implemented. For the inverse kinematics problem solving the virtual prototype (VP) manipulator robot was chosen (Fig. 1). The solution contains the following processes:

- Virtual prototype preparation in the ADAMS/View environment,
- modification of the simulation,
- creation of an “*.acf” file,
- data export into an “*.adm” file,
- creation of programs in MATLAB environment,
- inverse kinematics problem,
 - the creation of the point of interest working positions map,
 - the movement trajectory specification for the point of the interest,
 - the selection of the points from the working positions map that copy the prescribed trajectory in the best way,
 - the optimization of the rigid system element lengths.

* Alzbeta Sapietova, Milan Saga, Pavol Novak

Department of Applied Mechanics, Faculty of Mechanical Engineering, University of Zilina, Slovakia, E-mail: alzbeta.sapietova@fstroj.uniza.sk

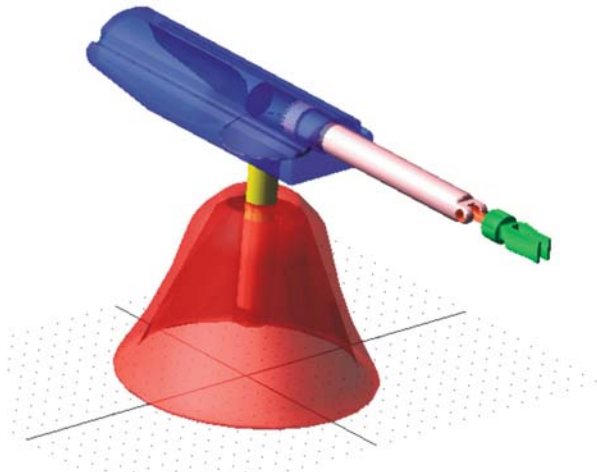


Fig. 1 Virtual prototype manipulator robot in environment ADAMS/View

2.1 Virtual prototype preparation in the ADAMS/View environment

The particular elements of the manipulator robot were designed in the ADAMS/View environment. Kinematic schema of the manipulating equipment has four movement degrees of freedom (Fig. 2). Quantity “ v ” is speed of motion and quantity “ ω ” is angular velocity.

During the creation of virtual prototypes the models in the ADAMS environment are saved in the various file formats according to their purpose. The manipulator robot was created in the binary file format (model.bin). This database contains the information about the working space configuration, all properties of one or more models and the analyses and the simulations results too.

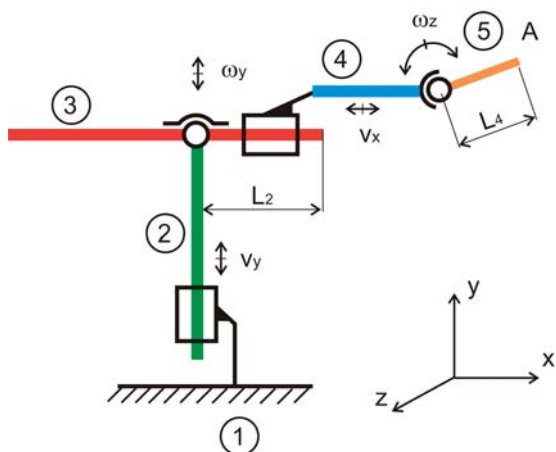


Fig. 2 Kinematic schema of manipulating equipment

The binary format allows the quick writing and loading of the data and it can be transferred between computers with the different operating systems but it does not allow their reading and editing.

2.2 Modification of the simulation

In the modification of the simulation, the prescribed process of the movements for all working cycles is defined. Modification of the simulation is created so that motion was directed gradually. In the particular joints the following movements are prescribed (Fig. 2 , Fig. 3):

MOTION_1 ["-1*time"]	% displacement PART_2 - v_y
MOTION_2 [-200]	% persistence of the PART_2 in the given position
MOTION_3 ["1d*(time-200)"]	% rotation of the PART_3 - ω_z
MOTION_4 [180d]	% persistence of the PART_3 in the given position
MOTION_5 ["1*(time-380)"]	% displacement PART_4 - v_x
MOTION_6 [100]	% persistence of the PART_4 in the given position
MOTION_7 ["-1d*(time-480.0)"]	% rotation of the PART_4 - ω_z

When the solid moves and it needs to stop afterwards, the zero movement must be activated for it in the time of the stop. Therefore more movements (MOTION_1, MOTION_2) are included into the JOINT (Fig. 3).

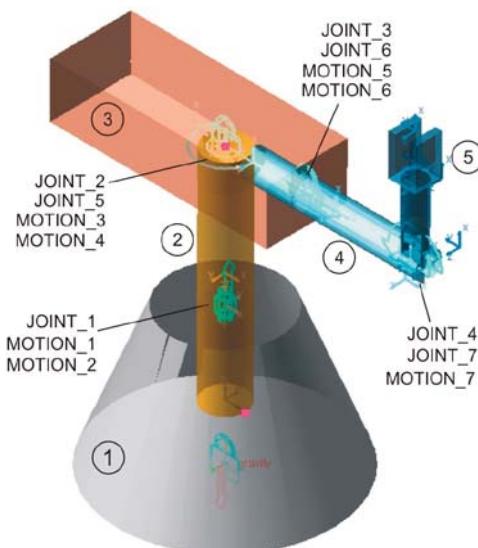


Fig. 3 Joints and motions of the manipulating equipment

Functionality of the virtual prototype (VP) is verified by the simulation in ADAMS/View environment and the kinematic parameters are calculated. Diagrams in Figs 4 to 6 illustrate trajectory of centre of gravity of particular parts.

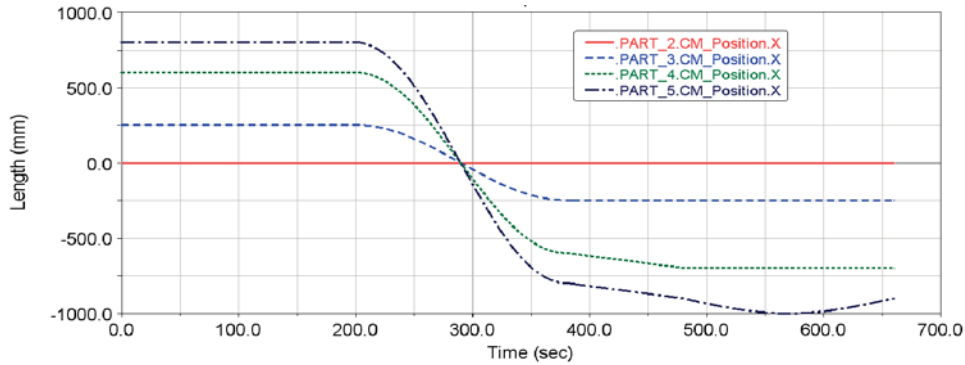


Fig. 4 Trajectory of centre of gravity of particular parts - position x

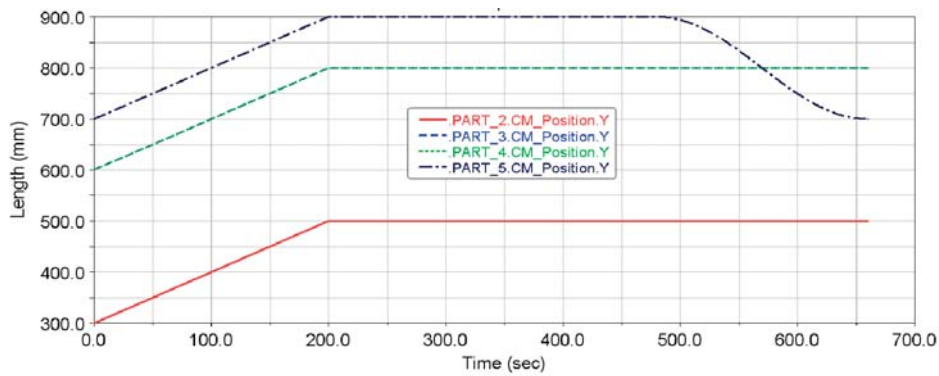


Fig. 5 Trajectory of centre of gravity of particular parts - position y

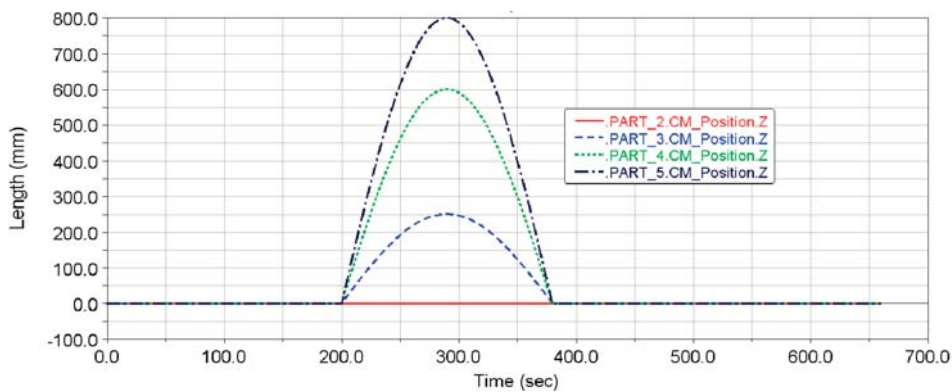


Fig. 6 Trajectory of centre of gravity of particular parts - position z

2.3 Creation of an “*.acf” file

Values for simulation modification instruction are stored into the new created file with “*.acf” suffix. This file can be imported into ADAMS environment with the aim to run ADAMS/Solver with the prescribed movement simulation modification and the consequent system solution.

2.4 Data export into an “*.adm” file

Model in the “*.adm” format is the record in its most saving form for sending to the ADAMS/Solver environment. It contains the data only for one model; it does not store the environment configuration. The advantage is the ASCII format in which the “*.adm” file can be comfortably read, edited and transferred between com-

puters with the different operating systems. This file can be again imported into ADAMS environment in order to run the ADAMS/ Solver.

2.5 Creation of programs in MATLAB environment

Programs created in the MATLAB environment control the computation approach. These programs are stored in the following files:

- *Optim_GENERAL.m* - this file contains optimization methods with the call of *dona.m*,
- *dona.m* - the file for computation of the objective function and for the solution of the point positions with the minimal distance from the prescribed trajectory. This program calls the subprogram *runAdams.m*,
- *runAdams.m* - it runs the ADAMS system and creates the result file *model.res*,
- *opt_uhl.m* - it optimizes the output parameters, e.g. angles of rotation in order to obtain the continuous movement.

2.6 Inverse kinematics problem

The inverse kinematics problem solves the suitable input kinematic parameters multibody of the systems (MBS) for obtaining the described movement [4]. The graphical diagram of the particular program relations is shown in Fig. 7. Assuming the stepping motor realistic usage with step of 5 degrees, all working positions of the manipulator robot endpoint "A" are mapped (Fig. 8). Prescribed trajectory of the point "A" is a helix (Fig. 9). From the obtained working position map the coordinates of those points were chosen which correspond with the prescribed trajectory in the best way and which meet the condition of the continuous movement MBS at the same time.

The input kinematics parameters ensuring the given element prescribed movement MBS are the solution results. The chosen results of the rotation angle values and displacements are shown

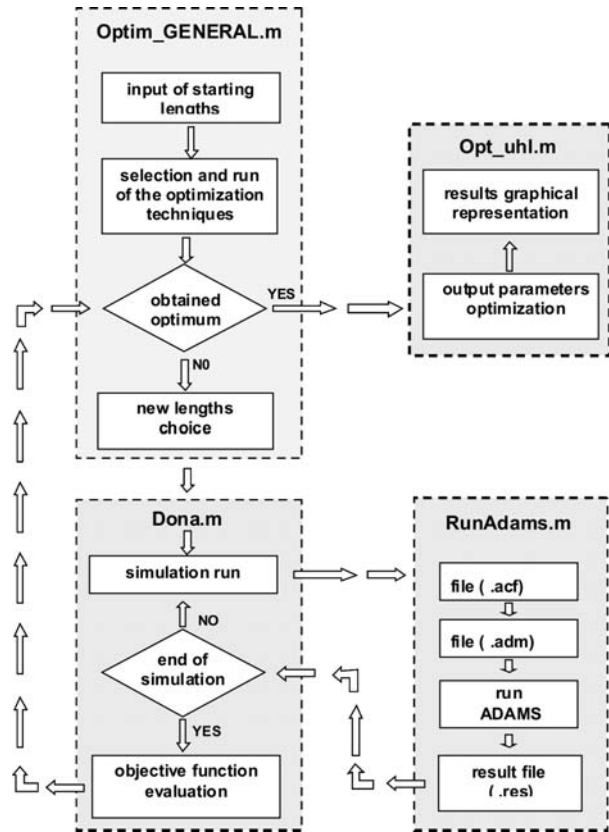


Fig. 7 Graphical representation of the inverted kinematics problem solution

in Tab. 1. Their number depends on the solution step size. Parameter "r" is minimal distance of the solved point from trajectory.

The genetic algorithm method was used. The objective function value was a numerical zero. In order to obtain the continuous movement the optimal length value was used in the program *opt_uhl.m*.

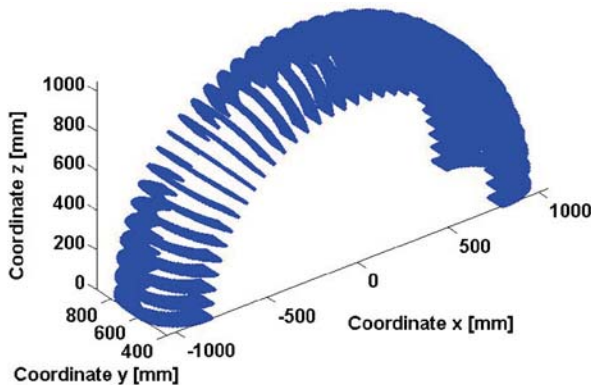


Fig. 8 Point "A" - map of working positions

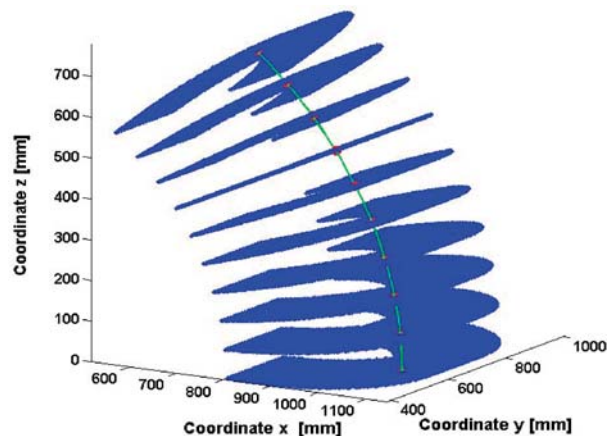


Fig. 9 Point "A" - map of working positions

2.6.1 Optimization of geometric parameters of a manipulator.

From the working positions map the points closest to prescribed trajectory were selected. Due to closer following of prescribed trajectory by end point of the manipulator, optimization of lengths of selected parts was involved. The solution algorithm was as follows:

- working positions map for point “A” contains n points, i.e. positions of point “A” on real trajectory k_1 ,
- on the prescribed trajectory k_2 n key points were defined - required positions of point “A”.
- Next, we minimize objective function F , which is a vicinity criterion of trajectories k_1 and k_2 :

$$F(L_2, L_4) = \sum_{i=1}^n \sqrt{dx_i^2 + dy_i^2 + dz_i^2} \rightarrow \min ,$$

where

$$dx_i = [x_i(L_2, L_4)]_{k_1} - [x_i]_{k_2},$$

$$dy_i = [y_i(L_2, L_4)]_{k_1} - [y_i]_{k_2},$$

$$dz_i = [z_i(L_2, L_4)]_{k_1} - [z_i]_{k_2}.$$

where $[x_i, y_i, z_i]_{k_2}$ are coordinates of point “i” on the prescribed trajectory and $[x_i(L_2, L_4), y_i(L_2, L_4), z_i(L_2, L_4)]_{k_1}$ are coordinates of point “i” on the real trajectory for given design iteration. Lengths L_2 and L_4 are design variables (Fig. 2). Initial values of design variables were $L_2 = 500$ mm, $L_4 = 200$ mm. The optimal values of the manipulator robot element lengths are: $L_2 = 515.92$ mm, $L_4 = 191.85$ mm (Fig. 2).

Pattern search function from Matlab Optimization Toolbox was used to design an optimization problem. The algorithm of this

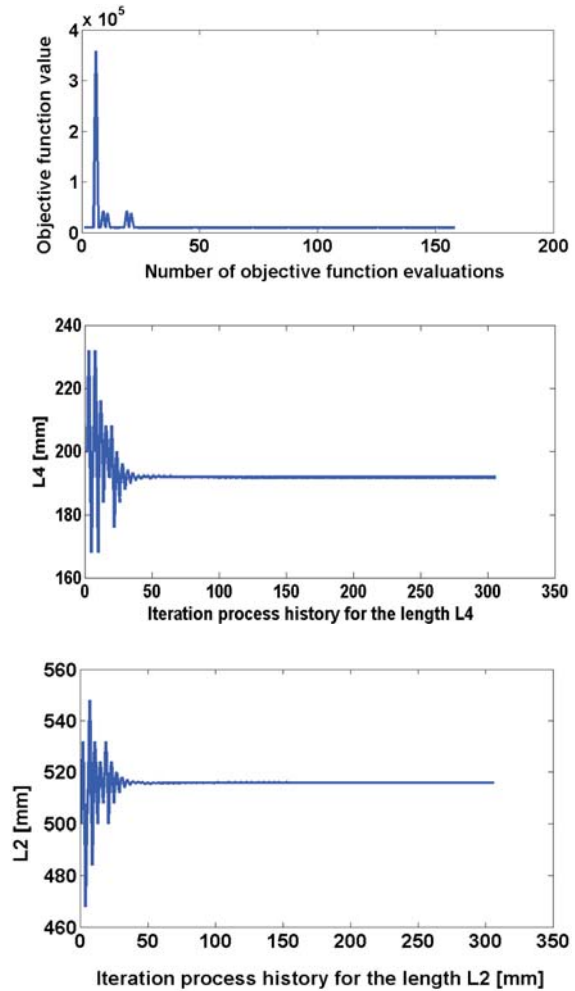


Fig. 10 Iteration process history

Evaluation of monitored values in the MBS synthesis.

Table 1

Displacement Part_2 (mm)	Angle Part_3 (°)	Displacement Part_4 (mm)	Angle Part_5 (°)	Position x (mm)	Position y (mm)	Position z (mm)	Min distance (mm)
60	2.5	50	80	1022.09	549.95	44.62	0.07
80	7.5	30	80	1014.31	569.95	133.53	17.85
100	10	30	80	1007.52	589.95	177.65	8.92
10	15	15	45	987.91	610.0	264.71	8.92
30	17.5	15	45	975.42	630.0	307.55	17.85
50	22.5	15	45	944.91	650.0	391.39	0.23
70	27.5	15	45	907.20	670.0	472.25	17.85
90	30	15	45	885.73	690.0	511.38	8.92
0	35	35	10	838.04	710.04	586.80	8.92
20	37.5	35	10	811.65	730.04	622.80	17.85
40	42.5	35	10	754.28	750.04	691.17	0.07

function is based on GA principles. Iteration history and solution history for design variables are shown in Fig. 10.

3. Conclusion

The goal of the paper was to suggest and apply the approach for the synthesis solution and the consequent manipulation device analysis using the interconnection of ADAMS and MATLAB programs. By reason of significant requirements for accuracy, economy, reliability and operating lifetime of technical equipment it is necessary to consider several parameters that secure the optimal product.

For that reason the next step is interconnection between simulation models and software for numerical optimization that enabled iterative improvement of the designed system. This was made on the base of exact optimization methods. From the experiences obtained during the problem solution, the next goals can be formulated; to modify the program in order to shorten the computation times and to use the whole range of possibilities offered by the ADAMS software.

Acknowledgement

The part of the results of this work has been supported by VEGA grant No. 1/1259/12 and the VEGA grant No. 1/1000/12.

References

- [1] KORMANIKOVA, E., RIECKY, D., ZMINDAK, M.: Strength of Composites with Short Fibers. In: Eds, J. Murin: Computational Modelling and Advanced Simulations, Springer Series: *Computational Methods in Applied Sciences*, vol. 24, 2011, ISBN 978-94-007-0316-2
- [2] ZMINDAK, M., RIECKY, D.: SOUKUP, J.: Failure of Composites with Short Fibers. *Communications - Scientific Letters of the University of Zilina*, No. 4, 2010. ISSN-13354205
- [3] VALASEK, M.: *Synthesis of Mechanisms of Production Machines*. In *22th Conference with Intern. Participation, Computational Mechanics*, 2006, Plzen : TYPOS-Digital Print, s.r.o., ISBN 80-7043-477-5, p. 29-38.
- [4] ARNOLD, M., SCHIEHLEN, W.: Simulation Techniques for Applied Dynamics, *CISM Courses and Lectures*, vol. 507, Italy : Springer Wien : New York, 2008, p. 313, ISBN 978-3-211-89547-4.
- [5] DE JALLON, J. G., BAYO, E.: *Kinematic and Dynamic Simulation of Multibody Systems. The Real-Time Challenge*, Springer-Verlag, New-York, 1994, p. 440, ISBN 0-387-94096-0.
- [6] SEGLA, S., CIUPITU, L., REICH, S.: Optimization of a Spring Balancing Mechanism for Parallelogram Robot Mechanisms. In *J. Mechanisms and Manipulators*, ISSN 1583-4743, 2006, vol. 5, No. 2, 2006, pp. 43-48.

Radoslav Konar – Milos Mician *

NUMERICAL SIMULATION OF RESIDUAL STRESSES AND DISTORTIONS IN BUTT WELD IN SIMULATION PROGRAMME SYSWELD

The article describes the theoretical knowledge of the residual stresses induced during welding in butt welded joint and the possibilities of their simulations in a simulation programme SYSWELD. In conclusion are compared experimental and simulated results.

Keywords: Butt weld, steel S355J2G3, SYSWELD.

1. Introduction

Welding induced residual stress and distortions are among the most situated subjects for welded structures. The localized heating and non-uniform cooling during welding results in a complex distribution of the residual stress in the joint region, as well as the often undesirable deformation or distortion of the welded structure. As residual stress and distortion can significantly impair the performance and reliability of the welded structure, they must be properly dealt with during design, fabrication and in-service use of the welded structures [1].

2. Theoretical part

2.1. Residual stress and distortions

In a welded joint, the expansion and contraction forces act on the weld metal and its adjacent base metal. As the weld metal solidifies and fuses with base metal, it is in its maximum expanded state. However, at this point, the weld metal and its adjacent base metal absorbed the high temperatures and have little strength or rigidity. The volume expansion caused local thickening in the weld area but is incapable of causing a significant amount of plastic strains in the cooler joint neighborhoods. On cooling, it attempts to contract to the volume that it would normally occupy at the lower temperature, but it is restrained from doing so by the adjacent cooler base material. Stresses develop within the weld, finally reaching the yield strength of weld metal. At this point the weld stretches, or yields and thins out, thus adjusting to the volume requirements of the lower temperature, but only those stresses that do not exceed the yield strength of the weld metal, or the elastic mechanical strain, are relieved by this accommodation [1].

Residual stresses are a consequence of interactions among time, temperature, deformation and microstructure (Fig. 1). Material or material-related characteristics that influence the development of residual stress include thermal conductivity, heat capacity, thermal expansivity, elastic modulus and Poisson's ratio, plasticity, thermodynamics and kinetics of transformations, mechanisms of transformations, and transformation plasticity [2].

The fundamental material properties are, of course, temperature dependent. Fig. 1 illustrates how several key properties might vary with temperature [2].

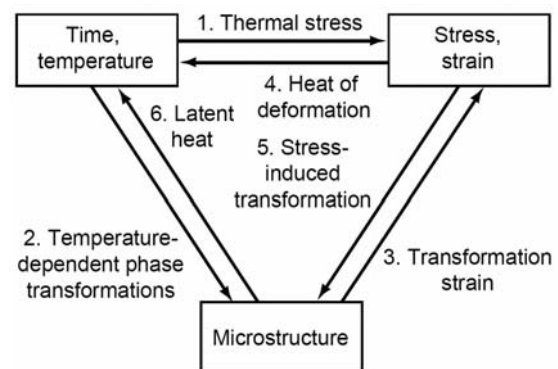


Fig. 1 The coupling of temperature, stress and microstructure [2]

Fig. 2 divides the development of residual stresses in welded seams in three different mechanisms [3].

* Radoslav Konar, Milos Mician

Department of Technological Engineering, Faculty of Mechanical Engineering, University of Zilina, Slovakia, E-mail: radoslav.konar@fstroj.uniza.sk

Shrinking stresses: these are stresses formed through uniform cooling of the seam. Caused by expansion restriction of the colder areas at the edge of the weld and base material, tensile stresses develop along and crosswise to the seam.

Quenching stresses: If cooling is not homogenous, the surface of the weld cools down faster than the core areas. If the high-temperature limit of elasticity is exceeded due to buildup stress differences, pressure stresses will be present at the weld surface after cooling. In contrast, the core shows tensile stresses in cold condition.

Transition stresses: Transitions in the ferrite and perlite stage cause normally only residual stresses, because within this temperature range the yield strength of the steel is so low that generated stresses can be undone by plastic deformations [3].

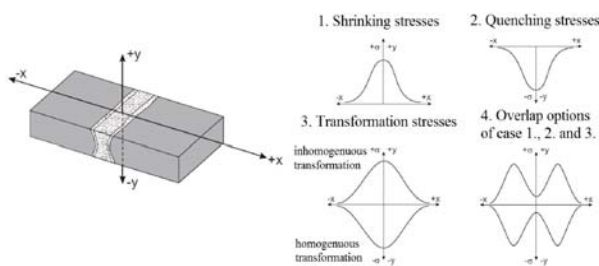


Fig. 2 Development of residual stresses [3]

The plastic strain results in permanent deformation of the welded structure after the welding. This is called welding-induced distortion. The mode of welding-induced distortion could show up in-plane deformation such as stretching and out-of-plane deformation such as bending, rotation or buckling. Typical welding-induced distortion is shown in Fig. 3 [2].

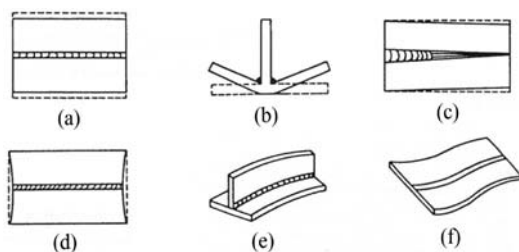


Fig. 3 Various types of welding-induced distortion (a) transverse shrinkage, (b) angular change, (c) rotational distortion, (d) longitudinal shrinkage, (e) longitudinal bending distortion, (f) buckling distortion [2]

2.2. SYSWELD

SYSWELD is a Finite Element software that simulates all usual welding processes such as MMA, MIG, TIG, spot welding, laser welding, heat treatment like bulk hardening, surface hardening, tempering and hardening and tempering, as well as thermo-chemical treatment like case hardening, carbonitriding, nitriding [1].

Simulation of a welding process requires two successive analyses:

- first a thermo-metallurgical analysis,
- followed by a mechanical analysis.

2.2.1 Definition of heat source in SYSWELD

Simulation system SYSWELD used for numerical calculations of heat following heat sources: 2D Gaussian model – for surface thermal treatment of material, 3D Gaussian model – for simulation of welding with high power density in impact area and 3D Glodak model – for shielded metal arc welding, submerged arc welding, GTAW, GMAW. Just because of great using variability will be this type of heat source closely described [4].

3. Experimental part

This experiment includes analysis of boundary conditions for the simulation of welding in butt weld and simulation thermal analysis, welding-induced distortion and residual stress in simulation programme SYSWELD.

3.1. Experimental sample

Model used for the experiment was compounded of two plates of materials S355J2G3. Chemical composition and mechanical properties of steel are in Tab. 1.

Both of the plates have same geometrical properties (250 × 50 × 7mm). The fusion faces were prepared according to scheme in Fig. 4. Two parts of experimental sample were tack-welding together without root gap. Run-on and run-off plates were used in welding process. Experimental sample was prepared for welding. Welding joint was welded using the mechanized GMAW process. Constant welding speed was secured by a welding truck.

3.2. Experimental measurements before, during and after welding

Before welding were measured distortion in y-axis of sample in 9 points (Fig. 4), during welding were measured welding parameters and thermal cycles in three points. After welding and cooling to ambient temperature (20 °C) were measured distortions again. Distortions in y-axis were measured from reference point. Displacements were measured with a mechanical standing micrometer.

Chemical composition and mechanical properties of steel S355J2G3

Table 1

Chemical composition								
max. %	C	Si	Mn	P	S	V	Nb	Ti
S355J2G3	0.20	0.55	1.60	0.035	0.035	-	-	-
Mechanical properties								
S355J2G3	R _m [MPa]		R _e [MPa]		A ₅ [%]		KV [J]	
	min. 490		min. 355		min. 20		min. 27	

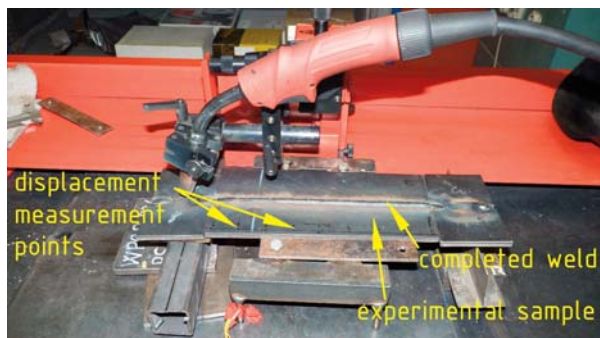
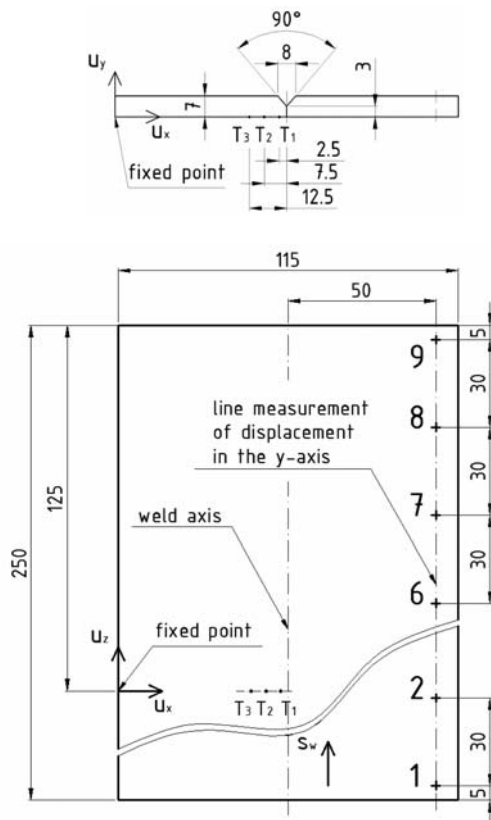


Fig. 4 Experimental sample, scheme (up), real sample (down)

Model was fixed on plane table in fixed point during displacement measurement with mechanical clamp. After all measurements the weld was analyzed. Complete analysis of weld for simulation in simulation programme SYSWELD contains:

- parameters of welding U_w, I_w (Tab. 2)
- cross-sectional geometry of the welds (weld metal, heat affected zone),
- welding speed (s_w),
- thermal cycles,
- distortions in y-axis (Tab. 3).

Parameters of welding

Table 2

Parameters of welding		
Welding current	I_w [A]	177
Welding voltage	U_w [V]	20
Welding speed	s_w [mm.s ⁻¹]	4.9
Wire feed rate	r_{wf} [m.min ⁻¹]	8
Gas flow rate	r_{gf} [l.min ⁻¹]	12
Welding wire diameter	d_{ww} [mm]	1.2
Real heat input ($\eta = 0,85$)	Q_r [J.cm ⁻¹]	6141

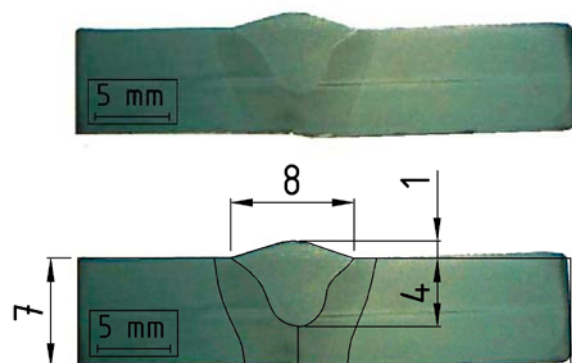


Fig. 5 Macrostructural analysis (up) and digitized macrostructure (down)

Digitizing of weld macrostructures, we get cross-sectional parameters of welds (Fig. 5), which are necessary for the definition of Goldak heat source model and FEM model creating.

Measured displacements of points in y-axis

Table 3

Measured displacements of points in y-axis [mm]									
Point	1	2	3	4	5	6	7	8	9
Displacement	0.54	0.51	0.49	0.47	0.46	0.47	0.49	0.51	0.54

Temperature cycles were measured by three thermocouples T_1, T_2, T_3 . Their location is shown in Fig. 4 and its graphic view in Fig. 6. Characteristic attributes of temperature cycles are in Tab. 4.

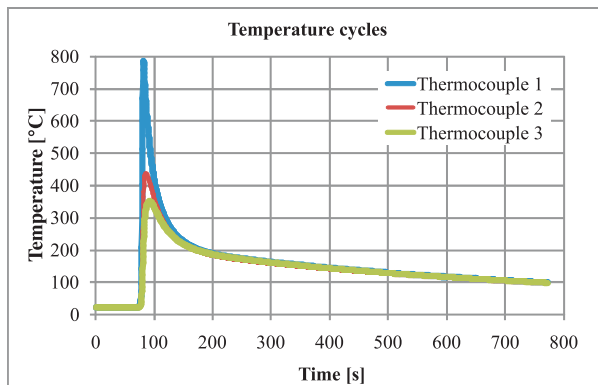


Fig. 6 Measured temperature cycles in three thermocouples

Characteristic attributes of measured temperature cycles Table 4

Characteristic attributes of temperature cycles			
Thermocouple	T_{max} [°C]	r_{300} [°C.s ⁻¹]	t_{100} [s]
1 st	785	3.91	683
2 nd	437	3.81	643
3 rd	350	3.42	662

Experimental results will serve as a boundary condition for the simulation in simulation programme SYSWELD.

3.3. Numerical simulation of welding in simulation programme SYSWELD

Numerical simulation process consists of several following steps:

1. Creating geometrical model and its distribution to FEM mesh,
2. Definition of input data and boundary condition,
3. Simulation and presentation of results.

The model has the same geometrical dimensions as the experimental sample. Meshed FEM model can be seen in Fig. 7. Distribution model has 57706 finite elements and 49843 nodes. The smallest element used in the FEM model is in the area of the weld with the dimension of 1.0 mm × 1.0 mm × 1.25 mm.

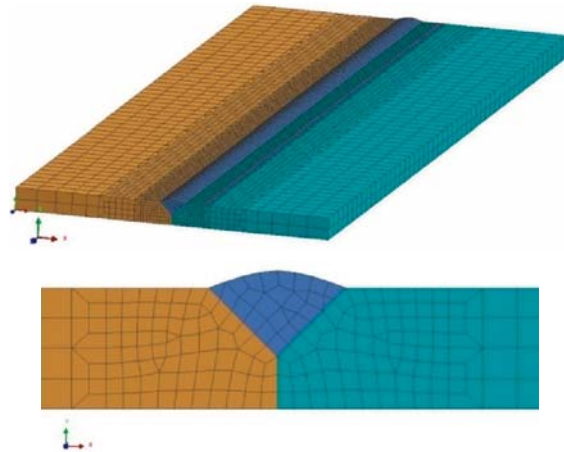


Fig. 7 FEM model of experimental sample

Input data and boundary conditions used for simulation of thermal analysis are: material database of the model was steel S355J2G3. Parameters of Goldak are in Tab.5.

Parameters of Goldak model Table 5

Parameters of Goldak model		
c_1	[mm]	2
c_2	[mm]	4
a	[mm]	4
b	[mm]	4.25
Q	[W]	3050

In the thermal analysis, temperature fields, temperature cycles were simulated. Graphic results of the simulation are in Figs. 8 and 9.

Characteristic attributes of simulated temperature cycles are in Tab. 6.

Characteristic attributes of simulated temperature cycle Table 6

Characteristic attributes of temperature cycles			
Thermocouple	T_{max} [°C]	r_{300} [°C.s ⁻¹]	t_{100} [s]
1 st	866	3.75	690
2 nd	500	3.75	685
3 rd	398	3.75	670

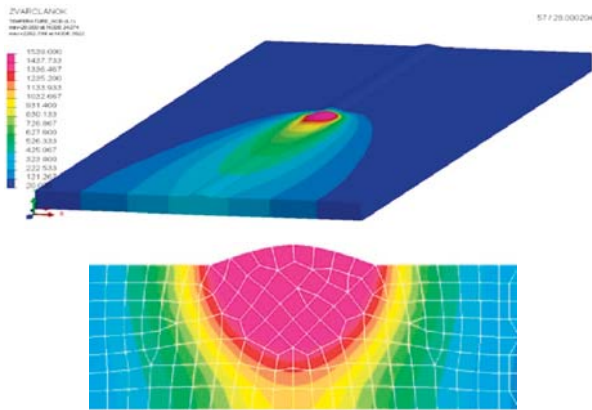


Fig. 8 Simulated temperature fields

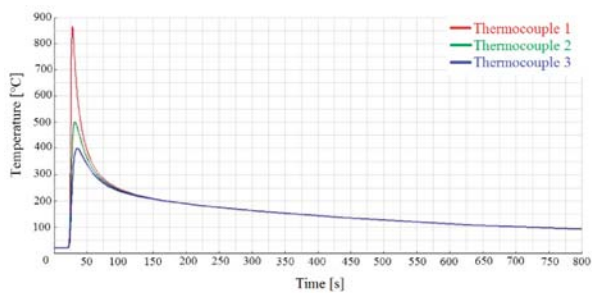


Fig. 9 Simulated temperature cycles in three thermocouples

Free boundary conditions of FEM model were used to calculate mechanical analysis. Free location of model can be seen in Fig. 10. Residual stresses and distortion were simulated in the mechanical simulation. Graphic results of the mechanical simulation are in Figs. 11, 12 and Tab. 7.

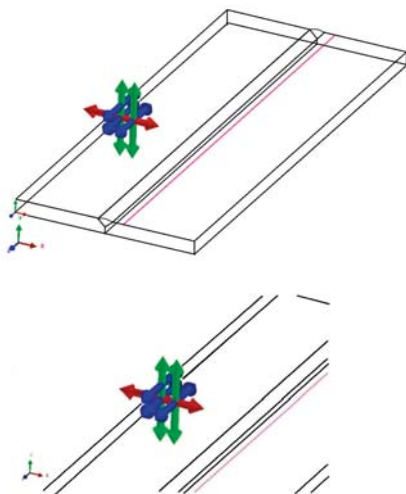


Fig. 10 Clamping condition for mechanical analysis

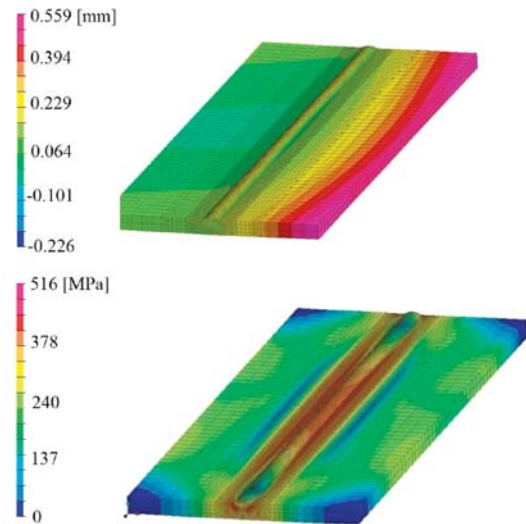


Fig. 11 Simulated displacements in y-axis (up) and residual stresses by Von Mises (down)

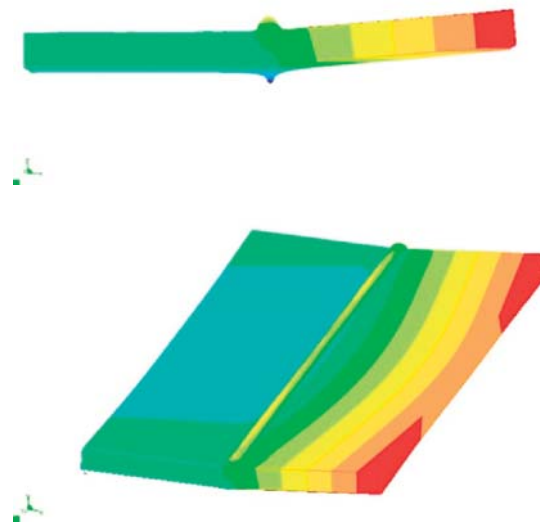


Fig. 12 Deformed shape of FEM model (deformed scale 10)

3. Conclusion

Theoretical part of the paper includes information about residual stresses induced during welding and welding simulation in programme SYSWELD. Experimental part includes analysis of boundary conditions and simulation of welding in butt weld. Experimental and simulation results are almost identical. The maximal difference between experimental and simulated characteristic para-

Simulated displacements of points in y-axis

Table 7

Simulated displacements of points in y-axis [mm]									
Point	1	2	3	4	5	6	7	8	9
Displacement	0.52	0.51	0.53	0.53	0.53	0.55	0.54	0.50	0.51

meters of temperature cycles are 10% and in results of displacements are 14%. Exactly the same results cannot be reached, because many factors (boundary condition, input data and definition of heat source) influence them.

Welding simulation has become a strong tool in technological praxis. It helps efficiently to solve complex problems in welding in a relatively short time.

Acknowledgement

This work has been supported by the Scientific Grant Agency of Ministry of Education of the Slovak Republic, grant VEGA No. V-11-015-00 and KEGA No. K-11-008-00.

References

[1] FENG, Z.: *Processes and Mechanisms of Welding Residual Stress and Distortion*. CRC Press, USA, 2005. ISBN 978-0-8493-3467-2
 [2] TOTTEN, G., HOWES, M., INOUE, T.: *Handbook of Residual Stress and Deformation of Steel*. AMS International, Materials Park, 2002, ISBN 0-87170-729-2
 [3] <http://mercury.kau.ac.kr/welding/Welding%20Technology%20II%20-20Welding%20Metallurgy/Chapter%203%20-%20Residual%20Stresses.pdf>
 [4] MORAVEC, J.: *Influence of Welding Parameters on Weld Pool's Geometry in Shielding Gas Welding*. POLLYPRESS s.r.o., Liberec, 2011. ISBN 978-80-7372-805-2

Slavomir Hreck – Robert Kohar – Stefan Medvecký *

DETERMINATION OF THE MAXIMUM ROLLER BEARING LOAD WITH REGARDS TO DURABILITY THEREOF USING FEM ANALYSIS

This paper deals with accurate geometric models of rolling bearing components in the CAD system. This model is then employed to create a static structural analysis used to determine the size of stress between the components of a rolling bearing. Following the stress analysis, we specify the maximum load of a rolling bearing with regards to durability thereof.

Keywords: roller bearing, maximum load, subsurface stress, von Mises stress, shear stress

1. Introduction

Numerical simulations of rolling bearings are currently predominantly based on the Hertz theory of contact stress of two objects, which is based on pressure calculation in areas of contact of rollers and raceways of bearing rings. This method, however, does not take into account the precise geometry of objects and their influence on stress distribution in rolling bearings. This article details a method permitting the creation of a realistic model of tapered roller bearing which will subsequently be used in a static structural analysis with the aim of determining the influence of operation process parameters under high load using the finite element method. A tapered roller bearing with inner diameter of 460 mm and 39 rolling elements was selected for the aforementioned analysis.

2. Creation of a 3D Virtual Model of Tapered Rolling Bearing

Pro/ENGINEER Wildfire, manufactured by PTC Corporation, was used to create the 3D virtual model of the tapered roller bearing. The bearing geometry was defined so as to reflect real-life production conditions, including all construction elements, such as concave roller, precise radii of profile curves, etc. This was necessary to assure the correct analysis of contact pressures and evaluate subsurface stress.

The distribution and magnitude of contact pressure depends on the geometrical shape of contact rollers. Rolling bearing manufacturers aim to optimize the shape of individual elements so as to assure optimal contact pressure and subsurface stress distribu-

tion. However, the manufacturers must also take into account limitations pertaining to the manufacturing process and technological possibilities. The manufacturing drawing defines the basic profile geometry and includes geometrical and shape tolerances reflecting the manufacturing process limitations. Fig. 1 shows a schematic view of the profile of the analyzed bearing with inner ring diameter d460, consisting of three circular arcs.

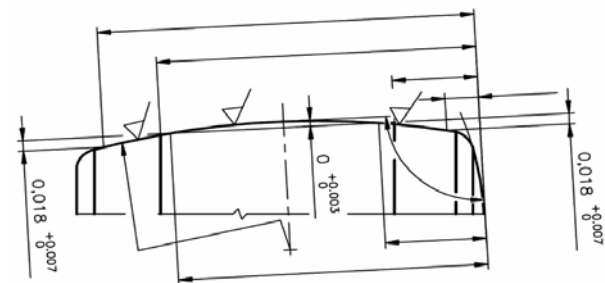


Fig. 1 Profile curve of d460 tapered roller bearing

Static structural analysis of the tapered roller bearing was performed using Ansys/Workbench, allowing the import of geometry from the Pro/ENGINEER system. The interconnection between Pro/ENGINEER and Ansys/Workbench is advantageous (Fig. 2), allowing for the modification of model geometry and position by changing relevant parameters. The Workbench environment retains the analysis definition (definition of border conditions, load forces, etc.) and whole post-processing process (evaluation of analysis results).

* Slavomir Hreck, Robert Kohar, Stefan Medvecký,

Faculty of Mechanical Engineering, University of Zilina, Slovakia, Email: slavomir.hreck@fstroj.uniza.sk

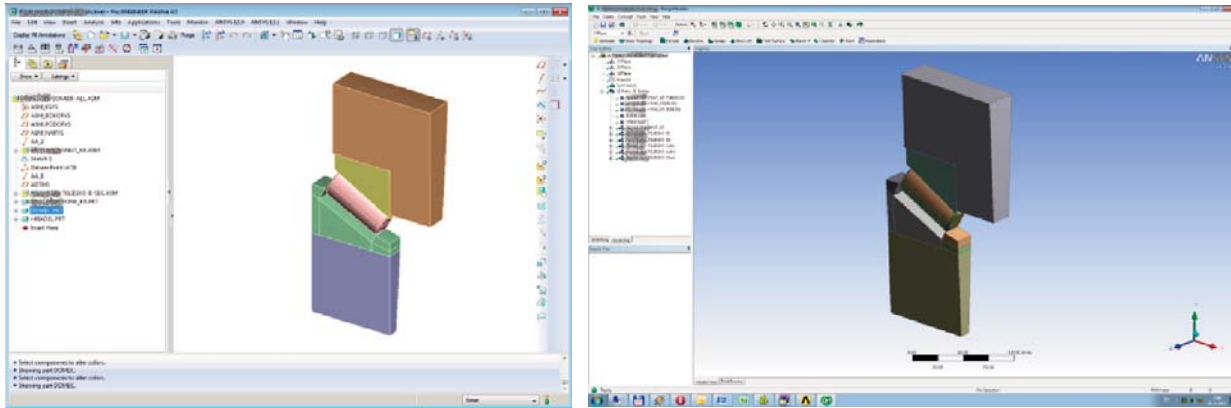


Fig. 2 Section of bearing model d460 constructed in CAD system ProENGINEER (left) and subsequently imported into CAE system Ansys/Workbench (right)

3. Definition of Static Analysis of Tapered Roller Bearing Using FEM in Ansys/workbench System

Choice of appropriate mesh element size is necessary in order to correctly analyze the contact pressure between the roller and roller raceway of outer and inner ring and analysis of subsurface stress. The FEM model mesh for contact pressure analysis should be defined by a minimum of 5 nodes per half width of contact area $b/2$. Mesh density along contact profiles was defined as 3 times the element size along the width of contact area in order to decrease the finite element model computational requirements. [1].

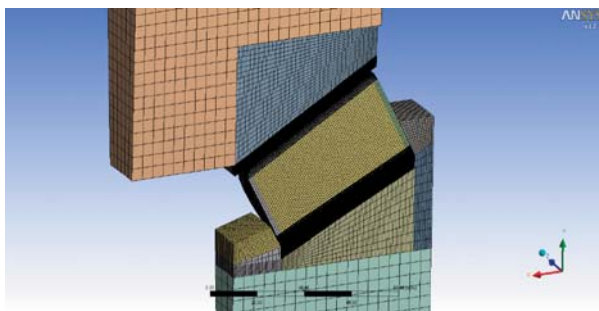


Fig. 3 FEM mesh of section of tapered roller bearing d460

Volume meshing of imported CAD geometry was performed in Ansys/Workbench using Solid185 element type (Fig. 3). Individual bearing elements are in contact because forces acting upon the bearing are transferred between rings (their raceways) and individual rollers. CONTA174 and TARGE170 element types were employed in Ansys/Workbench to define areas of contact between two rollers.

The tapered roller bearing d460 model was defined in half symmetry of one roller section ($360^\circ/39/2$) by two planes of symmetry defined via two coordinate systems with axis z perpendicular to the plane of symmetry.

Multiple contact types – connections between individual rollers were defined on the finite-element d460 bearing model. Areas between volumes, representing contact volumes of the roller with outer and inner ring, were defined as *Frictional* and the coefficient of friction was set to 0.1. The same contact type was defined between the face of the roller and inner ring support area [2]. Forces acting on the tapered roller bearing result in contact between the face of the roller and surface axial force components at inner bearing ring. Border conditions for the static analysis of d460 bearing were defined as follows:

- removal of one degree of freedom in direction of z axis in cylindrical coordinate system of the front surface of inner ring (axial force retention) – Fig. 4 – left,
- removal of one degree of freedom in direction of z axis in Cartesian coordinate system from the face of the roller due to roller stabilization (Fig. 4 middle).

Bearing load condition was simulated by applying axial force in the z axis direction (cylindrical coordinate system) onto the front area of housing (Fig. 4 right) and distributed into multiple load steps.

4. Static Analysis Results – Contact Pressure

The aim of this analysis was to determine the effect of load on the contact pressure at contact locations between the roller and inner and outer bearing ring. Distribution and magnitude of contact pressure depends on the geometrical shape of contact rollers. The analyzed tapered roller bearing d460 consists of rollers with a profile defined by three circular arcs. The dimensions of profile geometry include manufacturing tolerances since even cutting edge bearing manufacturing technologies are unable to deliver ideally precise geometry. Numerical simulations must therefore be conceived so as to take into account the said manufacturing tolerances.

Figs. 5 and 6 show the distribution of contact pressure at raceways of outer and inner ring of bearing d460 due to axial loading.

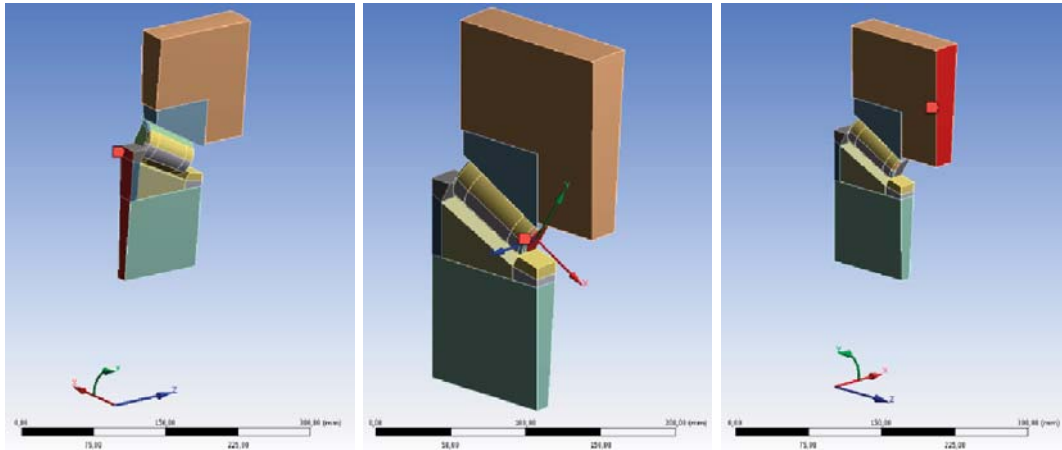


Fig. 4 Model of tapered roller bearing d460 with defined border conditions

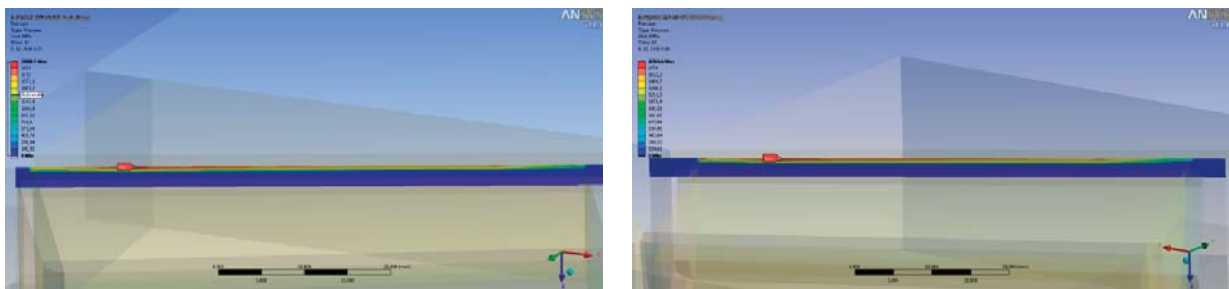


Fig. 5 Distribution of contact pressure at raceway of inner ring (left) and raceway of outer ring (right) - bearing d460

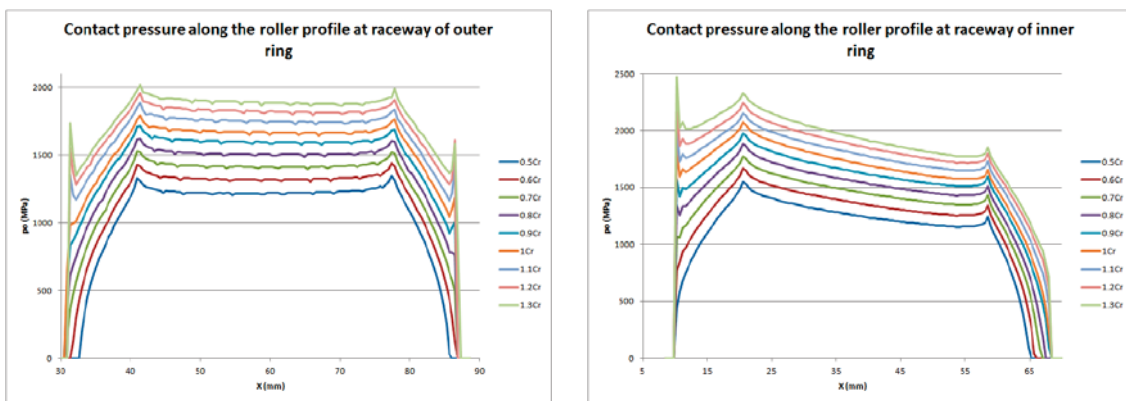


Fig. 6 Contact pressure along the roller profile at raceway of outer ring (left) and at raceway of inner ring (right) - bearing d460

The analysis result details the influence of load force size on the distribution of contact pressure and is presented graphically. For better representation, the value of contact pressure was subtracted from nodes of the finite element mesh in locations of maximum contact pressures at raceways of bearing rings, that is from points lying in the plane of symmetry ($z = 0$).

It is evident from Fig. 6 that the maximum contact pressure is present at contact locations between rollers and inner bearing ring.

Table 1 lists the maximum values of calculated contact pressures depending on applied load force.

When considering an equivalent load force higher than $P_e = 0.5 * C_r$, the ISO 281 standard imposes a loading limit in the rating life equation, because the said equation gives satisfactory results for a wide load force, however too high a load could result in undesirable plastic deformation of contact areas between rollers

Maximum values of contact stress at raceways of bearing rings

Table 1

	Contact pressure p_0 (MPa)								
	Pe=0.5Cr	Pe=0.6Cr	Pe=0.7Cr	Pe=0.8Cr	Pe=0.9Cr	Pe=1Cr	Pe=1.1Cr	Pe=1.2Cr	Pe=1.3Cr
outer ring	1347.8	1438.1	1525.3	1619.8	1716.6	1791.3	1882.7	1959.3	2017.2
inner ring	1548.1	1665.6	1776.2	1882.5	1976	2072.9	2155.7	2242.1	2473.4

and raceways of rings [3]. In view of the previous, it is necessary to conduct a detailed analysis of subsurface stress of rollers and bearing rings.

Radial bearings are often subjected to simultaneously acting radial and axial loads. If the resultant load is constant in magnitude and direction, the equivalent dynamic bearing load P can be obtained from the general equation

$$P_e = XF_r + YF_a$$

where P = equivalent dynamic bearing load [kN], F_r = actual radial bearing load [kN], F_a = actual axial bearing load [kN], X = radial load factor for the bearing, Y = axial load factor for the bearing.

5. Static Analysis Results - von Mises Stress

Numerous applications require the use of rolling bearings under load conditions exceeding 0.5 times the basic dynamic load capacity. However, a loading limit exists beyond which the rolling bearing might experience undesirable plastic deformations of raceways of bearing rings or rollers [3]. Criterion of equivalent stress or von Mises stress is used to ascertain whether the yield point (plastic deformation) has been reached due to excess stress.

Fig. 7 shows the von Mises stress distribution in areas of contact between the roller and raceways of rings of bearing d460.

The magnitude of subsurface von Mises stress is different along the line contact of two different rollers and depends on the mag-

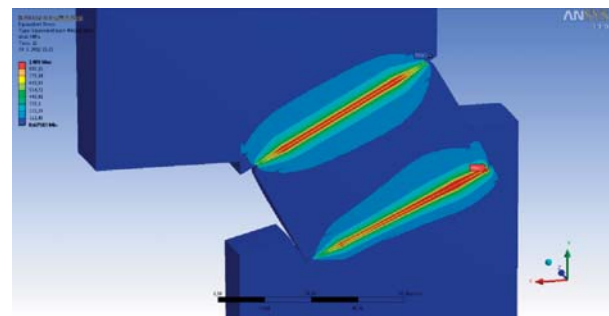


Fig. 7 Von Mises stress distribution along the profile of tapered roller bearing d460

nitude of contact stress between the said rollers in contact (Fig. 8). The performed analysis showed that maximum von Mises stress is located in the plane of symmetry at a depth of 0.446 mm under the surface. Paths were defined along the said depth and von Mises stress was evaluated.

Von Mises stress maxima along the roller profile are located at profile curve discontinuities. Additional paths were defined in the symmetry plane, normal to the axis of the roller, to achieve true analysis of the von Mises maxima (Fig. 9) due to different depths under the surface (wherein these are present) along the roller profile. The necessary case depth at raceways of bearing rings and rollers is determined based on the mentioned stress analysis and stress is evaluated at the boundary plane of base bearing material and case depth.

Table 2 lists maximum von Mises stress values calculated for tapered roller bearing d460 depending on the applied loading force.

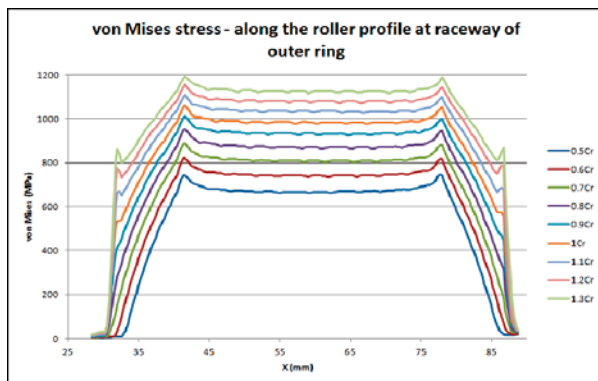


Fig. 8 Dependence of von Mises stress (outer ring left, inner ring right) on equivalent bearing load

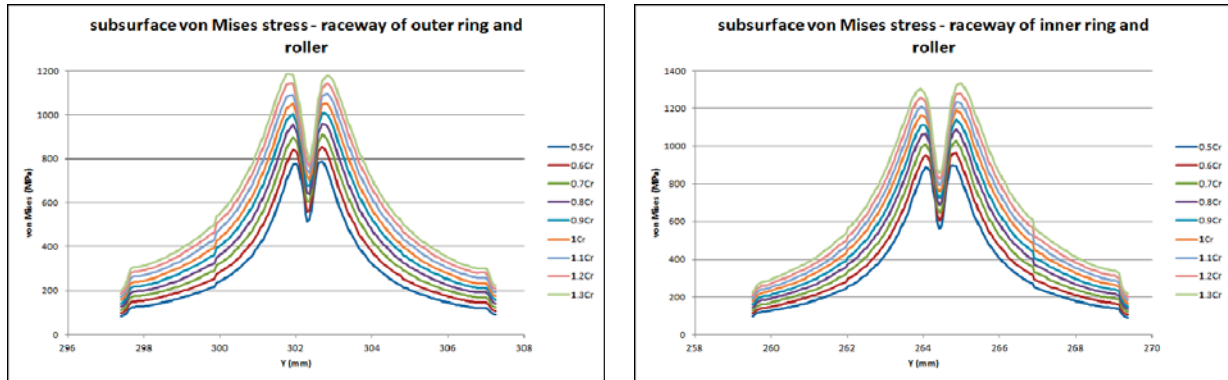


Fig. 9 Dependence of subsurface von Mises stress (outer ring – roller left, inner ring-roller right) on equivalent bearing load

Maximum equivalent von Mises stress based on applied bearing load

Table 2

	vonMises Stress σ_{vonM} (MPa)								
	Pe=0.5Cr	Pe=0.6Cr	Pe=0.7Cr	Pe=0.8Cr	Pe=0.9Cr	Pe=1Cr	Pe=1.1Cr	Pe=1.2Cr	Pe=1.3Cr
outer ring	790.03	854.79	909.24	960.47	1007.8	1050.6	1096.7	1140.3	1180.2
roller-outer ring	776.41	840.01	898.93	954.96	1005.3	1048.2	1091	1139.8	1186.4
roller-inner ring	897.96	965.88	1030.4	1091.1	1141.7	1190.6	1233.2	1281.1	1331.8
inner ring	889.66	952.33	1010	1064.3	1112.6	1164.6	1209.1	1258.3	1306.8

6. Static Analysis Results – Shear Stress τ_{yz}

Hertz equations are predominantly used to analyze contact stress, taking into account static pressure loading of contact areas. However, most machine components are moving and their contact areas are sliding or have a tendency to do so. Sliding causes frictional forces which in turn cause shear stress at contact areas, in addition to normal pressure load. This results in a complex stress state around the contact areas.

Insufficient analysis of contact stress could lead to erroneous design of machine components, causing component failure due to

premature material surface fatigue. This type of damage is most commonly characterized by pitting, crumbling or flaking and disrupts the machine workflow and introduces additional stress, which can result in fractures [1].

Material fatigue in rolling bearings usually manifests itself as pitting, observed at rollers or raceways of bearing rings. Pitting subsequently causes shear stress due to frictional forces between contact areas. Fatigue lifetime of rolling bearings can be determined by analyzing shear stress (based on Wohler curves or S-N material curves). Combined analysis of contact pressure, subsurface von

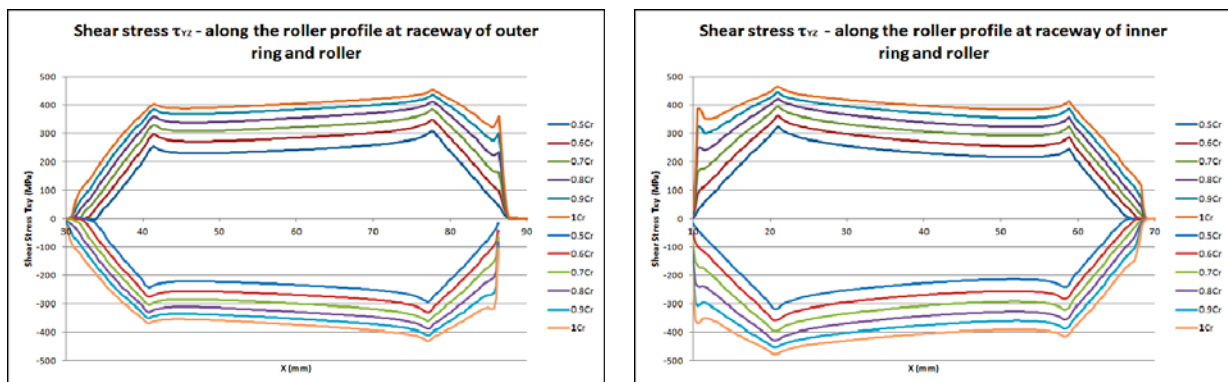


Fig. 10 Distribution of shear stress τ_{yz} located in contact areas between the roller and outer ring (left) and inner ring (right) depended on equivalent bearing load

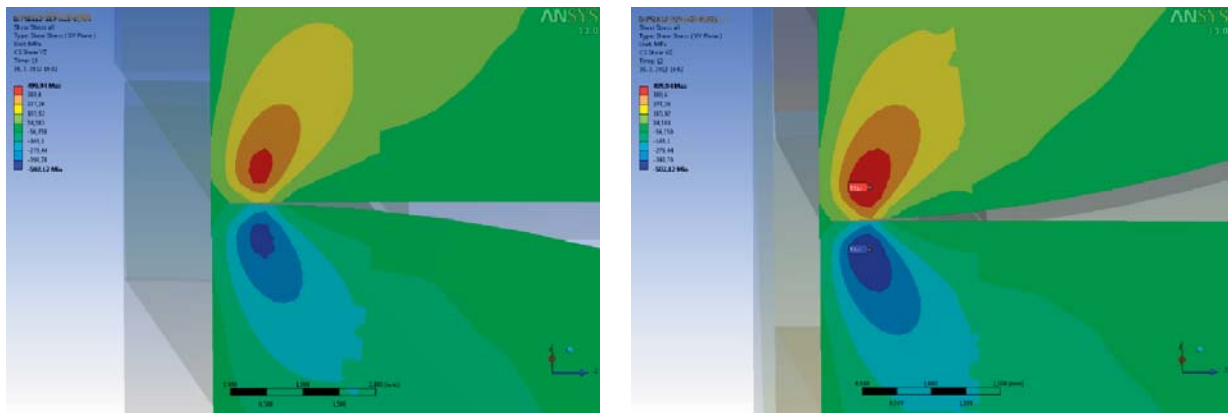


Fig. 11 Distribution of shear stress τ_{yz} at contact point outer ring - roller (left) and inner ring - roller (right)

Dependence of shear stress of tapered roller bearing d460 on loading force

Table 3

	Shear Stress τ_{yz} (MPa)								
	Pe=0.5Cr	Pe=0.6Cr	Pe=0.7Cr	Pe=0.8Cr	Pe=0.9Cr	Pe=1Cr	Pe=1.1Cr	Pe=1.2Cr	Pe=1.3Cr
outer ring	292.49	315.95	344.99	371.63	391.56	406.29	423.41	446.85	466.53
roller-outer ring	-295.97	-314.67	-344.72	-371.88	-390.98	-405.17	-428.71	-454.29	-474.67
roller-inner ring	347.87	371.85	406.96	435.65	454.44	472.85	499.94	528.25	552
inner ring	-343.42	-375.67	-408.97	-438	-458.36	-475.55	-502.12	-529.8	-551.43

Mises stress and shear stress portrays the complex stress state in contact areas between the rollers and bearing rings.

We analyzed and evaluated shear stress in planes of maximum shear stress [1]. The said planes are perpendicular to the cylinder axis for the contact pair cylinder-cylinder and perpendicular to roller axis in case of rolling bearings with line contact. Fig. 10 shows the distribution of subsurface shear stress located in contact areas between the roller and outer and inner bearing d460 ring. Shear stresses creating two symmetric pairs have approximately the same magnitude and opposite signs. Their maxima are located under the surface and offset from plane of symmetry (Fig. 11).

When the roller was in contact with the outer ring, shear stress maxima were located at a depth of 0.36 mm under the surface and 0.6 mm from the plane of symmetry. When the roller was in contact with inner ring, maxima were located at a depth of 0.35 mm under the surface and 0.61 mm away from the plane of symmetry.

Fig. 10 shows the dependence of two shear stresses on magnitude of equivalent load along the roller profile. Shear stress curves mimic the distribution of contact pressures along the profile in contact areas between the roller and bearing rings and maxima are located in discontinuities of the roller profile curve.

Table 3 lists maximum values of shear stresses depending on the magnitude of equivalent loading of bearing d460. Shear stress analysis showed that maximum shear stress is present at contact area between roller and inner bearing ring.

7. Load-bearing Capacity

Rolling bearings and their components can be subjected to load stress until reaching a point where external loading forces cause plasticity or permanent deformation. The total loading capacity of rolling bearings depends on the geometry of individual components, the material used, chemical and thermal treatment and distribution of subsurface stress. In order to determine the maximum loading capacity of rolling bearings using FEM analysis, we must employ non-linear material models for individual bearing components. Because raceways of bearing rings and the surface of rollers are hardened, when compared to cores of bearing components, it is necessary to use various material models reflecting the bearing material parameters after chemical and thermal treatment. In our FEM model of tapered roller bearing d460, we used *Bilinear Isotropic Hardening* material model, defined by Young modulus, Poisson number, yield point and tangent modulus. Table 4 lists values of materials models for bearing steel OVAKO 100Cr6. The material model for hardness 58HRC corresponds to the resulting martensitic steel structure after hardening.

Material hardness model for steel 58HRC was been used for elements of raceways of bearing rings and surface of roller depth 2X mm. Cores of bearing components were modeled using mode 30HRC based on production technology of the tapered roller bearing d460.

Maximum equivalent load force $P_e = 1.5 * C_r$, was applied to the tapered roller bearing d460 model with the aim of determining

Values of materials models Bilinear Isotropic Hardening for bearing FEM model Table 4

	Hardness	E	μ	Re	Etan
	HRC	MPa	–	MPa	MPa
core	30	210 000	0.3	750	3 264
raceway	58	210 000	0.3	1700	14 287

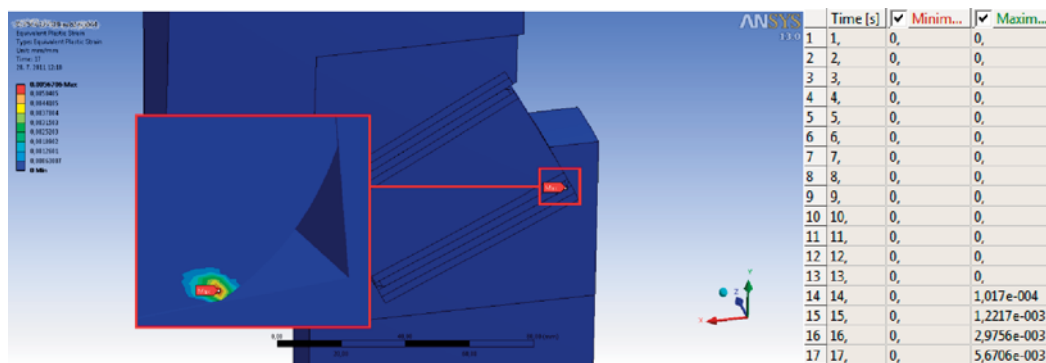


Fig. 12 Distribution and magnitude of Equivalent Plastic Strain of tapered roller bearing d460 for various bearing loads

the maximum permissible loadforce without permanent deformation of the bearing. Equivalent Plastic Strain (EPS) was evaluated post-analysis and we determined that the maximum loadforce of the tapered roller bearing under given boundary conditions is up to an equivalent load force $P_e = 1.1 * C_r$, beyond which plasticity of bearing components occurs (Fig. 12). Right hand side of the table lists EPS values (mm/mm) for different loading values of tapered roller bearing d460.

The subsequent chapters detail the analysis of surface and subsurface stress of the FEM model of tapered roller bearing d460 depending on the applied loadforce. Based on evaluation of various stress types, we can predict the projected service life-time of a given rolling bearing under certain boundary conditions and optimize construction thereof in view of extending the service life-time.

8. Conclusion

The aim of this article was to detail a method allowing the stress analysis of rolling bearings under equivalent loads higher

than 0.5 times the basic dynamic load capacity. Based on this analysis we can determine the maximum load the bearing can repeatedly endure. Stress distribution analysis, coupled with knowledge of operating conditions, inner construction of the bearing and load conditions can help predict the service life-time of the rolling bearing and can subsequently be used to optimize construction thereof.

This work was supported by the Slovak Research and Development Agency under the contract No. APVV-0087-10 - Intelligent Diagnostic Systems of Gearboxes and their Components.

This work was supported by the Slovak Research and Development Agency under the contract No. APVV-0419-11 - Adaptation of modern computer-simulation methods to the development of rolling bearings and their verification in real conditions.

References

[1] CASTLEBERRY, G.A.: AnalyzingContactStresses More Accurately. In: *Machine Design*, 1984.
 [2] JEDRZEJEWSKI, J., KWASNY, W.: Modelling ofAngularContactBallBearings and AxialDisplacementsforHigh-Speed Spindles, *Tribology International*, vol. 45, No. 1, 2012, pp. 8-15.
 [3] ISO 281 RollingBearings - DynamicLoadRatings and Rating Life, 2007.

Robert Kohar – Slavomir Hreck – Stefan Medvecký *

USAGE OF DYNAMIC ANALYSIS TO DETERMINE FORCE INTERACTIONS BETWEEN COMPONENTS OF ROLLING BEARINGS

The aim of this paper is to detail the creation of a roller bearing model in the Adams program suite for subsequent dynamic analysis and to obtain information about different parts of the bearing during the simulation. The bearing model was made so as to closely resemble its real-life counterpart, which allows us to estimate load conditions, dynamic conditions of individual bearing parts and interactions between them.

1. Introduction

This article details the creation of a virtual bearing model allowing the analysis of individual bearing components under dynamic behavior. Two models of tapered roller bearings will be employed: one with steel cage and the other with plastic cage, both of which are pictured in Fig. 1 along with the assembled bearing model.

2. Tapered roller bearing model

Dynamic simulations of the tapered roller bearing were performed in the MSC.Adams system. A precise geometrical model of the bearing was necessary in order to perform the said simulations. The 3D model was created based on available drawing docu-

mentation and incorporates various methods with regards to the overall model complexity. Model design was performed in Pro/Engineer Wildfire 5 (Fig. 1), which, when compared to the MSC.Adams environment, allows simpler model creation and subsequently easier bearing geometry modifications. The bearing model assembly was transformed from Pro/Engineer into Adams environment using the Parasolid file format and was further processed based on analysis requirements. The first step included material definition for individual bearing components. The bearing consists of inner and outer ring, cage and rollers. Table 1 lists values assigned to individual parts.

In the next step we defined the contacts between individual bearing components. Contact type “solid to solid” was chosen for the afore mentioned operation, defining two objects coming into contact. This was due to the geometrical complexity of the model



Fig. 1 Tapered roller bearing model in Pro/Engineer

* Robert Kohar, Slavomir Hreck, Stefan Medvecký
Faculty of Mechanical Engineering, University of Zilina, Slovakia, E-mail: robert.kohar@fstroj.uniza.sk

Material properties of individual bearing parts Table 1

	Density (kg.m ⁻³)	Young modulus (MPa)	Poisson constant (-)
Inner ring	7850	202000	0.29
Outer ring	7850	202000	0.29
Roller	7850	202000	0.29
Steel cage	7850	202000	0.29
Plastic cage	1100	3000	0.42

and inability to determine all bearing parts that come into contact. This contact type requires the definition of the following parameters to define the normal force which is based on an impact using the "Impact" function [1]: Stiffness, Exponent, Max Damping and Penetration Distance. Contact pairs were formed between inner ring and rollers, outer ring and rollers and between ring and rollers. Parameter values for contact between cage and rollers were defined as per [1]. Parameter values for contacts of rollers with outer and inner ring were defined based on the Hertz theory of contact pressure for tapered roller bearing. Table 2 lists values of parameters for individual contacts. We also considered a friction model based on Coulomb friction force calculation. Values of static and dynamic friction coefficient were set according to [2] and values of transmission velocity according to [1] which are generalized values for the model with friction effects at the contact locations using Coulomb friction model in Adams.

Contact parameters used in the tapered roller bearing model Table2

Parameter	Contact pairs			
	Roller - outer ring	Roller - inner ring	Roller - cage	
			steel	Plastic
Stiffness (N.mm ⁻¹)	9870000	9870000	100000	80000
Exponent (-)	1.5	1.5	1.5	1.8
Max. Damping (N.s.mm ⁻¹)	10000	10000	100	
Penetration Distance (mm)	0.15	0.15	0.1	
Static coefficient (-)	0.12	0.12	0.12	0.1
Dynamic coefficient (-)	0.1	0.1	0.1	0.06
Stiction transition velocity (mm.s ⁻¹)	100	100	100	
Friction transition velocity (mm.s ⁻¹)	1000	1000	1000	

Next we defined the geometric and kinematic constraint conditions and load force. Axial load force of the outer ring was associated with "Fixed joint" constraint, which resulted in removal of all degrees of freedom. The inner ring was associated with "Cylindrical Joint" constraint condition, which allowed rotation and translation along the x axis. "Rotational Joint Motion" of type "Velocity" was assigned to the "Cylindrical Joint" constraint, allowing rotational

movement. This movement was defined via the STEP function [1] and corresponds to bearing rotational speed $n = 15.5 \text{ min}^{-1}$. Loading force was defined via gravitation acceleration "Gravity" and "Axial Force" of magnitude 518000 N in x axis direction, influencing the inner ring. Figure 2 left shows a model with axial load force with defined geometrical and kinematic constraint conditions.

Constraint conditions for dynamic analysis with radial load force were defined as following: "Revolute Joint" was assigned to the inner ring and allowed inner ring rotation around the x axis. "Translational Joint" was assigned to the outer ring, allowing movement in direction of the y axis. "Rotational Joint Motion" of type "Velocity" was assigned to the aforementioned constraint, allowing rotational movement. This movement was defined in a similar fashion as described above using the STEP function. Loadforce was defined via gravitation acceleration "Gravity" and "Radial Force" of magnitude 4500000 N was applied in y axis direction, influencing the outer ring. Figure 2 right shows the model under radial load force with defined geometric and kinematic constraint conditions.

After defining all constraint conditions, boundary conditions and loadforce, we defined the analysis type and solved parameters as follows:

SIMULATE/DYNAMIC, END = 30, STEPS = 3000

Integrator GSTIFF, Formulation SI2, Corrector Modified, Error 1e-2, Executable External C++, Thread Count 8, Contacts Default Library, Faceting Tolerance 1e5.

3. Dynamic simulation results - axial load force

Dynamic simulation results with axial load force represent force interactions between individual bearing parts, movement of bearing cage center of gravity and angular velocity thereof. Figure 3 shows forces between roller and cage, roller and inner ring and angular velocity of this roller. Maximum force between steel cage and rollers was observed during interaction of the cage with roller n.26 and is equal to 268 N (Fig. 3 up, green line). Also shown is the force between inner ring and roller n. 26 (red line), which varied between 54297 N and 59103 N, a difference of 4.2% (minimal force) and 8.1% (maximal force) when compared to theoretical calculations. The blue line displays angular velocity of roller n. 26 and varies between 483°/s and 495°/s.

Maximum force between plastic cage and rollers was observed during interaction of the cage with roller n.2 and is equal to 251N (Fig. 3 down, green line). Also shown is the force between inner ring and roller n. 2 (red line), which varied between 54467 N and 58636 N and was lower when compared to the steel cage, representing a difference of 3.9% (minimal force) and 7.1% (maximal force) when compared to theoretical calculations. The blue line displays angular velocity of roller n. 2 and varies between 483°/s and 495°/s, similar to the velocity observed for the steel cage.

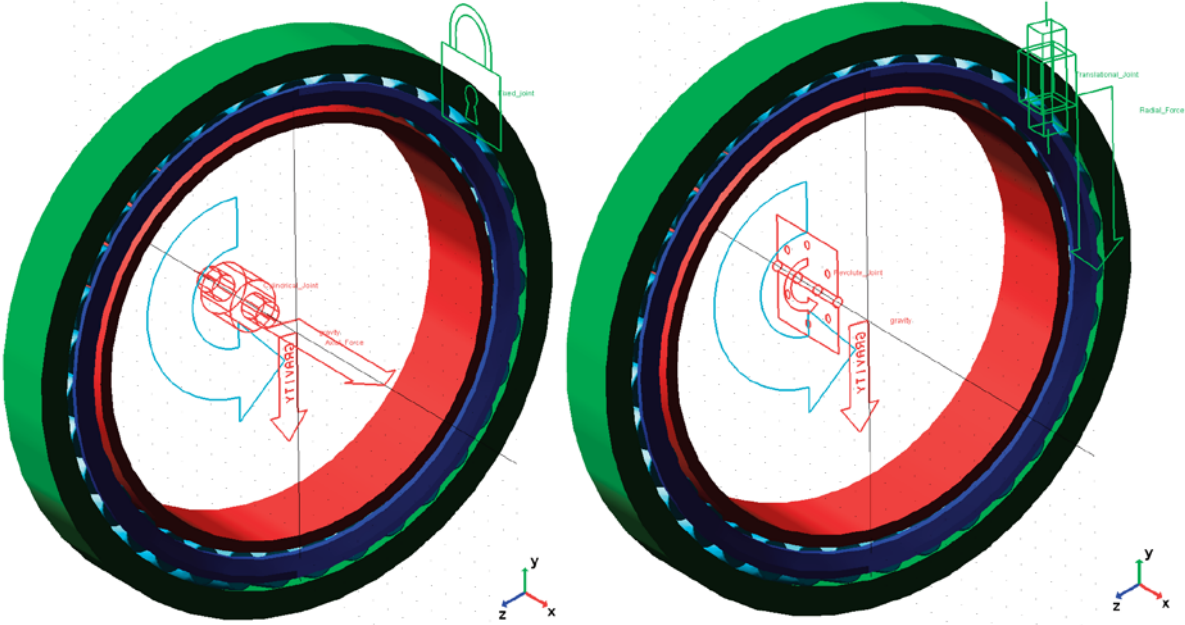


Fig. 2 Definition of geometric and kinematic constraint conditions - axial load force - left, radial load force - right

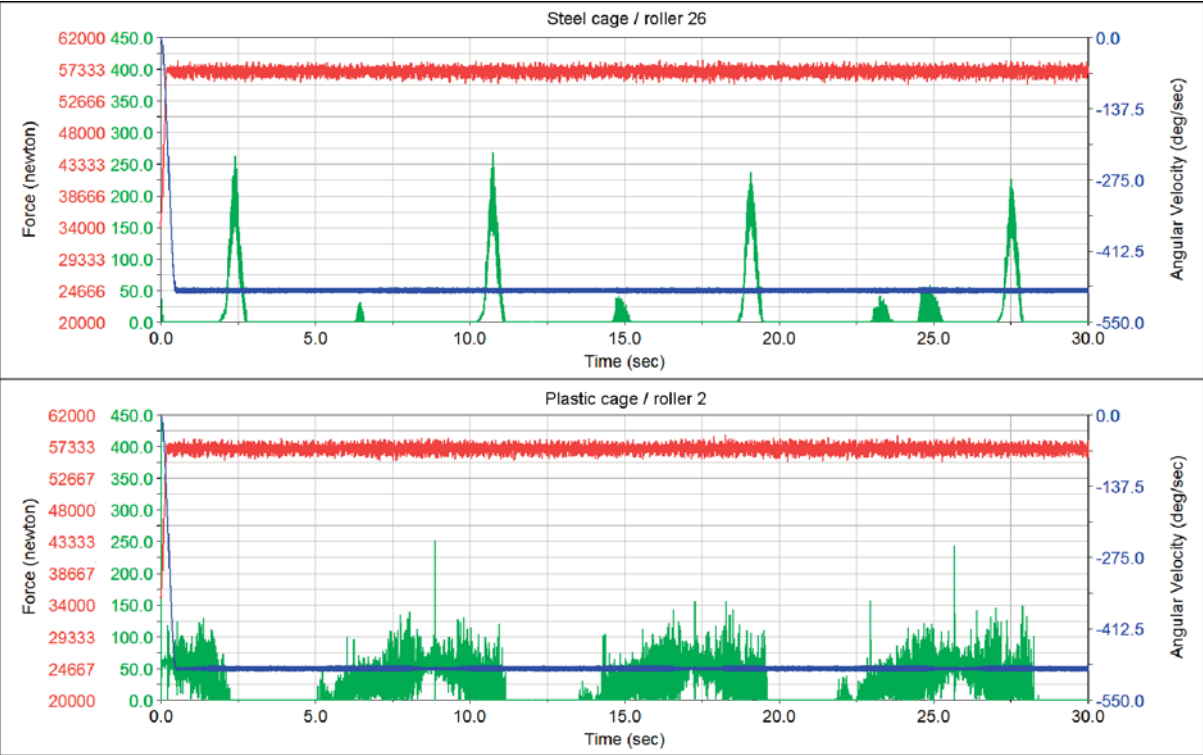


Fig. 3 Force interaction between inner ring and rollers (red lines), force interaction between cage and rollers (green lines) and angular velocity of rollers.

Figure 4 left shows the movement of steel cage center of gravity in x, y and z axes oriented as per Fig. 2. It is evident that minimum change of center of gravity is within the rotation axis (x axis, up to 0.007 mm) and maximum change in the $y-z$ plane, wherein the deviation in the y axis is equal to 0.419 mm and in z axis up to 0.649 mm.

Figure 4 right shows the movement of plastic cage center of gravity. It is evident that the center of gravity deviation increased within the rotation axis (x axis) to 0.605mm when compared to the steel cage and also increased in the $y-z$ plane, wherein the deviation in the y axis was equal to 0.599 mm and 0.919 mm for the z axis. Figure 4 down shows the center of gravity location in the $y-z$ plane.

4. Dynamic simulation results – radial load force

Similar to axial load force, we calculated force interactions between individual bearing parts, movement of bearing cage and angular velocity thereof when subjected to radial force. Figure 5 shows force between roller and cage, roller and inner ring and angular velocity of the roller. Also shown is the force between inner ring and roller n.13 (red line). Maximum force between steel cage and rollers was observed for roller n.13 and is equal to 706N (green line). The analysis also showed that highest load rates are present at rollers 10 to 14 during start-up time (2-5 seconds) and are equal to 700N. During subsequent simulation time, the cage was in contact with rollers only when the rollers were off-loaded

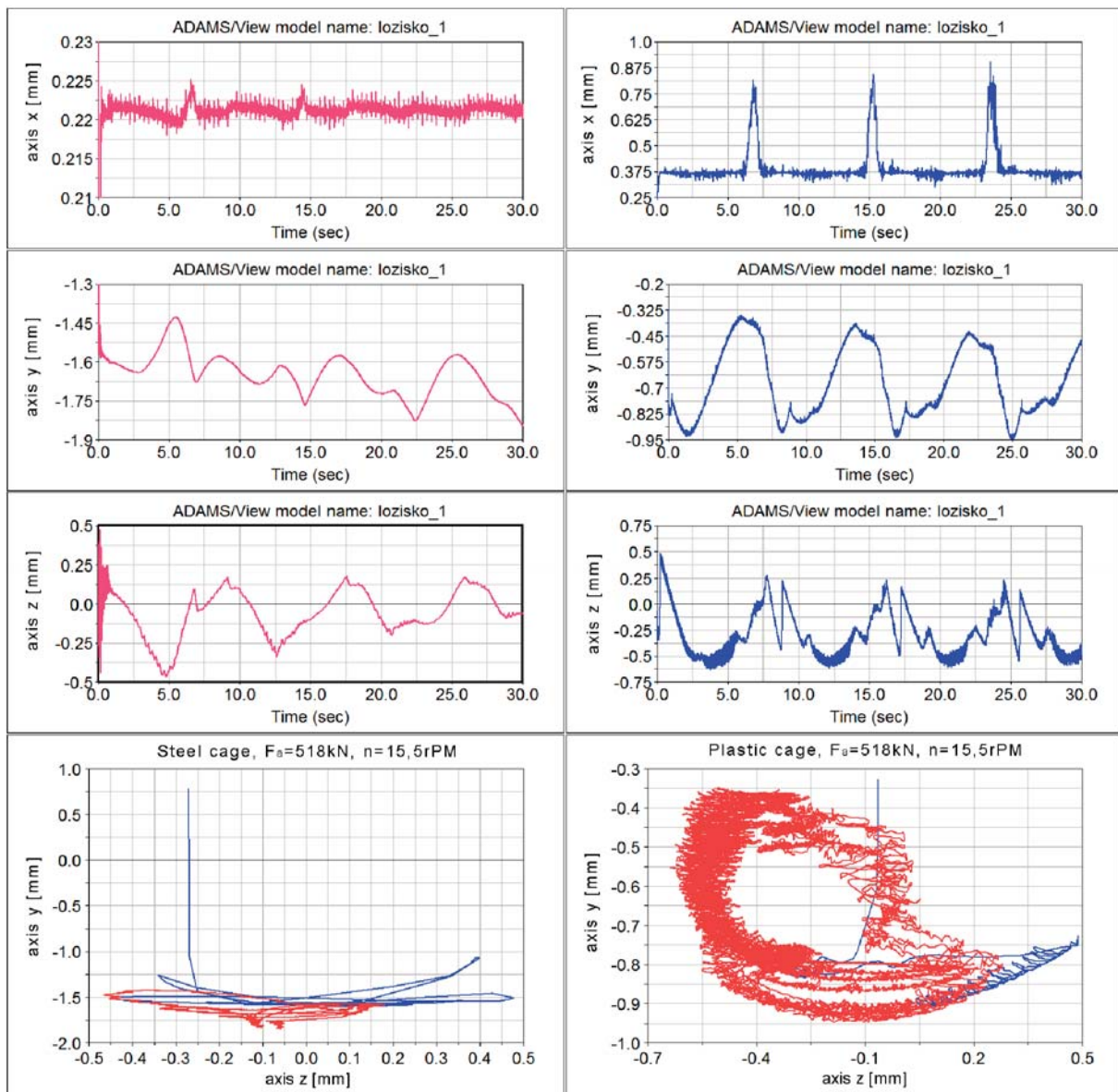


Fig. 4 Movement of center of gravity of steel and plastic cages in the $y-z$ plane, axial load force

and maximum force value was equal to 250N. Angular speed was constant (489°/s) under applied roller load and lowered under roller load in the 20000N to 70000N range, achieving a minimum value of 445°/s (blue curve).

Figure 5 down shows force between inner ring and roller n.10 (red line) for bearing with plastic cage. Maximum force between plastic cage and rollers was observed for roller n.13 and is equal to 706N (green line). Maximum force between the plastic cage and rollers was observed for roller n.10 and is equal to 670N (green line). Similar to the steel cage, highest load rates were present at rollers 10 to 14 during start-up time (2-5 seconds) and are equal to 700 N. When compared to the steel cage, the rollers were in contact not only in the off-load phase (force equal to 100 N) but also during the load phase, with the force equal to 400 N. Angular speed was constant (489°/s) under applied roller load and, similar to the steel cage, lowered under roller load in the 20000N to 70000N range, achieving a minimum value of 167°/s (blue curve) and 320°/s under load.

Figure 6 left shows the movement of steel cage center of gravity in *x*, *y* and *z* axes oriented as per Fig. 2. The change of center of gravity within the rotation axis (*x* axis) is equal to 0.026 mm and maximum change is in the *y-z* plane, wherein the deviation in the *y* axis is up to 0.433 mm and in the *z* axis up to 0.711 mm. Figure 6 right shows the movement of plastic cage center of gravity. It is evident that the center of gravity deviation in the rotation axis (*x*

axis) is similar that of the steel cage (0.605mm), however decreased in the *y-z* plane, wherein the deviation in the *y* axis was 0.345 mm and 0.575 mm for the *z* axis. Figure 6 down shows the center of gravity location of the cages in the *y-z* plane.

5. Conclusion

The aim of this article was to detail the creation of a tapered roller bearing model in the Adams software suite to be used for further dynamic analysis and to obtain information about individual parts during the simulation process. The bearing model was made so as to closely resemble its real-life counterpart and thus allowed us to extract information about load transfer conditions, kinematic ratios and mutual component interactions. This approach can help identify problematic parts during the development phase and allows modification of the bearing design before the actual manufacturing process, thus maximizing the overall service life-time of the bearing.

This work was supported by the Slovak Research and Development Agency under the contract No. APVV-0087-10 – Intelligent Diagnostic Systems of Gearboxes and their Components.

This work was supported by the Slovak Research and Development Agency under the contract No. APVV-0419-11 – Adaptation of modern computer-simulation methods to the development of rolling bearings and their verification in real conditions.

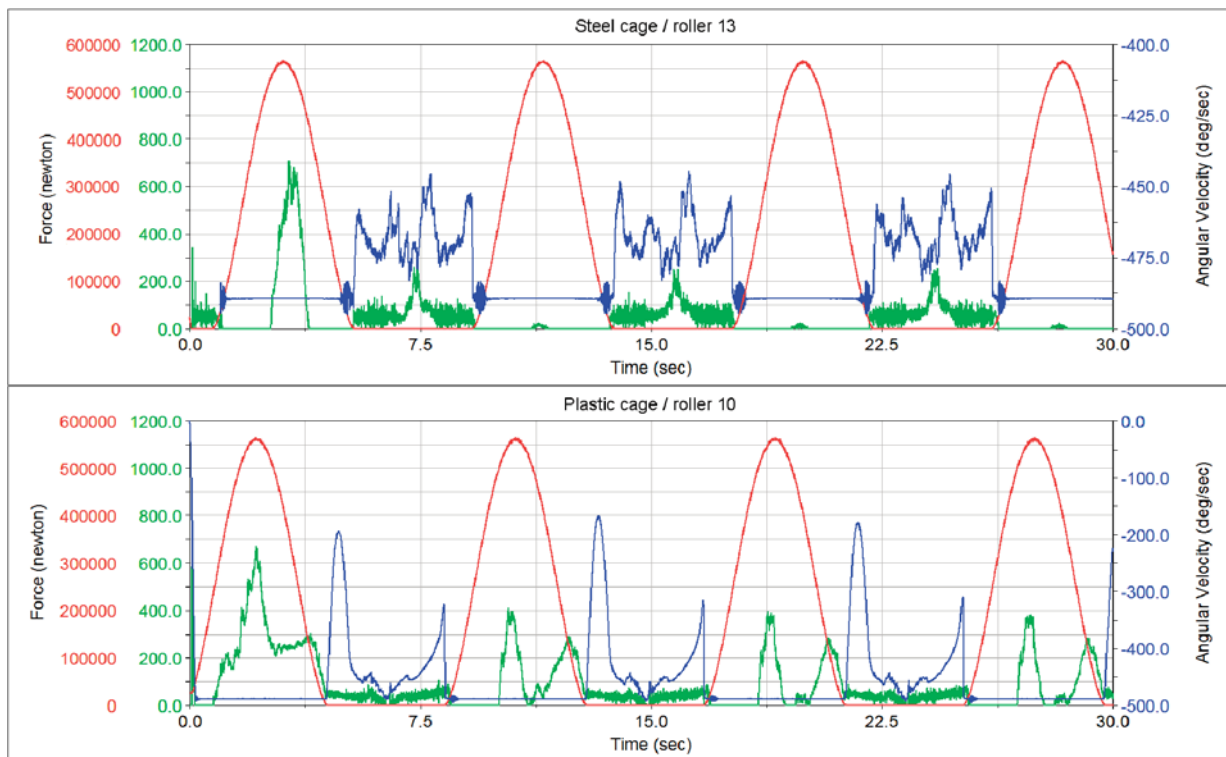


Fig. 5 Force interaction between inner ring and rollers (red lines), force interaction between cage and rollers (green lines), angular velocity of rollers (blue line)

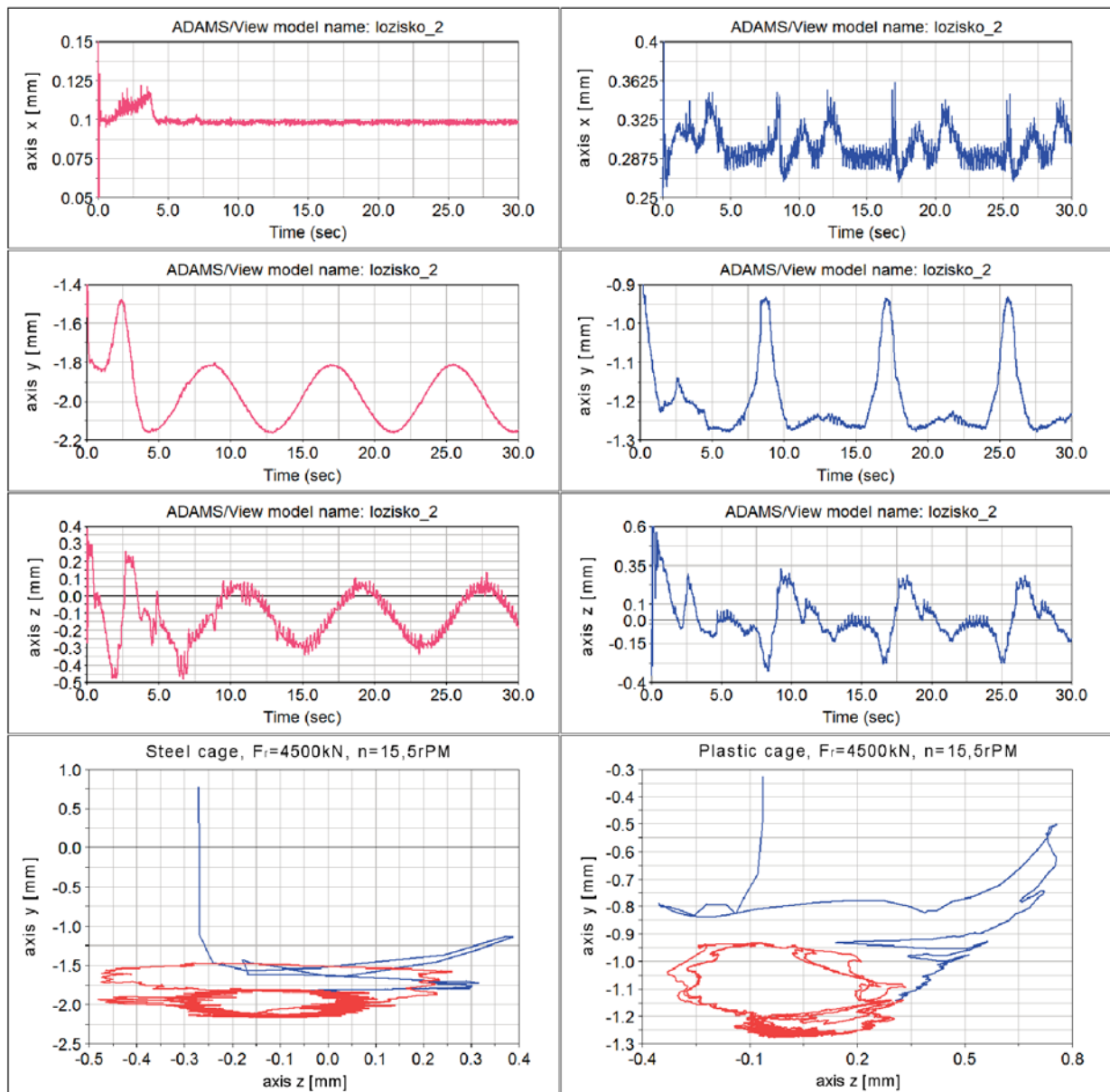


Fig. 6 Movement of center of gravity of cages in the y-z plane under axial load

References:

- [1] MD Adams 2011 Online Help.
- [2] HARRIS, T. A., KOTZALAS, M. N.: *Essential Concepts of Bearing Technology*. 5. edition. 2007.

THE EFFECT OF METRIC SPACE ON THE RESULTS OF GRAPH BASED COLOUR IMAGE SEGMENTATION

This paper deals with the impact of the metric space on the results of colour image segmentation algorithm. Distance and similarity measures are important tasks for quality of colour image segmentation. Main idea of this research is to make a comparison of algorithm results with using different metrics. Euclidean distance is the most used metric in many colour image segmentation algorithms. This paper shows comparison of this metric with many other metrics. Nine different metrics are gradually used in efficient graph based colour image segmentation algorithm created in the C++ language. The efficiency of precision and recall is one of the investigation tasks of colour image segmentation.

Keywords: image, segmentation, metric, distance, similarity

1. Introduction

Colour image segmentation is an important process in image analysis and processing. The main idea of this process is dividing the representation of image into spatially coherent regions that cover entire image. Image segmentation is fundamental problem in the image analysis. There is problem to find a fast, simple, automatic, robust algorithm that will be efficiently segment varied types of images [1], [2].

In the last decades, some colour image segmentation algorithms have been developed and improved. The algorithms used for colour image segmentation can be divided into next groups: algorithms based on Markov random field [3], graph based algorithms [4], algorithms based on neural networks [5], algorithms based on mean shift [6], clustering algorithms [7], algorithms with using colour histograms [8], region growing algorithms [9], and finally fuzzy algorithms [10]. Most of those algorithms used Euclidean distance to computing dissimilarity between pixels in the image. The goal of this paper is to compare this distance with other ten distances and find the best metric as a best solution for the algorithm.

This paper is organized as follows: Section 1 is Introduction, Section 2 presents the efficient graph based algorithm. In Section 3, metric space is described. Experiments and experimental results are presented in Section 4. Finally, Section 5 introduces the conclusion and suggestions for future works.

2. The efficient graph based algorithm

The efficient graph based algorithm presented in [11] deals with problem in terms of a graph $G = (V, E)$ where nodes $v_i \in V$

represent pixels in the image, and the edges $(v_i, v_j) \in E$ connect certain pairs of neighbouring nodes. Each edge (v_i, v_j) has corresponding weight $w(v_i, v_j)$ that is nonnegative dissimilarity measure between connected nodes by the edge (e.g. the difference in colour, location, intensity, motion, etc). There are several techniques to correct pixels merging. One of most popular is merging pixels via their similarity or dissimilarity. Thus, edges between two vertices in the same segment should have low weights and high weights for edges between two vertices in different segments [11].

Efficient graph based algorithm has two important tasks, namely, definition of difference between two components or segments and the definition of threshold function. In the first step each segment contains one pixel only. In the next step, segments are iterative merged by the following conditions:

$$Diff(C_1, C_2) \leq Int(C_1) + T(C_1), \quad (1)$$

$$Diff(C_1, C_2) \leq Int(C_2) + T(C_2), \quad (2)$$

where $Diff(C_1, C_2)$ is difference between C_1 and C_2 components, $Int(C_1)$ and $Int(C_2)$ are internal differences of C_1 and C_2 components, $T(C_1)$ and $T(C_2)$ are threshold functions of C_1 and C_2 components [11].

The threshold function controls the level of two segments merging, where in order to boundary detection the difference between two segments must be bigger than their internal difference. Threshold function is defined as follows:

$$T(C) = \frac{k}{|C|}, \quad (3)$$

* Martina Zachariasova, Robert Hudec, Miroslav Benco, Patrik Kamencay, Peter Lukac, Slavomir Matuska
Department of Telecommunications, University of Zilina, Slovakia, E-mail: martina.zachariasova@fel.uniza.sk

where $|C|$ presents the size of component C , k parameter is constant, which manages size of the components. For small segments, stronger evidence of a boundary is required. Larger k causes a preference for larger segments, smaller segments are allowed when there is a sufficiently large difference between them [11].

3. Metric space

In computer vision, colour image segmentation is process of partitioning image into multiple segments. The main form how to find object and boundaries in the image is by using efficient graph based algorithm. For computing differences between the pixels or segment, dissimilarity metric is used. The most used metric to measure difference between pixels is Euclidean distance. In this chapter, Euclidean distance and other metrics will be introduced.

Euclidean distance represents shortest distance between two vectors in Cartesian coordinate system. This distance examines the root of square of absolute value of differences between coordinates of a pair of objects (pixels or segments in image segmentation). Euclidean distance is the most common use of distances and is given as [12]:

$$d_{Eucl} = \sqrt{\sum_i |x_i - y_i|^2}, \tag{4}$$

where x_i and y_i are elements of vectors.

Nine different distances are compared in this paper. All the equations that compute those distances are shown in next equations [13] - [15]:

- Bray Curtis distance (*BrCu*)

$$d_{BrCu} = \frac{\sum_i |x_i - y_i|}{\sum_i (x_i + y_i)}, \tag{5}$$

- Canberra distance (*Canb*)

$$d_{Canb} = \sum_i \frac{|x_i - y_i|}{x_i + y_i}, \tag{6}$$

- Clark distance (*Clar*)

$$d_{Clar} = \sqrt{\left(\sum_i \frac{|x_i - y_i|}{x_i + y_i}\right)^2}, \tag{7}$$

- Euclidean distance (*Eucl*)

$$d_{Eucl} = \sqrt{\sum_i |x_i - y_i|^2}, \tag{8}$$

- Hamming distance (*Hamm*)

$$d_{Hamm} = \sum_i (x_i - y_i)^2, \tag{9}$$

- Jaccard distance (*Jacc*)

$$d_{Jacc} = \frac{\sum_i (x_i - y_i)^2}{\sum_i x_i^2 + \sum_i y_i^2 + \sum_i x_i y_i}, \tag{10}$$

- Lorentzian distance (*Lore*)

$$d_{Lore} = \sum_i \ln(1 + |x_i - y_i|), \tag{11}$$

- Manhattan distance (*Manh*)

$$d_{Manh} = \sum_i |x_i - y_i|, \tag{12}$$

- Minkowski distance (*Minp*)

$$d_{Minp} = \sqrt[p]{\sum_i |x_i - y_i|^p}. \tag{13}$$

4. Evaluation criterion

With the increase in the number of developed algorithms for image segmentation, evaluation criterion for studying of segmentation is required.

The criterion used for comparing image segmentation algorithms presented in this article, is based on computing precision, recall and parameter $F1$. These three parameters determine the algorithms efficiency by comparing boundaries of their segments. Each of the algorithms is compared with segmentation by a human. Based on this comparison, precision, recall and parameter $F1$ are computed. The definition of precision and recall is given by:

$$P = \frac{C}{C + F} \cdot 100\%, \tag{14}$$

$$R = \frac{C}{C + M} \cdot 100\%, \tag{15}$$

where C is the number of correct detected pixels that belongs to boundary, F is the number of false detected pixels and M is the number of not detected pixels.

Parameter $F1$ is combined measure from precision and recall. It is in high values if both precision and recall have high values and on the other hand, if one of them has low value, the value of the parameter $F1$ is going down. The definition of parameter $F1$ is given by:

$$F1 = \frac{2PR}{P + R}. \tag{16}$$

5. Experimental results

Experimental part of the paper consists of the experiments on real images. For this purpose, Berkeley's database of natural images was used [16]. The size of images is 256×384 (384×256) pixels. The example of images is in Fig. 1.



Fig. 1 Images of Berkeley database

Efficient graph based colour image segmentation algorithm was used for the experiments. The algorithm was programmed in C++ language. The main principle of this paper is to compare the results of segmentations with using different type of metrics. Gradually, all metrics introduced in chapter 3 were used in the algorithm. Special evaluation criterion was used for the comparison [17]. The criterion is based on the computing precision, recall and parameter F1. It works by comparison of two images, comparison of boundaries of the segments from image segmented by algorithm and boundaries made by human. The experimental results from algorithm are shown in the next figure and tables.

Based on visual representation of results shown in Fig. 2, the best results were achieved by metrics Bray Curtis Fig. 2b, Canberra Fig. 2c, Clark Fig. 2d and Jaccard Fig. 2g. They have less over-seg-

Averaged results achieved for all metrics.

Table 1

Metric	P [%]	R [%]	F1 [%]	Computing time [s]
BrCu	53.34	24.81	33.87	34.19
Canb	53.34	24.81	33.87	34.21
Clar	51.68	27.33	35.75	40.19
Eucl	55.47	18.42	27.66	37.57
Hamm	55.46	18.83	28.11	35.31
Jacc	45.87	36.82	40.85	37.13
Lore	54.85	18.44	27.61	46.83
Manh	55.21	18.58	27.80	33.12
Min3	55.46	18.38	27.60	52.97
Min4	55.46	18.38	27.60	53.02
Min5	55.50	18.40	27.63	54.33

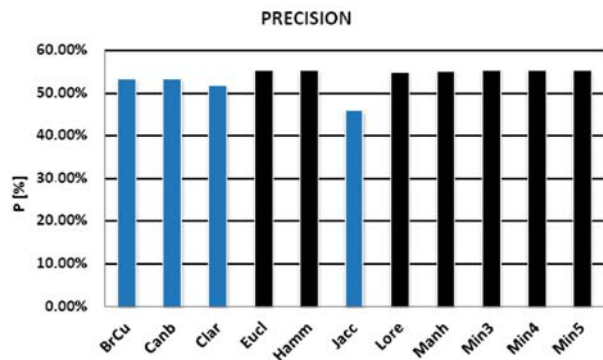


Fig. 3 Average results of precision for all metrics

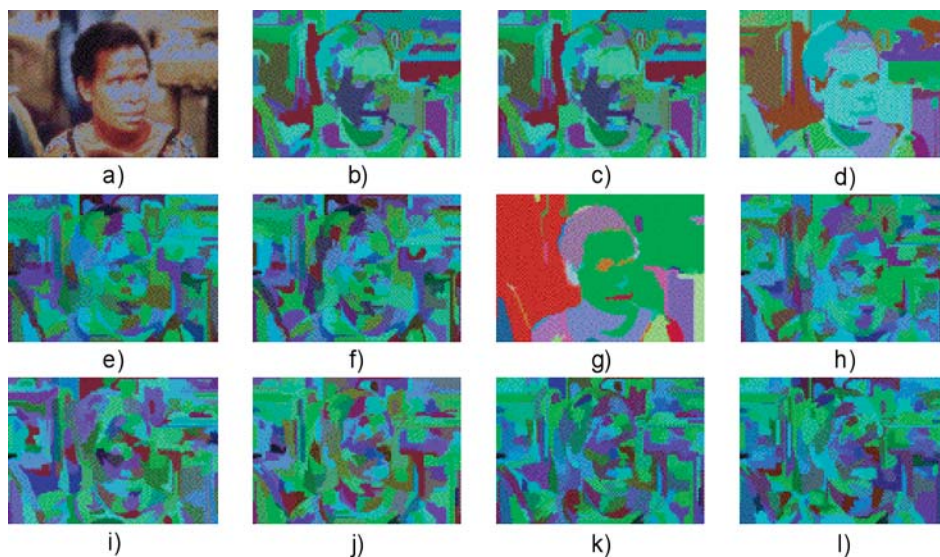


Fig. 2 The example of results achieved for all metrics; a) original image, b) Bray Curtis, c) Canberra, d) Clark, e) Euclidean, f) Hamming, g) Jaccard, h) Lorentzian, i) Manhattan, j) Minkowski ($p = 3$), k) Minkowski ($p = 4$), l) Minkowski ($p = 5$)

mented images. The segmented images of other metrics seem to be more over-segmented.

From Table 1 there can be seen that the selection of metric has impact on the quality of results. There is lot of differences in the percent results achieved from the experiments. Neither from all metrics had the best all three evaluation parameters and best computing time.

The first parameter from evaluation criterion is precision. From Fig. 3 it is evident that the results for all metrics are very similar. The values of this parameter are about 55% for the best metrics. Only one metric has worse results value and that metric is Jaccard distance. This metric achieved results under 46%.

The next evaluation criterion parameter is recall. The results for all metrics are shown in Fig. 4. From Fig. 4 it is evident that the Jaccard distance had the best results in recall, almost 37%. The second was Clark distance with 27.33% and after that were Bray Curtis and Canberra distances with almost 25% recall. Other metrics had the final result of recall under the 19%.

Parameter *F1* is final parameter of evaluation criterion. It is defined as combination of precision and recall. The differences

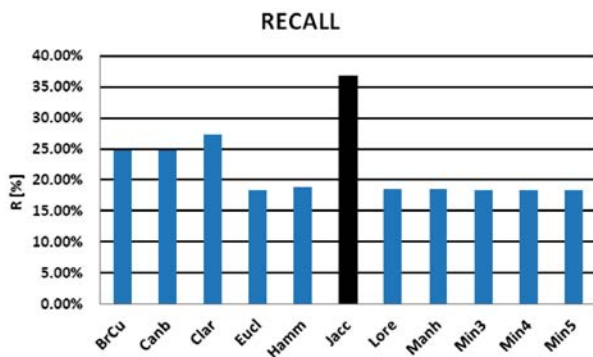


Fig. 4 Average results of recall for all metrics

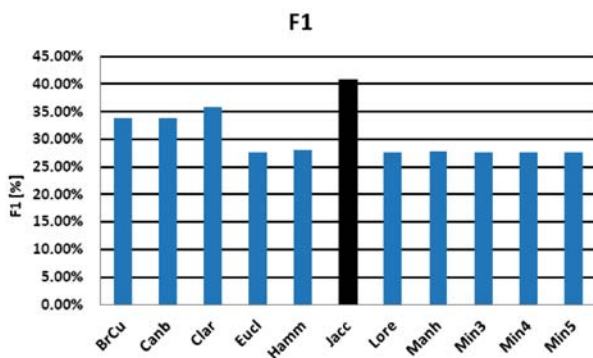


Fig. 5 Average results of parameter *F1* for all metrics

between the metrics based on this parameter can be seen in Fig. 5. The best from all metrics was Jaccard distance with almost 41%. This metric was the only one that reached the final results above 40%. The Clark distance had second best results with 35.75%. The Canberra and Bray Curtis distances had the same results almost 34%. All other distances had the parameter *F1* parameter less than 28%.

In Fig. 6 there are shown differences in computing time for the metrics. All results are for segmentation of 100 images. The best computing time for all images had the Manhattan, Canberra and Bray Curtis distances. Their computing time for all images was about 34 seconds. The Euclidean and Jaccard distances had the time about 37 seconds. The worst computing time score had the Lorentzian and Minkowski distances with results about 50 seconds. On the other hand, the differences are so big only for segmentations more images. For one image, the differences are only in milliseconds.

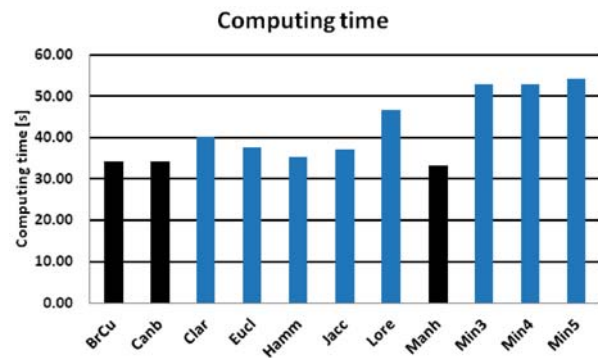


Fig. 6 Computing time for all metrics

6. Conclusion

In this paper, one well known colour image segmentation algorithm, and nine metrics that were gradually implemented to this algorithm, were presented. From the results it is possible to say that the best metric for efficient graph based algorithm is not definitely determined. For the precision, almost all metrics had the results more than 55%. Only Jaccard distance had the precision less than 50% (45.87%). On the other hand, the Jaccard distance is the best in the recall and *F1* parameters ($R = 36.82\%$ and $F1 = 40.85\%$). The experiments have shown that the metric selection is very important for the efficient graph based algorithm. The computing time for one image was different only in milliseconds for all metrics.

Acknowledgements

This paper has been supported by the VEGA grant agency no. 1/0570/10, "Algorithms research for automatic analysis of multimedia data".

References

- [1] MORAVCIK, T.: *Image Segmentation in Programming Environment MATLAB*, 11 International PhD Workshop OWD 2009, Wisla, pp. 469-470, October 2009.
- [2] ALSULTANNY, Y. A.: *Color Image Segmentation to the RGB and HSI Model Based on Region Growing Algorithm*, Proc. of the 4th WSEAS intern. conference on Computer Engineering and Applications, Cambridge, pp. 63-68, USA, 2010.
- [3] HEDJAM, R., MIGNOTTE, M.: *A Hierarchical Graph-Based Markovian Clustering Approach for the Unsupervised Segmentation of Textured Color Images*, Proc. of IEEE Int. Conf. Image Process., Cairo, Egypt, pp. 1365-1368, 2009.
- [4] SHI, J., MALIK, J.: Normalized Cuts and Image Segmentation, *IEEE Trans. Pattern Anal. Mach. Intell.*, vol. 22, no. 8, pp. 888-905, 2000.
- [5] DONG, G., XIE, M.: Color Clustering and Learning for Image Segmentation Based on Neural Networks, *IEEE Trans. Neural Netw.*, vol. 16, no. 4, pp. 925-936, 2005.
- [6] COMANICIU, D., MEER, P.: Mean Shift: A Robust Approach Toward Feature Space Analysis, *IEEE Trans. Pattern Anal. Mach. Intell.*, vol. 24, no. 5, pp. 603-619, 2002.
- [7] MIGNOTTE, M.: Segmentation by Fusion of Histogram-Based K-Means Clusters in Different Color Spaces, *IEEE Trans. Image Process.*, vol. 17, no. 5, pp. 780-787, 2008.
- [8] BHOYAR, K., KAKDE, O.: Color Image Segmentation based on JND Color Histogram, *Int. J. of Image Process.*, vol. 3, no. 6, pp. 283-292, 2010.
- [9] DENG, Y., MANJUNATH, B. S.: Unsupervised Segmentation of Color-texture Regions in Images and Video, *IEEE Trans. Pattern Anal. Mach. Intell.*, vol. 23, no. 8, pp. 1-26, 2001.
- [10] CLAIRET, J., BIGAND, A., COLOT, O.: *Color Image Segmentation using Type-2 Fuzzy Sets*, IEEE Inter. Conf. on E-Learning in Indust. Elec., pp. 52-57, 2006.
- [11] FELENZWALB, P. F., HUTTENLOCHER, D. P.: Efficient Graph-based Image Segmentation, *Int. J. of Computer Vision*, vol. 59, No. 2, pp. 1-26, 2004.
- [12] MACHAJ, J., BRIDA, P.: *A Comparison of Similarity Measurements for Database Correlation based Indoor Positioning System*, 2011.
- [13] CHA, S. H.: Comprehensive Survey on Distance/Similarity Measures between Probability Density Functions, *Int. J. of Mathematical Models and Methods in Applied Science*, vol. 1, no. 4, pp. 300-307, 2007.
- [14] KRAUSE, E. F.: *Taxicab Geometry an Adventure in Non-Euclidean Geometry*, Dover Publications, pp. 96, 1986.
- [15] TAX, D. M. J., DUIN, R., RIDDER, D. D.: *Classification, Parameter Estimation and State Estimation: an Engineering Approach using Matlab*, John Wiley and Sons, pp. 419, 2004.
- [16] WANG, J. Z.: Berkeley 1000 image database. [online 10.06.2011] Available on the internet. <http://wang.ist.psu.edu/~jwang/test1.tar>.
- [17] LUKAC, P., HUDEC, R., BENCO, M., DUBCOVA, Z., ZACHARIASOVA, M., KAMENCAY, P.: The Evaluation Criterion for Color Image Segmentation Algorithms, *J. of Electrical Engineering (JEEEC)*, vol. 63, no. 1, pp. 13-20, 2012.

Vladimir Medvid *

APPLICATIONS OF CUTTING STOCK PROBLEM

We present one heuristic solution for the well-known cutting stock problem which was formulated by Kantorovich in 1939. It is the problem of filling an order at minimum cost for specified numbers of lengths of material to be cut to given stock lengths of given cost. When expressed as an integer programming problem the large number of variables involved generally makes computation infeasible. The same difficulty persists when only an approximate solution is being sought by linear programming.

Keywords: model, linear programming, cutting stock, optimal solution, lower bound.

1. Introduction

The first known formulation of cutting stock problem was given in 1939 by the Russian economist and mathematician Kantorovich known to be NP complete problem [1]. The primary reasons for this activity are that cutting stock problems occur in a wide variety of industrial applications and there is a large economic incentive to find more effective solution procedures. It is easy to compare alternative solution procedures and to identify the potential benefits of using a proposed procedure [2].

For example imagine that you work in a factory and you have a number of valuable rod stocks waiting to be cut, yet different customers want different numbers of rods of various-sized lengths (e. g. for steel railway bridge [3]). How are you going to cut the rod stocks so that you minimize the waste?

2. Formulation of the problem

Let R_i be the nominal order requirements for rods of length s_i , $s_i \neq s_j$ for any elements i, j , $i \neq j$ $i = 1, \dots, m, j = 1, \dots, m$, to be cut from rod stocks of usable length s , b_i is the lower bound on the order requirement for rods of length s_i and c_j is the cost of pattern j [2]. This problem can be formulated as the following model:

$$\text{Minimize } \sum_{j=1}^m c_j x_j$$

$$\text{subject to } \sum_{j=1}^m a_{ij} x_j \geq b_i \quad i = 1, \dots, m,$$

where $x_j \geq 0$ and x_j are integer,

a_{ij} is the number of rods of length s_i to be slit from each rod stock that is processed using pattern j . In order for the elements a_{ij} ,

$i = 1, \dots, m$, to constitute a feasible cutting pattern, the following restriction must be satisfied:

$$\sum_{j=1}^m a_{ij} s_i \leq s,$$

where $a_{ij} \geq 0$ and a_{ij} are integer,

x_j is the number of rod stocks to be slit using pattern j , and c_j is

the trim loss incurred by pattern j , $c_j = s - \sum_{i=1}^m a_{ij} s_i$.

3. Solution approach

The main idea of solution approach lies in a scheduling of cutting stock in descending order with respect to a length of rods.

For this reason we sort out a set S of all order requirements s_i in descending order that yields the set $S = \{s_1, \dots, s_n\}$, where $s_i \geq s_{i+1}$ for $i = 1, \dots, n-1$. It seems that $m \leq n$ with respect to items b_i , where $b_i \geq 1$ and b_i are integer. Especially if any $b_i = 1$, $i = 1, \dots, m$ then $m = n$.

4. Procedure

1-st step. We create the set $S_k = \{s_1^*, \dots, s_k^*\}$, where s_1^*, \dots, s_k^* are the first k possible requirements of the set S such that $s_1^* + \dots + s_k^* + r_k = s$ and $r_k < s_i$ for $i = 1, \dots, n$. Here r_k represents a remainder by scheduling of cuts. Obviously this remainder is less than the arbitrary requirement $s_i \in S$.

2-nd step. We will progressively remove items of greatest lengths from the set S_k and add the nearest shorter items to S_k from the S . By this way we will find a nearest s_i^* greater than s_{i+1}^*

* Vladimir Medvid

Department of Mathematics, Faculty of Humanities, University of Zilina, Slovakia, E-mail: vladimir.medvid@fhv.uniza.sk

in the set S_k . The item s_i^* will be removed from S_k and added the nearest shorter items of the lengths $s_{i+1}^*, \dots, s_{i+l}^*$ to S_k until the condition is satisfied

$$s - (s_1^* + \dots + s_{i-1}^* + s_{i+1}^* + \dots + s_{i+l}^*) = r_k, \text{ where } r_k < s_i, s_i \in S \text{ for } i = 1, \dots, n \text{ and } S_k = \{s_1^*, \dots, s_{i-1}^*, s_{i+1}^*, \dots, s_{i+l}^*\}, l \text{ is positive integer.}$$

We repeat this step until the order set S has the same items of the greatest lengths. Finally we state as the 1-st cut of the stock. We remove all items $s_j \in S_k$ from the set S , i. e. $S := S - S_k$ and return on the 1-st step and continue. (a command $A := B$ means that the content of the set B is moved into the set A). We will repeat this procedure until the set S is empty.

5. Algorithm

Let $S = \{s_1, s_2, \dots, s_n\}$, S is the set of the rods of the lengths s_i , where $s_i \geq s_{i+1}$, $i = 1, 2, \dots, n$, s is a size of a whole rod stock, R is a set of remainders, $S_c = \emptyset$.

$$k = 0$$

0. $k := k + 1$. Let $R = \emptyset, S^* = \emptyset$. Let b be a number of rods of a maximal length s_1 and $S_k^b = \emptyset$. Choose the first j nearest possible rods of the lengths $s_1^*, s_2^*, \dots, s_j^*$ from the set S such that $s_1^*, s_2^*, \dots, s_j^* + r_{b+1} = s$, where $r_{b+1} < s_i$ for $i = 1, 2, \dots, n$ (i (iota) is the letter of the Greek alphabet). If $r_{b+1} = 0$ then $S_c := S_c \cup \{S_k^b\}$ and go to 3.

$$\text{Put } S_k^b = \{s_1^*, s_2^*, \dots, s_j^*\}, R := R \cup \{r_{b+1}\}$$

1. If there are the nearest rods of the lengths $s_i^*, s_{i+1}^* \in S_k^b$ such that $s_i^* > s_{i+1}^*$ then subtract s_i^* from the set S_k^b and add the nearest possible items of the lengths $s_{i+1}^*, \dots, s_{i+l}^*$ into S_k^b until the following condition

$$s - (s_1^* + \dots + s_{i-1}^* + s_{i+1}^* + \dots + s_{i+l}^*) = r_b \text{ where } r_b < s_i, i = 1, 2, \dots, n \text{ is satisfied and } S_k^b = \{s_1^*, \dots, s_{i-1}^*, s_{i+1}^*, \dots, s_{i+l}^*\}.$$

If $r_b = 0$ then $S_c := S_c \cup \{S_k^b\}$ and go to 3.

Else subtract s_j^* from S_k^b and add $s_{j+1}^*, \dots, s_{j+l}^*$ into S_k^b until the $s - (s_1^* + \dots + s_{j-1}^* + s_{j+1}^* + \dots + s_{j+l}^*) = r_b$ where $r_b < s_j$ is satisfied. If $S_k^b = S$ then $S_c := S_c \cup \{S_k^b\}$ and S_c represents the optimal solution, or optimal cuts of the rods. Else put

$$R := R \cup \{r_b\}, S^* := S^* \cup \{S_k^b\}$$

$$2. b := b - 1$$

If $b \geq 1$ go to 1, else choose the minimal r_b from the set R and the relevant set S_k^b from the set S^* .

$$3. \text{ Put } S := S - S_k^b, S_c := S_c \cup \{S_k^b\}.$$

If $S \neq \emptyset$ go to 0.

Else, the family set S_c represents the optimal cuts of the rods.

This algorithm was programmed in Matlab.

6. Problems

Practical realization was performed for several test problems. At first we present for illustration one simple problem below.

Problem 1. We have an unlimited number of rod stocks, each 600 cm length. The following 5 items must be cut (see the Table 1):

How is it possible to cut the rod stocks so that we minimize the waste?

Table 1

Length of rods (cm)	55	42	27	22	16
Number of rods	10	15	12	6	10

Solution.

We present the solution of this problem by our algorithm in the following tables.

The Table 1.1 represents the solution of the first cut of the rods (the maximal length $s_1 = 55, b = 10$). $S = \{10*55, 15*42, 12*27, 6*22, 10*16\}$ ((*)-times).

Table 1.1

1. type	2. type	3. type	4. type	5. type	\sum	rb
10*55	+1*42				592	8
9*55	+2*42				579	11
8*55	+3*42		+1*27		593	7
7*55	+5*42				595	5
6*55	+6*42			+1*16	598	2
5*55	+7*42		+1*27		596	4
4*55	+9*42				598	2
3*55	+10*42				585	15
2*55	+11*42		+1*27		599	1
1*55	+12*42		+1*27		586	14

The last but one row represents the best solution for the first cut. The minimal remainder $r_2 = 1$ and relevant $S_1^2 = \{2*55, 11*42, 1*27\}$.

$$S := S - S_1^2, \text{ i.e. } S = \{8*55, 4*42, 11*27, 6*22, 10*16\}$$

The Table 1.2 represents the solution of the second cut of the rods (the maximal length $s_1 = 55, b = 8$).

Table 1.2

1. type	2. type	3. type	4. type	5. type	Σ	r_b
8*55	+3*42	+1*27		+1*16	599	1
7*55	+4*42	+1*27		+1*16	596	4
6*55	+4*42	+3*27		+1*16	595	5
5*55	+4*42	+5*27		+1*22	600	0

The last row represents the best solution for the second cut. The minimal remainder $r_2 = 0$ and relevant $S_2^5 = \{5*55, 4*42, 5*27, 1*22\}$.

$$S: = S - S_2^5, \text{ i.e. } S = \{3*55, 6*27, 5*22, 10*16\}$$

The Table 1.3 represents the solution of the third cut of the rods (the maximal length $s_1 = 55, b = 3$).

Table 1.3

1. type	2. type	3. type	4. type	5. type	Σ	r_b
3*55		+6*27	+5*22	+10*16	597	3

The remainder $r_3 = 3$ and $S_3^3 = \{3*55, 6*27, 5*22, 10*16\}$.

This row represents the last cut because $S: = S - S_3^3, \text{ i.e. } S = \emptyset$.

Our optimal answer requires 3 rod stocks and has $r_1 + r_2 + r_3 = 1 + 0 + 3 = 4$ cm waste. The summary of the solution is shown below in the next Table 2:

Table 2

	Length of rods times number of rods					sum
1-st rod stock	55*2	42*11	27*1			599
2-nd rod stock	55*5	42*4	27*5	22*1		600
3-rd rod stock	55*3		27*6	22*5	16*10	597
total	55*10	42*15	27*12	22*6	16*10	1796

Imagine that we have one infinite rod stock and we need to cut this rod stock into the smaller rods mentioned above. Thus we need the total length of rod stock at least $TL = 55*10 + 42*15 + 27*12 + 22*6 + 16*10 = 1796$ cm. This is the lower bound for the optimal solution.

Sum of three rod stocks is 1800 cm. Our total length is $T = 1796$ cm. The waste is 4 cm. It is easy to see that our solution is minimal because our total length is equal to the lower bound, i.e. $T = TL$.

Problem 2. These next tasks arise from the practice. One business firm placed the special requirements. They needed to cut

several rods of different lengths from rod stocks of different types and lengths.

We present the list of corresponding requirements in the Tables 3–7:

1-st requirement

Type: beam 8 40×40 L, length of rod stock 8000 mm Table 3

Length of rods (mm)	1450	1320	960	860	720	260	100
Number of rods	60	3	80	30	12	30	30

2-nd requirement

Type: beam 8 40×40 L, length of rod stock 8000 mm Table 4

Length of rods (mm)	1220	358	765	542	395	386	360	350
number of rods	4	6	8	1	1	3	8	1

Length of rods (mm)	345	305	300	290	260	250	170	100
number of rods	1	1	1	4	4	2	14	6

3-rd requirement

Type: tube D30, length of rod stock 6000 mm Table 5

Length of rods (mm)	1300	700	840
Number of rods	6	33	81

4-th requirement

Type: beam 5 20×10, length of rod stock 3000 mm Table 6

Length of rods (mm)	1400	1280	940	822	800	682
Number of rods	1	1	15	4	6	2

5-th requirement

Type: beam of roller ledge, length of rod stock 3000 mm Table 7

Length of rods (mm)	1400	1365	940	860	800	450
Number of rods	4	4	20	2	8	2

7. Solutions of problems

We present our answers for the all requirements mentioned above.

Solution for the 1-st requirement

The answer requires 27 rod stocks. It is presented in the following Table 8:

Table 8

Ordinal number of the rod stock	1	2	3	4	5	6	7	8	9	10	11	12	13	14
Remainder of the rod stock	0	20	20	20	20	20	20	20	20	20	20	20	20	20
Ordinal number of the rod stock	15	16	17	18	19	20	21	22	23	24	25	26	27	
Remainder of the rod stock	20	20	0	0	0	20	60	60	320	320	320	320	1280	

Our remainder is $OR = 3000$ mm. The total length of the all rods is $TL = 1450*60 + 1320*3 + 960*80 + 860*30 + 720*12 + 260*30 + 100*30 = 213000$. We had to use 27 rod stocks, i.e. $L = 27*8000 = 216000$ mm.

The total remainder is $TR = L - TL = 216000 - 213000 = 3000$ mm. The difference D of our remainder and the total remainder is $D = OR - TR = 0$ mm. It means that we have found the best solution for this case.

Solution for the 2-nd requirement

Table 9

Ordinal number of the rod stock	1	2	3	4
Remainder of the rod stock	0	5	40	3990

Now the answer requires 4 rod stocks. Table 9 represents our solution together with the remainders on the every used rod stock.

Our remainder is $OR = 4035$ mm. The total length of the all rods is $TL = 1220*4 + 835*6 + 765*8 + 542*1 + 395*1 + 386*3 + 360*8 + 350*1 + 345*1 + 305*1 + 300*1 + 290*4 + 260*4 + 250*2 + 170*14 + 100*6 = 27965$ mm. It have been used 4 rod stocks, i.e. $L = 4*8000 = 32000$ mm.

The total remainder is $TR = L - TL = 32000 - 27965 = 4035$ mm. The difference of our remainder and the total remainder is $D = OR - TR = 0$ mm. We have found the best solution again.

Solution for the 3-rd requirement

The answer requires 17 rod stocks (see the Table 10 below): Our remainder is $OR = 3060$ mm. The total length of all the rods is $TL = 1300*6 + 700*33 + 840*81 = 98940$ mm. 17 rod stocks were used, i.e. $L = 17*6000 = 102000$ mm.

The total remainder is $TR = L - TL = 102000 - 98940 = 3060$ mm. The difference of our remainder and the total remainder is $D = OR - TR = 0$ mm. As above we have again found the best solution.

Solution for the 4-th requirement

The answer to this requirement requires 10 rod stocks (see the Table 11):

Our remainder is $OR = 3768$ mm. The total length of all the rods is $TL = 1400*1 + 1280*1 + 940*15 + 822*4 + 800*6 + 682*2 = 26232$ mm. We have used 10 rod stocks. If we imagine that we have one infinite rod stock then the least integer multiple of 3000 greater than 26232 is 27000 for $n = 9$, i.e. $L = 9*3000 = 27000$ mm.

The total remainder is $TR = L - TL = 27000 - 26232 = 768$ mm. The difference of our remainder and the total remainder is $D = OR - TR = 3000$ mm.

Solution for the 5-th requirement

The answer requires 14 rod stocks (see the Table 12):

Table 10

Ordinal number of the rod stock	1	2	3	4	5	6	7	8	9
Remainder of the rod stock	40	40	40	120	120	120	120	120	120
Ordinal number of the rod stock	10	11	12	13	14	15	16	17	
Remainder of the rod stock	120	120	120	120	120	120	400	1100	

Table 11

Ordinal number of the rod stock	1	2	3	4	5	6	7	8	9	10
Remainder of the rod stock	98	180	180	180	180	298	96	556	600	1400

Table 12

Ordinal number of the rod stock	1	2	3	4	5	6	7	8	9	10	11	12	13	14
Remainder of the rod stock	180	180	180	180	180	180	200	200	30	10	35	35	270	1260

Our remainder is $OR = 3120$ mm. The total length of all the rods is $TL = 1400*4 + 1365*4 + 940*20 + 860*2 + 800*8 + 450*2 = 38880$ mm. We used 14 rod stocks. There is an analogous reason as the one mentioned above, the ideal number of rod stocks is $n = 13$, i.e. $L = 13*3000 = 39000$ mm.

The total remainder is $TR = L - TL = 39000 - 38880 = 120$ mm. The difference of our remainder and the total remainder is $D = OR - TR = 3000$ mm.

8. Evaluation

In Problem 1 and in the first three tasks (requirements 1, 2, 3) of Problem 2 we obtained the exact solution, because our solution reached the lower bound of the requirement.

In the other tasks (requirements 4, 5) we used one more rod stock than the lower bound. Still these solutions can be accepted because the lower bound is the absolute minimum which does not need to be always reached. This is explained in the following example.

We have 3000 mm rod stocks and we need to cut 3 rods of the length 1600 mm. It is obvious that we will use three 3000 mm rod stocks, because when one 1600 mm rod is cut, the remainder is 1400 mm and is useless. The lower bound is $3*1600 = 4800$

mm, and $4800 < 6000$ mm, i.e. 2 rod stocks, we would only use 4800 mm, which is less than two 3000 mm rod stocks. One less than three 3000 mm rod stocks.

The computational time of all the problems lasted under 1 second.

According to the facts and examples mentioned above it would be interesting to find exact solution and compare it with our solution. Let us point out that we were looking for the solution of the above Problem 1 by exact methods accessible on the internet <http://code.google.com/p/cspsol/>. Here the computational time is quite high, i.e. over one hour.

9. Conclusion

Our observations may be concluded as follows:

The longer the rod stocks are and the shorter our rods required are, the more closely we get to the lower bound, i.e. we can be sure about accuracy of our solution.

In practice we usually use the rod stocks of length 6000-8000 mm. Using these lengths we reached exact solutions.

Supported by the grant KEGA 088 zU-4/2011.

References

[1] GILMORE, P. C., GOMORY, R. E.: A Linear Programming Approach to the Cutting-Stock Problem, *Operation research* 9, 1961, pp. 849-859.
 [2] HAESSLER, R. W., SWEENEY, P. E.: Cutting Stock Problem and Solution Procedures, *European J. of Operational Research* 54, (1991), pp. 141-150.
 [3] VICAN, J., GOCAL, J., JOST, J.: Fatigue Resistance of Typical Fatigue Prone Riveted Steel Railway Bridge Structural Detail, *Communications - Scientific Letters of the University of Zilina*, vol. 13, No. 3, 2011, pp. 5-8.

Julia Stoberova *

DYNAMICS OF HAEMATOPOIETIC STEM CELLS MODEL

The article deals with the haematopoietic stem cells model with delay introduced by M. C. Mackey [1]. Our aim is to establish the new conditions under which the equilibria of the model are stable or unstable. The model without delay is also investigated.

Keywords: Haematopoietic stem cells, equilibrium, stability, differential system, delay argument.

1. Introduction

The population of haematopoietic stem cells gives rise to all of the differentiated elements of the blood (see [1, 2]): the white blood cells, red blood cells and platelets; which may be either actively proliferating or in a resting phase. After entering the proliferating phase, a cell is committed to undergo cell division at a fixed time τ later. The generation time τ is assumed to consist of four phases: the pre-synthesis phase, the DNA synthesis phase, the post-synthesis phase and the mitotic phase. Just after the division, both daughter cells go into the resting phase. Once in this phase, they can either return to the proliferating phase and complete the cycle or die before ending the cycle. The dynamics of the model is governed by the nonlinear differential system with delay argument:

$$\begin{aligned} \frac{dN}{dt} &= -\delta N(t) - \beta(N(t))N(t) + \\ &+ 2e^{-\gamma\tau}\beta(N(t-\tau))N(t-\tau), \\ \frac{dP}{dt} &= -\gamma P(t) - \beta(N(t))N(t) - \\ &- e^{-\gamma\tau}\beta(N(t-\tau))N(t-\tau), t \geq 0, \end{aligned} \tag{1}$$

where $\beta(N)$ is a monotone decreasing function and has the explicit form of a Hill function:

$$\beta(N) = \beta_0 \frac{\theta^n}{\theta^n + N^n}, \quad n = 1, 2, \dots$$

The symbols in (1) have a following interpretation: N is the number of cells in nonproliferative phase, P is the number of cycling proliferating cells, γ is the rate of cells loss from proliferative phase, δ is the rate of cells loss from nonproliferative phase, τ is the time spent in the proliferative phase, β is the feedback function which represents the rate of recruitment from nonproliferative phase, β_0

is the maximum recruitment rate and θ, n control the shape of the feedback function. We assume that $\delta, \gamma, \tau, \beta_0, \theta \in (0, \infty)$.

2. Equilibria of System (1) Without Delay

For $\tau = 0$ the system (1) has a form

$$\begin{aligned} \frac{dN}{dt} &= -\delta N(t) - \beta(N(t))N(t), \\ \frac{dP}{dt} &= -\gamma P(t), t \geq 0. \end{aligned} \tag{2}$$

The equilibrium points of (2) we obtain from the system

$$\begin{aligned} -\delta N + \beta(N)N &= 0, \\ -\gamma P &= 0. \end{aligned}$$

The system (2) has the trivial equilibrium $E_0 = (N, P) = (0, 0)$ and the nontrivial equilibrium $E = (N^*, P^*) = (\beta^{-1}(\delta), 0)$.

The value $N^* = \beta^{-1}(\delta)$ we can obtain from the equation

$$\begin{aligned} \beta(N^*) &= \beta_0 \frac{\theta^n}{\theta^n + N^{*n}}, \\ \beta(\beta^{-1}(\delta)) &= \beta_0 \frac{\theta^n}{\theta^n + N^{*n}}, \end{aligned}$$

$$\delta(\theta^n + N^{*n}) = \beta_0 \theta^n,$$

$$N^* = \theta \left(\frac{\beta_0}{\delta} - 1 \right)^{\frac{1}{n}}, \beta_0 > \delta.$$

* Julia Stoberova

Department of Crisis Management, Faculty of Special Engineering, University of Zilina, Slovakia, E-mail: julia.stoberova@gmail.com

3. Stability of Equilibria Without Delay

Theorem 1. [2] Assume that $\delta \in (0, \beta_0)$. Then the system (2) has the trivial equilibrium $E_0 = (0, 0)$ which is unstable and a positive one $E = (N^*, 0)$ which is asymptotically stable.

Theorem 2. Suppose that $\delta \in (\beta_0, \infty)$. Then the system (2) has the trivial equilibrium $E_0 = (0, 0)$ which is asymptotically stable.

Proof. The matrix of the linearized system (2) has a form

$$A = \begin{pmatrix} -\delta + \beta'(N)N + \beta(N) & 0 \\ 0 & -\gamma \end{pmatrix}$$

and the matrix of the linearized system around $E_0 = (0, 0)$ is given by

$$A_1 = \begin{pmatrix} -\delta + \beta'(0)0 + \beta(0) & 0 \\ 0 & -\gamma \end{pmatrix} = \begin{pmatrix} -\delta + \beta_0 & 0 \\ 0 & -\gamma \end{pmatrix}.$$

Then the characteristic equation of the linearized system of (2) around E_0 is

$$\det(A_1 - \lambda I) = 0,$$

$$\begin{vmatrix} -\delta + \beta_0 - \lambda & 0 \\ 0 & -\gamma - \lambda \end{vmatrix} = 0,$$

$$(\lambda + \gamma)(\lambda - \beta_0 + \delta) = 0.$$

This equation has two roots given by

$$\lambda_1 = -\gamma < 0, \lambda_2 = \beta_0 - \delta < 0, (\delta > \beta_0).$$

Thus the point $E_0 = (0, 0)$ is asymptotically stable equilibrium of the system (2).

4. Model with Delay $\tau > 0$

Using

$$\delta(N) = \beta(N)N$$

we rewrite system (1) as follows

$$\frac{dN}{dt} = -\delta N(t) - \alpha(N(t)) + 2e^{-\gamma\tau} \alpha(N(t-\tau)), \quad (3)$$

$$\frac{dP}{dt} = -\gamma P(t) + \alpha(N(t)) - e^{-\gamma\tau} \alpha(N(t-\tau)), t \geq 0.$$

We set

$$s = \frac{t}{\tau} \quad \text{i.e. } t = s\tau$$

and we get

$$N(t) = N(s\tau) = u(s), N(t - \tau) = N(\tau(s - 1)) = u(s - 1),$$

$$P(t) = P(s\tau) = v(s),$$

$$\frac{dN(t)}{dt} = \frac{du(s)}{dt} = \frac{du(s)}{ds} \frac{ds}{dt} = \dot{u}(s) \frac{1}{\tau},$$

$$\frac{dP(t)}{dt} = \frac{dv(s)}{dt} = \frac{dv(s)}{ds} \frac{ds}{dt} = \dot{v}(s) \frac{1}{\tau}.$$

Using the relations above the system (3) is transformed into the next one

$$\dot{u}(t) = \tau[-\delta u(t) - \alpha(u(t)) + 2e^{-\gamma\tau} \alpha(u(t-1))], \quad (4)$$

$$\dot{v}(t) = \tau[-\gamma v(t) + \alpha(u(t)) - e^{-\gamma\tau} \alpha(u(t-1))], t \geq 0.$$

In the next consideration we will use the root τ of the equation

$$\beta_0(2e^{-\gamma\tau} - 1) - \delta = 0.$$

We get

$$e^{-\gamma\tau} = \frac{1 + \frac{\delta}{\beta_0}}{2},$$

$$-\gamma\tau = \ln \frac{1 + \frac{\delta}{\beta_0}}{2},$$

$$\tau = \frac{1}{\gamma} \ln \frac{2}{1 + \frac{\delta}{\beta_0}}.$$

We will use the notation

$$\bar{\tau} = \frac{1}{\gamma} \ln \frac{2}{1 + \frac{\delta}{\beta_0}}.$$

Lemma 1. Suppose that $0 < \delta < \beta_0$. Then $\bar{\tau} > 0$.

Proof. We have

$$\frac{\delta}{\beta_0} < 1, 1 + \frac{\delta}{\beta_0} < 2 \text{ and } \frac{2}{1 + \frac{\delta}{\beta_0}} > 1 \text{ implies that } \bar{\tau} > 0.$$

Lemma 2. Assume that $0 < \delta < \beta_0$. Then for $0 < \tau < \bar{\tau}$ it holds that

$$\beta_0(2e^{-\gamma\tau} - 1) - \delta > 0.$$

Proof. Since $\tau < \bar{\tau}$, then

$$\gamma\tau < \ln \frac{2}{1 + \frac{\delta}{\beta_0}},$$

$$2e^{-\gamma\tau} > 1 + \frac{\delta}{\beta_0},$$

$$\beta_0(2e^{-\gamma\tau} - 1) - \delta > 0.$$

Lemma 3. Suppose that $0 < \delta < \beta_0$. Then for $0 < \tau < \bar{\tau}$ it holds that $2e^{-\gamma\tau} - 1 > 0$.

Proof. Since $\beta_0(2e^{-\gamma\tau} - 1) - \delta > 0$. and $\beta_0 > 0, \delta > 0$, it follows that

$$2e^{-\gamma\tau} - 1 > 0.$$

Lemma 4. Assume that $0 < \delta < \beta_0$. Then for $\tau > \bar{\tau}$ the next inequality holds

$$\beta_0(2e^{-\gamma\tau} - 1) - \delta < 0.$$

Proof. Since $\tau > \bar{\tau}$, then we get

$$\gamma\tau > \ln \frac{2}{1 + \frac{\delta}{\beta_0}},$$

$$2e^{-\gamma\tau} < 1 + \frac{\delta}{\beta_0},$$

$$\beta_0(2e^{-\gamma\tau} - 1) - \delta < 0.$$

5. Equilibria of System (4)

If we take $a(u) = \beta(u)u$, then the equilibria of (4) we obtain from the system

$$\begin{aligned} -\delta u - \beta(u)u + 2e^{-\gamma\tau} \beta(u)u &= 0, \\ -\gamma v - \beta(u)u - e^{-\gamma\tau} \beta(u)u &= 0. \end{aligned} \tag{5}$$

The first equation of (5) is satisfied for

$$u = 0 \text{ or } -\delta - \beta(u) + 2e^{-\gamma\tau} \beta(u) = 0.$$

For $u = 0$ from the second equation of (5) we get that $v = 0$.

So the system (4) has the trivial equilibrium $(u, v) = (0, 0)$.

The positive equilibrium of (4) we obtain from the system

$$\begin{aligned} -\delta - \beta(u) + 2e^{-\gamma\tau} \beta(u) &= 0, \\ -\gamma v + \beta(u)u - e^{-\gamma\tau} \beta(u)u &= 0. \end{aligned}$$

From the first equation it follows that

$$\beta(u) = \frac{\delta}{2e^{-\gamma\tau} - 1}$$

According to Hill function we have

$$\beta_0 \frac{\theta^n}{\theta^n + u^n} = \frac{\delta}{2e^{-\gamma\tau} - 1},$$

$$u^n = \beta_0 \theta^n \frac{2e^{-\gamma\tau} - 1}{\delta} - \theta^n,$$

$$u = \theta \left(\frac{\beta_0(2e^{-\gamma\tau} - 1) - \delta}{\delta} \right)^{\frac{1}{n}}.$$

From the second equation we get

$$\begin{aligned} v &= \frac{u}{\gamma} (\beta(u) - e^{-\gamma\tau} \beta(u)) = \frac{u}{\gamma} \beta(u) (1 - e^{-\gamma\tau}) = \\ &= \frac{du}{\gamma} \left(\frac{1 - e^{-\gamma\tau}}{2e^{-\gamma\tau} - 1} \right) = \frac{\delta \theta}{\gamma} \left(\frac{\beta_0(2e^{-\gamma\tau} - 1) - \delta}{\delta} \right)^{\frac{1}{n}} \cdot \\ &\quad \cdot \frac{1 - e^{-\gamma\tau}}{2e^{-\gamma\tau} - 1}. \end{aligned}$$

Put $u = u^*, v = v^*$. For $0 < \delta < \beta_0, 0 < \tau < \bar{\tau}$ the point $E^* = (u^*, v^*)$ is a positive equilibrium of the system (4).

6. Trivial Equilibrium of System (4)

The linearized system of (4) around the trivial equilibrium $(0,0)$ is given by

$$\dot{u}(t) = \tau[\delta - a'(0)u(t) + 2e^{-\gamma\tau} a'(0)u(t - 1)],$$

$$\dot{v}(t) = \tau[-\gamma v(t) + a'(0)u(t) - e^{-\gamma\tau} a'(0)u(t - 1)].$$

The characteristic equation of the linearized system of (4) is

$$\begin{vmatrix} \tau[-\delta - a'(0) + 2e^{-\gamma\tau} a'(0)] - \lambda & 0 \\ \tau[a'(0) - e^{-\gamma\tau} a'(0)] & -\tau\gamma - \lambda \end{vmatrix} = 0,$$

$$(\lambda + \tau\gamma)(\lambda + \tau[\delta + a'(0) - 2e^{-\gamma\tau} a'(0)]) = 0.$$

The roots of the equation above are

$$\lambda_1 = -\tau\gamma, \lambda_2 = \tau[-\delta - a'(0) + 2e^{-\gamma\tau} a'(0)].$$

Because $a'(0) = \beta(0) = \beta_0$, we have

$$\lambda_1 = -\tau\gamma, \lambda_2 = \tau[-\delta + \beta_0(2e^{-\gamma\tau} - 1)].$$

Theorem 3. [2] Suppose $0 < \delta < \beta_0$. Then for $0 < \tau < \bar{\tau}$ the trivial equilibrium $(0, 0)$ of the system (4) is unstable.

Proof. Since $\lambda_1 = -\tau\gamma < 0$ and with regard to Lemma 2 we have that $\lambda_2 = \tau[-\delta + \beta_0(2e^{-\gamma\tau} - 1)] > 0$ then equilibrium $(0, 0)$ is unstable.

Theorem 4. Suppose that $0 < \delta < \beta_0$. Then for $\tau > \bar{\tau}$ the trivial equilibrium $(0, 0)$ of the system (4) is asymptotically stable.

Proof. We have $\lambda_1 = -\tau\gamma < 0$ and according to Lemma 4 $\lambda_2 = \tau[-\delta + \beta_0(2e^{-\gamma\tau} - 1)] < 0$. Then the equilibrium $(0, 0)$ is asymptotically stable.

7. Positive Equilibrium of System (4)

The linearized system of (4) around the positive equilibrium $E^* = (u^*, v^*)$ is given by

$$\dot{u}(t) = \tau[\delta - \alpha'(u^*)u(t) + 2e^{-\gamma\tau} \alpha'(u^*)u(t-1)],$$

$$\dot{v}(t) = \tau[-\gamma v(t) + \alpha'(u^*)u(t) - e^{-\gamma\tau} \alpha'(u^*)u(t-1)].$$

The characteristic equation of the linearized system of (4) around E^* is

$$\begin{vmatrix} \tau[-\delta - \alpha'(u^*) + 2e^{-\gamma\tau} e^{-\lambda} \alpha'(u^*)] - \lambda & 0 \\ \tau[\alpha'(u^*) - e^{-\gamma\tau} e^{-\lambda} \alpha'(u^*)] & -\tau\gamma - \lambda \end{vmatrix} = 0,$$

$$(\lambda + \tau\gamma)(\lambda + \tau[\delta + \alpha'(u^*) - 2e^{-\gamma\tau} e^{-\lambda} \alpha'(u^*)]) = 0.$$

From this equation we obtain

$$\lambda_1 = -\tau\gamma \text{ or } \lambda + \tau[\delta + (1 - 2e^{-\gamma\tau} e^{-\lambda})\alpha'(u^*)] = 0.$$

We will be interested in real part of the roots of equation

$$\lambda + \tau\delta + \tau[(1 - 2e^{-\gamma\tau} e^{-\lambda})\alpha'(u^*)] = 0. \tag{6}$$

Theorem 5. Suppose that $\alpha'(u^*) < 0$ and $-\alpha'(u^*)(1 + 2e^{-\gamma\tau}) < \delta < \beta_0$ for $0 < \tau < \bar{\tau}$. Then the equilibrium $E^* = (u^*, v^*)$ is asymptotically stable.

Proof. Let $\lambda = \mu + iv$ be the root of (6). Then we have

$$\mu + iv + \tau\delta + \tau(1 - 2e^{-\gamma\tau} e^{-(\mu + iv)})\alpha'(u^*) = 0,$$

$$\mu + \tau\delta + \tau\alpha'(u^*) - 2\tau e^{-\gamma\tau} \alpha'(u^*) e^{-\mu} \cos v + i(v + 2\tau e^{-\gamma\tau} \alpha'(u^*) e^{-\mu} \sin v) = 0.$$

Separating the real and imaginary parts leads to

$$\mu + \tau\delta + \tau\alpha'(u^*) - 2\tau e^{-\gamma\tau} \alpha'(u^*) e^{-\mu} \cos v = 0, \tag{7}$$

$$v + 2\tau e^{-\gamma\tau} \alpha'(u^*) e^{-\mu} \sin v = 0.$$

We assume that (7) is satisfied for some $\mu \geq 0$. Then we get

$$\tau\delta + \tau\alpha'(u^*) - 2\tau e^{-\gamma\tau - \mu} \alpha'(u^*) \cos v \leq 0$$

and

$$2\tau e^{-\gamma\tau - \mu} \alpha'(u^*) \cos v \geq \delta + \alpha'(u^*). \tag{8}$$

Since

$$\delta > -\alpha'(u^*)(1 + 2e^{-\gamma\tau}) > -\alpha'(u^*),$$

then $\delta + \alpha'(u^*) > 0$. From (8) we have

$$\cos v \leq \frac{\delta + \alpha'(u^*)}{2e^{-\gamma\tau - \mu} \alpha'(u^*)} < 0.$$

Because $-1 \leq \cos v \leq 1$, we obtain

$$-1 \leq \frac{\delta + \alpha'(u^*)}{2e^{-\gamma\tau - \mu} \alpha'(u^*)} < 0,$$

$$-2e^{-\gamma\tau - \mu} \alpha'(u^*) \geq \delta + \alpha'(u^*) > 0,$$

$$\delta \leq -\alpha'(u^*)(1 + 2e^{-\gamma\tau - \mu}).$$

Since $1 + 2e^{-\gamma\tau - \mu} \leq 1 + 2e^{-\gamma\tau}$, we get

$$\delta \leq -\alpha'(u^*)(1 + 2e^{-\gamma\tau}).$$

This is a contradiction with condition $\delta > -\alpha'(u^*)(1 + 2e^{-\gamma\tau})$ of the theorem. So it cannot be $\mu \geq 0$. Thus $\lambda = \mu + iv$ has a negative real part. From it follows that E^* is asymptotically stable.

Theorem 6. Suppose that $\alpha'(u^*) \geq 0$ and $\alpha'(u^*)(2e^{-\gamma\tau} - 1) < \delta < \beta_0$ for $0 < \tau < \bar{\tau}$. Then the equilibrium $E^* = (u^*, v^*)$ is asymptotically stable.

Proof. Assume that (7) is satisfied for some $\mu \geq 0$. If $\alpha'(u^*) = 0$, then from (8) we obtain that $\delta \leq 0$, which is a contradiction with condition that $\delta > 0$. So we will assume that $\alpha'(u^*) > 0$. From (8) we get

$$\cos v \geq \frac{\delta + \alpha'(u^*)}{2e^{-\gamma\tau - \mu} \alpha'(u^*)} > 0.$$

Since $|\cos v| \leq 1$, we have

$$\frac{\delta + \alpha'(u^*)}{2e^{-\gamma\tau - \mu} \alpha'(u^*)} \leq 1,$$

$$\delta + \alpha'(u^*) \leq 2e^{-\gamma\tau - \mu} \alpha'(u^*),$$

$$\delta \leq \alpha'(u^*)(2e^{-\gamma\tau - \mu} - 1).$$

Because

$$2e^{-\gamma\tau-\mu} - 1 \leq 2e^{-\gamma\tau} - 1,$$

we obtain that

$$\delta \leq a'(u^*)(2e^{-\gamma\tau} - 1),$$

which is a contradiction with condition that

$$\delta > a'(u^*)(2e^{-\gamma\tau} - 1).$$

So it cannot be $\mu \geq 0$. Thus $\mu < 0$ and E^* is asymptotically stable equilibrium.

8. Simulation

For $\beta_0 = 2, \delta = 1, \gamma = 1, \tau = 1, \theta = 1, n = 2$ the system (4) is given by

$$\dot{u}(t) = -u(t) - \frac{2u(t)}{1 + u^2(t)} + \frac{4}{e} \frac{u(t-1)}{1 + u^2(t-1)}, \tag{9}$$

$$\dot{v}(t) = -v(t) - \frac{2u(t)}{1 + u^2(t)} + \frac{2}{e} \frac{u(t-1)}{1 + u^2(t-1)}, t \geq 0.$$

Fig. 1 shows three solutions of (9) in the phase plane which converge to asymptotically stable equilibrium $E = (0, 0)$, (Theorem 4).

For $n = 2, \theta = 1, \beta_0 = 2, \delta = 1, \gamma = 1, \tau = 0.1$ the system (4) has a form

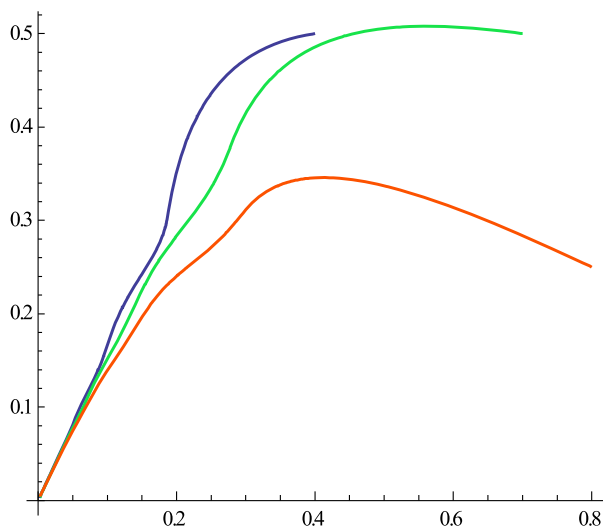


Fig. 1 Solutions of (9) in the phase plane

$$\dot{u}(t) = 0.1 \left[-u(t) - \frac{2u(t)}{1 + u^2(t)} + 4e^{-0.1} \frac{u(t-1)}{1 + u^2(t-1)} \right], \tag{10}$$

$$\dot{v}(t) = 0.1 \left[-v(t) - \frac{2u(t)}{1 + u^2(t)} - 2e^{-0.1} \frac{u(t-1)}{1 + u^2(t-1)} \right],$$

$$t \geq 0.$$

Fig. 2 shows three solutions of (10) in the phase plane which converge to asymptotically stable equilibrium $E^* = (u, v) = (0.7870, 0.0925)$, (Theorem 6).

9. Conclusion

Since the differentiation and interaction in a population of haematopoietic stem cells is very complex and complicated, it is difficult to comprehend the large scale dynamics of this process without the formal structure of a mathematical model.

The main results of the article are new, extend and improve some results in [2]. For example the conditions of Theorem 6 are satisfied for $n = 2, \theta = 1, \beta_0 = 2, \delta = 1, \gamma = 1, \tau = 0.1$ or for $n = 2, \theta = 1, \beta_0 = 2, \delta = 1.5, \gamma = 1, \tau = 0.05$ or for $n = 2, \theta = 1, \beta_0 = 2, \delta = 1.2, \gamma = 1, \tau = 0.1$ But these parameters do not satisfy condition of Theorem 3.1 in [2].

Acknowledgement

The research was supported by the Grant 1/1260/12 of the Scientific Grant Agency of the Ministry of Education of the Slovak Republic.

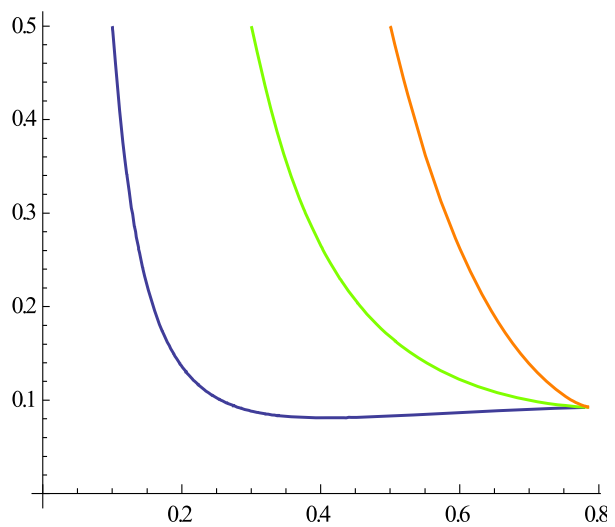


Fig. 2 Solutions of (10) in the phase plane

References

- [1] MACKEY, M. C.: Unified Hypothesis for the Origin Aplastic Anemia and the Periodic Hematopoietics, *Blood* 51, 5 (1978).
- [2] TALIBI ALAOUI, H., YAFIA, R.: Stability and Hopf Bifurcation in an Approachable Haematopoietic Stem Cells Model, *Mathematical Biosciences*. 206 (2007), pp. 176-184.
- [3] DOROCIAKOVA, B., OLACH, R.: Existence of Positive Solutions of Delay Differential Equations, *Tatra Mt. Math. Publ.* 43, 2009, pp. 63-70.
- [4] LEVIN, S. A., HALLAM, T. G., GROSS, L. J.: *Applied Mathematical Ecology*, Springer - Verlag, Berlin : New York : London : Tokyo, 1989.
- [5] MARUSIAK, P., OLACH, R.: *Functional Differential Equations (in Slovak)*. EDIS - University of Zilina, 2000.
- [6] OLACH, R.: Observation of a Feedback Mechanism in a Population Model, *Nonlinear Analysis*, 41 (2000), pp. 539-544.

**COMMUNICATIONS - Scientific Letters of the University of Zilina
Writer's Guidelines**

1. Submitted papers must be unpublished and must not be currently under review for any other publication.
2. Submitted manuscripts should not exceed 8 pages including figures and graphs (in Microsoft WORD - format A4, Times Roman size 12, page margins 2.5 cm).
3. Manuscripts written in good English must include abstract and keywords also written in English. The abstract should not exceed 10 lines.
4. Submission should be sent: By e-mail - as an attachment - to one of the following addresses: komunikacie@uniza.sk or holesa@uniza.sk (or on CD to the following address: Zilinska univerzita, OVaV - Komunikacie, Univerzitna 1, SK-10 26 Zilina, Slovakia).
5. Uncommon abbreviations must be defined the first time they are used in the text.
6. Figures, graphs and diagrams, if not processed in Microsoft WORD, must be sent in electronic form (as JPG, GIF, TIF, TTF or BMP files) or drawn in high contrast on white paper. Photographs for publication must be either contrastive or on a slide.
7. The numbered reference citation within text should be enclosed in square brackets. The reference list should appear at the end of the article (in compliance with ISO 690).
8. The numbered references (in square brackets), figures, tables and graphs must be also included in text - in numerical order.
9. The author's exact mailing address, full names, E-mail address, telephone or fax number, the name and address of the organization and workplace (also written in English) must be enclosed.
10. The editorial board will assess the submitted paper in its following session. If the manuscript is accepted for publication, it will be sent to peer review and language correction. After reviewing and incorporating the editor's comments, the final draft (before printing) will be sent to authors for final review and minor adjustments
11. Submission deadlines are: September 30, December 31, March 31 and June 30.

COMMUNICATIONS

SCIENTIFIC LETTERS OF THE UNIVERSITY OF ZILINA
VOLUME 14

Editor-in-chief:

Prof. Ing. Otakar Bokuvka, PhD.

Editorial board:

Prof. Ing. Jan Bujnak, CSc. - SK
 Prof. Ing. Otakar Bokuvka, PhD. - SK
 Prof. RNDr. Peter Bury, CSc. - SK
 Prof. RNDr. Jan Cerny, DrSc. - CZ
 Prof. Eduard I. Danilenko, DrSc. - UKR
 Prof. Ing. Branislav Dobrucky, PhD. - SK
 Prof. Dr.hab Inž. Stefania Grzeszczyk - PL
 Prof. Ing. Vladimír Hlavna, PhD. - SK
 Prof. RNDr. Jaroslav Janacek, PhD. - SK
 Prof. Ing. Hermann Knoflacher - A
 Doc. Dr. Zdena Kralova, PhD. - SK
 Doc. Ing. Tomas Lovecek, PhD. - SK
 Prof. Ing. Milan Moravcik, CSc. - SK
 Prof. Ing. Gianni Nicoletto - I
 Prof. Ing. Ludovít Parilak, CSc. - SK
 Prof. Ing. Pavel Polednak, PhD. - SK
 Prof. Bruno Salgues - F
 Prof. Andreas Steimel - D
 Prof. Ing. Miroslav Steiner, DrSc. - CZ
 Prof. Ing. Marian Sulgan, PhD. - SK
 Prof. Josu Takala - SU
 Doc. Ing. Martin Vaculik, PhD. - SK

Address of the editorial office:

Zilinská univerzita
 Office for Science and Research
 (OVaV)
 Univerzitna 1
 SK 010 26 Zilina
 Slovakia

E-mail: komunikacie@uniza.sk

Each paper was reviewed by two reviewers.

Journal is excerpted in Compendex and Scopus.

It is published by the University of Zilina in
 EDIS - Publishing Institution of Zilina University
 Registered No: EV 3672/09
 ISSN 1335-4205

Published quarterly

Single issues of the journal can be found on:
<http://www.uniza.sk/komunikacie>